The Software Development and Physics Pre-study of ND280++ on Hyper-Kamiokande Experiment

Master Thesis

Author(s):
Wu, Jialin

Publication date:
2023

Permanent link:
https://doi.org/10.3929/ethz-b-000644677

ETH Zürich
Department of Physics
Institute for Particle Physics and Astrophysics
Master of Science in Physics

The Software Development and Physics Pre-study of ND280++ on Hyper-Kamiokande Experiment

Master Thesis

Submitted by:
Jialin Wu

Supervisor(s):
Prof. Dr. Davide Sgalaberna

Tutor:
Botao Li

Zürich, 2023

Eidgenössische Technische Hochschule Zürich
Swiss Federal Institute of Technology Zurich

Declaration of originality

The signed declaration of originality is a component of every semester paper, Bachelor's thesis, Master's thesis and any other degree paper undertaken during the course of studies, including the respective electronic versions.

Lecturers may also require a declaration of originality for other written papers compiled for their courses.

I hereby confirm that I am the sole author of the written work here enclosed and that I have compiled it in my own words. Parts excepted are corrections of form and content by the supervisor.

Title of work (in block letters):

THE SOFTWARE DEVELOPMENT AND PHYSICS PRE-STUDY OF ND280++ ON HYPER-KAMIOKANDE EXPERIMENT

Authored by (in block letters):

For papers written by groups the names of all authors are required.

Name(s):	**First name(s):**
JIALIN WU	JIALIN

With my signature I confirm that

- I have committed none of the forms of plagiarism described in the 'Citation etiquette' information sheet.
- I have documented all methods, data and processes truthfully.
- I have not manipulated any data.
- I have mentioned all persons who were significant facilitators of the work.

I am aware that the work may be screened electronically for plagiarism.

Place, date	**Signature(s)**
ETH Zürich, October 26, 2023	Jialin Wu 武家麟

For papers written by groups the names of all authors are required. Their signatures collectively guarantee the entire content of the written paper.

Abstract

T2K (Tokai-to-Kamioka) experiment is a long baseline neutrino oscillation experiment whose goal is to precisely measure 3-neutrino PMNS matrix parameters θ_{13}, θ_{23} and Δm^2_{32} and to look for a hint of CP violation in the leptonic sector of the elementary particle physics. Other goals of the experiment include measurements of various neutrino-nucleus scattering cross sections and sterile neutrino searches. The CP violation is examined by observing differences of oscillation probabilities $\nu_\mu \to \nu_e$ and its CP conjugated counterpart $\bar{\nu}_\mu \to \bar{\nu}_e$. T2K is collecting data from both ν_μ ($\bar{\nu}_\mu$) disappearance and ν_e ($\bar{\nu}_e$) appearance channels. The observation is made by comparing neutrino flux predictions based on measurements at the near detector complex (ND280) located at 280 m down stream of the hadron production target, where neutrinos do not travel enough distance to oscillate, and the observed flux at the far detector Super-Kamiokande (Super-K), a 50 kilo tons ultra-pure water Cherenkov detector located at a distance of about 295 km away from the neutrino production spot.

The reduction of systematic uncertainties is vital for the precise measurements of neutrino oscillation parameters. The dominant origin of systematic uncertainties is the ignorance of produced neutrino flux $\phi(E_\nu)$ from parent hadrons' leptonic and semileptonic decays. The ND280 is responsible for measuring non-oscillated neutrino flux, neutrino-nucleus cross sections and reducing their systematic uncertainties. The ND280 is under an important upgrade planned to be complete in 2023. The upgraded ND280 is expected to bring down a systematic uncertainty of the number of predicted events at Super-Kamiokande from 6% to 4%, which meets needs of the T2K-II phase project. This phase of the T2K experiment is supposed to provide a 3σ exclusion of CP conservation for 36% of the δ_{CP} phase space, if the neutrino mass ordering is given.

However, this is still not evident enough to announce a convincing CP violation or conservation of neutrino oscillations. In a longer term, the plan is to start the successor of the T2K experiment – the Hyper-Kamiokande experiment. The Hyper-Kamiokande experiment is planned to start its operation in the year around 2027. Hyper-Kamiokande will investigate CP violations by measuring differences between flavour oscillation probabilities for neutrinos and for antineutrinos. For 75% of the δ_{CP} phase space, it will be able to confirm non-zero CP violation with 3σ significance. And for over 50% of the δ_{CP} phase space with 5σ significance. To match the needs of the Hyper-Kamiokande experiment, the upgraded ND280 also requires a second major upgrade to ND280++, where one of the current Fine Grained Detectors (FGD) based on scintillator bars might be replaced by a Hyper-Fine Grained Detector (HFGD) based on sub-mm scintillating fibers (SciFi).

The first chapter of this master thesis provides an introduction to neutrino physics with especial attention to neutrino oscillation formalism and long-baseline accelerator neutrino oscillation experiments. A very brief introduction to the T2K experiment is presented in the second chapter. A preliminary software of a novel Hyper-Fine Grained Detector (HFGD) with two kinds of geometry designs is developed, with a great emphasis on the performance of sub-mm scintillating fibers alternating along orthogonal directions, which can provide isotropic, high-resolution tracking in

polystyrene-based scintillators. The details of HFGD designs and software implementations are illustrated in the third chapter. The included physics pre-studies based on the HFGD are: the proton track reconstruction efficiency, the relevant CC0πNp event reconstruction efficiency, the momentum reconstructions and charge identifications by track curvatures, and the γ rejection efficiency estimation. They are discussed in sequence from the fourth chapter to the sixth chapter. The seventh also the last chapter functions as a short overall conclusion to the whole thesis work.

Acknowledgements

First of all and most importantly, I would like to thank Prof. Dr. Davide Sgalaberna for providing me with such a precious opportunity of working with ETH neutrino physics group and T2K collaboration. I am extremely grateful for his passionate instructions and active discussions no matter in our software group meetings or personal communications, from which I benefited a lot.

My thesis tutor Botao Li undoubtedly keeps my most sincere gratefulness. His patience, friendship, encouragement, experienced skills and countless technical supports help me overcome many difficulties of the research.

I have to express my deepest gratitude to my senior and friend Till Dieminger as well. His contribution to the pure scintillating fiber simulation software implementation directly supports the physics analysis based on that. Many fruitful discussions with him also innovate new ideas and deeper understandings of the research subject.

I also warmly and kindly appreciate Xingyu Zhao, Dr. Matthew Franks and Dr. Saul Alonso Monsalve for their supports to my thesis study.

Besides, I gratitude nice accompanies and humorous joy from my friendly office mates Nived Puthumana Meleppattu, Botao Li, Dr. Johannes Wüthrich and Dr. Alex Stauffer.

At last, I am and will always be thankful to my dear parents, for their unconditional supports and infinite love.

Contents

Acronyms and abbreviations

AGS	Alternating Gradient Synchrotron
BNL	Brookhaven National Laboratory
CC	Charged Current
CCQE	Charged Current Quasi-Elastic
CC0πNp	Charged Current 0 pion N protons
CERN	The European Organization for Nuclear Research
CID	Charge Identification
CKM matrix	the Cabibbo–Kobayashi–Maskawa matrix
ECal	Electromagnetic Calorimeter
FD	Far Detector
FGD	Fine Grained Detector
HA-TPC	High-Angle Time Projection Chamber
HFGD	Hyper-Fine Grained Detector
HpTPC	High-Pressure Time Projection Chamber
IBD	Inverse Beta Decay
INGRID	Interactive Neutrino Grid
J-PARC	Japan Proton Accelerator Research Complex
KEK	The High Energy Accelerator Research Organization
LNGS	Laboratori Nazionali del Gran Sasso
NC	Neutral Current
ND	Near Detector
ND280	Near Detector Complex at 280 m
NOL	Nanostructured Organosilicon Luminophore
PDE	Photon Detection Efficiency
p0D	Pi-zero Detector
p.e.	photoelectron
PID	Particle Identification
PMNS matrix	the Pontecorvo–Maki–Nakagawa–Sakata matrix
POPOP	1,4-bis(5-phenyloxazol-2-yl) benzene
PTP	para-Terphenyl
QE	Quasi-Elastic
R&D	Research and Development
SciFi	Scintillating Fiber
Single Exp. Att.	Single Exponential Attenuation
SM	Standard Model of Particle Physics
SPAD	Single-Photon Avalanche Diode
Super-FGD	Super-Fine-Grained Detector
Super-K	Super-Kamiokande
TOF	Time of Flight
TPC	Time Projection Chamber
T2K	Tokai to Kamioka
UV	UltraViolet
WLS	Wavelength Shifting Fiber

1 Introduction to Neutrino Physics

In the Standard Model (SM) of Particle Physics, neutrinos are introduced as massless spin $\frac{1}{2}$ fermions which are electrically neutral and chromoly colorless. Therefore, they only participate in weak interactions via exchanging $W^{\pm}$ (charged current, CC) and Z^0 (neutral current, NC) gauge bosons. They are represented by three massless, chirally left-handed Dirac spinor fields ν_e, ν_μ and ν_τ in their flavour eigenstates and arranged with corresponding left-handed charged lepton fields e^-, μ^- and τ^- to form three-generation $\mathrm{SU}(2)_L$ doublets

$$\begin{bmatrix} \nu_e \\ e^- \end{bmatrix}_L , \begin{bmatrix} \nu_\mu \\ \mu^- \end{bmatrix}_L , \begin{bmatrix} \nu_\tau \\ \tau^- \end{bmatrix}_L . \tag{1}$$

In experiments, with the discovery of neutrino flavour oscillations, physicists believe that at least two of three nuetrinos are granted a tiny mass ($< 1.1\,\mathrm{eV}/c^2$ [1]) in their mass eigenstates ν_1, ν_2 and ν_3.

In subsection 1.1, a brief history of neutrino physics is introduced. After that, the theoretical formalism of mass-induced neutrino flavour oscillations in a $3-\nu$ paradigm is discussed in subsection 1.2. Then some important neutrino oscillation experiments are briefly reviewed in subsection 1.3. At last, motivations of this thesis research are proposed in subsection 1.4.

1.1 A brief history of neutrino physics

Major references of subsection 1.1 are **Chapter 21: Neutrinos and the Three Lepton Families** (pp. 655-692) of the textbook *Phenomenology of Particle Physics* [2] by Prof. Dr. André Rubbia and the English Wikipedia webpage *Neutrino Oscillation* [3].

In the early 20th century, after the discovery of radioactivity by Becquerel and many subsequent studies, physicists were aware that there were different types of rays(i.e. α, β and γ) from nucleus. The α-rays consist of ${}^4_2\mathrm{He}^{2+}$ nuclei emitted from the decay of radioactive isotopes. They appeared to be mono-chromatic (i.e. mono-energetic) because of their well-defined stopping range in materials. γ-rays are energetic photons emitted via the transition between different nucleus states whose energy intervals are also discrete. Thus the γ-rays from a certain process are also mono-chromatic. However, the β-rays which are emitted electrons from nuclei seemed to possess a continuous energy spectrum. Initially, the β decay was considered to be a two-body decay of a nucleus with fixed kinematics, where a single-valued energy of β-rays was expected. Situations even became worse after Chadwick and Ellis experimentally concluded that the β decay itself was the unique source of the continuous energy spectrum, which formed a physics crisis at that time. What's more, Ellis and Wooster's further experiment even showed that some energy was missing in the β decay and the lost energy cannot be trapped in the calorimeter of their experiment. Hence the law of energy conservation was also challenged by the puzzle of β decay! Theoretically, Niels Bohr even came up with the idea that the energy conservation might only be statistically valid.

In 1930, Pauli wrote a famous letter to remedy the crisis by conjecturing that an undiscovered electrically neutral fermion, which he called "neutron" was also emitted in the β decay. In 1932, Chadwick discovered the actual neutron which is a building block of nucleus. Then Enrico Fermi decided to relabel the Pauli's "neutron" as "neutrino", which literally means "small neutron" in Italian. Because of the tiny cross section of neutrinos' interactions, it was not until 1958 did Cowan and Reines directly prove the existence of neutrinos in the Savannah River Plant Experiment. The nuclear reactor at the plant was an intense, pure and controllable source of the low-energy $\bar{\nu}_e$(i.e. reactor neutrinos). The inverse beta decay (IBD) channel ($\bar{\nu}_e + p \rightarrow n + e^+$) was used in the experiment to detect neutrinos. In 1959, Melvin Schwartz, an American physicist from Columbia University, created an idea of using energetic neutrinos in the GeV range from high-energy positive pions' weak decay $\pi^+ \rightarrow \mu^+ + \nu_\mu$ to study weak interactions and address the unitarity violation of cross sections derived from Fermi's theory. Together with the virtue of the "absence of the β decay" of charged pions, the question that whether ν_μ and ν_e are different neutrinos could also be answered. In 1962, the famous BNL-Columbia experiment led by Lederman, Schwartz and Steinberger at the Brookheaven National Laboratory (BNL) Alternating Gradient Synchrotron (AGS) concluded that $\nu_\mu \neq \nu_e$. Thus it also proved the existence of ν_μ(i.e. accelerator neutrinos) which were produced by the AGS accelerator. Finally, in 2000, the DONUT(Direct Observation of NU Tau) experiment directly detected the ν_τ based on the detection of the tau lepton $\tau^\pm$ and the high-energy hadrons produced in the charged-current interaction of a neutrino and a nucleon. The experimental verification of three generations of neutrinos $\nu_e \neq \nu_\mu \neq \nu_\tau \neq \nu_e$ was finally achieved.

Neutrino flavour oscillations were first predicted by Bruno Pontecorvo in 1957 and independently discussed by Maki, Nakagawa and Sagata as a consequence of lepton mixing. In analogy to the CKM quark mixing matrix, the idea of Pontecorvo–Maki–Nakagawa–Sakata matrix (PMNS matrix) was first introduced in 1962 to explain the oscillation [4]. After that, a great deal of evidence of neutrino oscillations has been collected from different sources, over a wide range of energies and with various distinct experimental techniques. In the late 1960s, Ray Davis' Homestake experiment firstly detected the effects of neutrino oscillations. He observed a large ($\sim \frac{2}{3}$) deficit of the flux of solar neutrinos (predominately produced as ν_e in the core of the Sun through various nuclear fusion reactions [5]) from the measurement when comparing with the Standard Solar Model's prediction. Until 2001, the Sudbury Neutrino Observatory provided the clear evidence that the main source of deficit came from neutrino flavour oscillations when ν_e propagated from sun to earth. In 1998, the first experimental evidence for atmospheric neutrino oscillations was announced by the Super-Kamiokande experiment which provided a very precise measurement in an energy range of hundreds MeV to a few TeV, with a baseline of the diameter of the Earth. For the accelerator neutrinos, many experiments have observed the same oscillations as in atmospheric neutrino oscillation using neutrinos with a few GeV of energy and several-hundred-km baselines. The MINOS, K2K, and Super-K experiments have all independently observed ν_μ disappearance over such long baselines. Many experiments have also searched for oscillations of $\bar{\nu}_e$ from nuclear reactors. Such oscillations determine the value of parameter θ_{13} of the PMNS matrix (see Eq.(15)). In 2011, the Double Chooz experiment concluded that $\theta_{13} \neq 0$. Then in 2012, the Daya Bay experiment found that $\theta_{13} \neq 0$ with a significance of 5.2σ. RENO experiment confirmed the results above.

1.2 Neutrino oscillations in the 3-flavour PMNS framework

Main references of subsection 1.2 are **Review 14: Neutrino Masses, Mixing, and Oscillations** (pp. 285-308) of *The Review of Particle Physics (2022)* [1] and the English Wikipedia webpage *Neutrino Oscillation* [3].

1.2.1 Flavour Oscillations in Vacuum

Neutrinos are produced in their flavour eigenstates(i.e. ν_e, ν_μ and ν_τ) and travel freely in their mass eigenstates(i.e ν_1, ν_2 and ν_3) which diagonalize the free-propagation Hamiltonian. Two mismatch eigenbasis are linked by a unitary PMNS matrix U as follows [3]:

$$\begin{bmatrix} \nu_\mathrm{e} \\ \nu_\mu \\ \nu_\tau \end{bmatrix} = \begin{bmatrix} U_{\mathrm{e}1} & U_{\mathrm{e}2} & U_{\mathrm{e}3} \\ U_{\mu 1} & U_{\mu 2} & U_{\mu 3} \\ U_{\tau 1} & U_{\tau 2} & U_{\tau 3} \end{bmatrix} \begin{bmatrix} \nu_1 \\ \nu_2 \\ \nu_3 \end{bmatrix}. \tag{2}$$

Compactly and reversely [1],

$$|\nu_\alpha\rangle = \sum_i U_{\alpha i} |\nu_i\rangle , \tag{3}$$

$$|\nu_i\rangle = \sum_\alpha U^*_{\alpha i} |\nu_\alpha\rangle , \tag{4}$$

where the Greek letter $\alpha \in \{e, \mu, \tau\}$ denotes the flavour and the Latin letter $i \in \{1,2,3\}$ labels the mass eigenbasis. For the mass eigenstate $|\nu_j\rangle$, its free propagation can be expressed as a plane wave [3]

$$\left|\nu_j(t)\right\rangle = e^{-i(E_j t - \vec{p}_j \cdot \vec{x})} \left|\nu_j(0)\right\rangle , \tag{5}$$

where all physical quantities are in natural units. Practically, neutrinos have extremely tiny mass(less than 1 eV/c^2) and always propagate in the ultra-relativistic limit where $E_j \approx |\vec{p}_j| \gg m_j$ and $t = \frac{L}{\beta_j} \approx L$ in natural units. Therefore, we have

$$\begin{gathered} E_j = \sqrt{\vec{p}_j^{\,2} + m_j^2} \approx E + \frac{m_j^2}{2E} , \\ |\vec{p}_j| \approx E , \end{gathered} \tag{6}$$

where E is the energy of the neutrino. Inserting equation (6) into equation(5) yields

$$\left|\nu_j(L)\right\rangle = e^{-\mathrm{i}\frac{m_j^2}{2E}L} \left|\nu_j(0)\right\rangle . \tag{7}$$

After substituting the equation (7) into the equation (3), we get

$$|\,\nu_\alpha(L)\rangle = \sum_j U_{\alpha j} e^{-\mathrm{i}\frac{m_j^2}{2E}L} \big|\,\nu_j(0)\,\big\rangle\,. \tag{8}$$

Then we define a quantity $P_{\alpha\to\beta}(L)$ standing for the probability of detecting a β-flavoured neutrino after an α-flavoured neutrino is created via the weak interactions and freely propagates a distance L. It is straightforward that

$$P_{\alpha\to\beta}(L) \,=\, \Big|\big\langle\,\nu_\beta\,\big|\,\nu_\alpha(L)\,\big\rangle\Big|^2 \,=\, \left|\sum_j U_{\alpha j}\,U^*_{\beta j}\,e^{-\mathrm{i}\frac{m_j^2}{2E}L}\right|^2\,. \tag{9}$$

The equation (9) can be recast into a more physically intuitive form

$$\begin{aligned} P_{\alpha\to\beta}(L) = \delta_{\alpha\beta} - 4\sum_{j>k} \mathbf{Re}\Big\{U^*_{\alpha j}\,U_{\beta j}\,U_{\alpha k}\,U^*_{\beta k}\Big\}\,\sin^2\left(\frac{\Delta m^2_{jk}L}{4E}\right) \\ +2\sum_{j>k}\mathbf{Im}\Big\{U^*_{\alpha j}\,U_{\beta j}\,U_{\alpha k}\,U^*_{\beta k}\Big\}\,\sin\left(\frac{\Delta m^2_{jk}L}{2E}\right)\,, \end{aligned} \tag{10}$$

where $\Delta m^2_{jk} \equiv m^2_j - m^2_k$. For experimental practice, the oscillation phase factor from the equation (10) is often written in a more convenient manner with proper units explicitly

$$\frac{\Delta m^2_{jk}c^4 L}{4\hbar c E} = \frac{\mathrm{GeV\,fm}}{4\hbar c}\times\frac{\Delta m^2_{jk}c^4}{\mathrm{eV}^2}\frac{L}{\mathrm{km}}\frac{\mathrm{GeV}}{E} \approx 1.267\times\frac{\Delta m^2_{jk}}{\mathrm{eV}^2}\frac{L}{\mathrm{km}}\frac{\mathrm{GeV}}{E}\,. \tag{11}$$

The second sum of equation (10) is of great interests for physicists. It links to the CP asymmetry as follows

$$A^{(\alpha\beta)}_{\mathrm{CP}} = P(\nu_\alpha\to\nu_\beta) - P(\bar\nu_\alpha\to\bar\nu_\beta) = 4\sum_{j>k}\mathbf{Im}\Big\{U^*_{\alpha j}\,U_{\beta j}\,U_{\alpha k}\,U^*_{\beta k}\Big\}\,\sin\left(\frac{\Delta m^2_{jk}L}{2E}\right)\,. \tag{12}$$

In terms of the Jarlskog Invariant J_{CP}, the relation $\mathbf{Im}\Big\{U^*_{\alpha j}\,U_{\beta j}\,U_{\alpha k}\,U^*_{\beta k}\Big\} = -J_{\mathrm{CP}}\sum_{\gamma,\ell}\varepsilon_{\alpha\beta\gamma}\,\varepsilon_{jk\ell}$ holds as a consequence of unitarity of PMNS matrix. Then the equation (12) is equivalent to [3]

$$A^{(\alpha\beta)}_{\mathrm{CP}} = 16\sin\left(\frac{\Delta m^2_{21}L}{4E}\right)\sin\left(\frac{\Delta m^2_{32}L}{4E}\right)\sin\left(\frac{\Delta m^2_{31}L}{4E}\right)J_{\mathrm{CP}}\sum_\gamma\varepsilon_{\alpha\beta\gamma}\,. \tag{13}$$

From the equation (13), we can see that the CP violation only appears if and only if all following conditions are satisfied

$$\alpha\neq\beta\,,\,\Delta m^2_{21}\neq 0\,,\,\Delta m^2_{32}\neq 0\,,\,\Delta m^2_{31}\neq 0\,,\,J_{\mathrm{CP}}\neq 0\,. \tag{14}$$

As a leptonic analogy to the CKM matrix for quarks mixing, PMNS matrix can be parameterized by three real mixing angles(θ_{12}, θ_{13} and θ_{23}) and a physical phase δ_{CP} [1]

$$\begin{aligned} U &= \begin{pmatrix} 1 & 0 & 0 \\ 0 & c_{23} & -s_{23} \\ 0 & s_{23} & c_{23} \end{pmatrix} \cdot \begin{pmatrix} c_{13} & 0 & s_{13}e^{-\mathrm{i}\delta_{\mathrm{CP}}} \\ 0 & 1 & 0 \\ -s_{13}e^{+\mathrm{i}\delta_{\mathrm{CP}}} & 0 & c_{13} \end{pmatrix} \cdot \begin{pmatrix} c_{12} & s_{12} & 0 \\ -s_{12} & c_{12} & 0 \\ 0 & 0 & 1 \end{pmatrix} \\ &= \begin{pmatrix} c_{12}c_{13} & s_{12}c_{13} & s_{13}e^{-\mathrm{i}\delta_{\mathrm{CP}}} \\ -s_{12}c_{23} - c_{12}s_{13}s_{23}e^{\mathrm{i}\delta_{\mathrm{CP}}} & c_{12}c_{23} - s_{12}s_{13}s_{23}e^{\mathrm{i}\delta_{\mathrm{CP}}} & c_{13}s_{23} \\ s_{12}s_{23} - c_{12}c_{23}s_{23}e^{\mathrm{i}\delta_{\mathrm{CP}}} & -c_{12}s_{23} - s_{12}s_{13}c_{23}e^{\mathrm{i}\delta_{\mathrm{CP}}} & c_{13}c_{23} \end{pmatrix}, \end{aligned} \tag{15}$$

where $s_{ij} \equiv \sin\theta_{ij}$ and $c_{ij} \equiv \cos\theta_{ij}$. Without loss of generality, θ_{ij} can be confined in the first quadrant, $\theta_{ij} \in [0, \frac{\pi}{2}]$. And δ_{CP} takes the value among $[0, 2\pi]$. From the parameterization (15), one can easily derive

$$\mathbf{Im}\left\{ U^*_{\alpha j}\, U_{\beta j}\, U_{\alpha k}\, U^*_{\beta k} \right\} = -J_{\mathrm{CP}} \sum_{\gamma,\ell} \varepsilon_{\alpha\beta\gamma}\, \varepsilon_{jk\ell} \equiv -J^{\max}_{\mathrm{CP}} \sin\delta_{\mathrm{CP}} \sum_{\gamma,\ell} \varepsilon_{\alpha\beta\gamma}\, \varepsilon_{jk\ell}\ , \tag{16}$$

where $J^{\max}_{\mathrm{CP}}$ is given by

$$J^{\max}_{\mathrm{CP}} \equiv c_{12}\, s_{12}\, c_{23}\, s_{23}\, c^2_{13}\, s_{13}\ . \tag{17}$$

Then the equation (13) becomes

$$A^{(\alpha\beta)}_{\mathrm{CP}} = 16 \sin\left(\frac{\Delta m^2_{21} L}{4E}\right) \sin\left(\frac{\Delta m^2_{32} L}{4E}\right) \sin\left(\frac{\Delta m^2_{31} L}{4E}\right) \sin\left(\delta_{\mathrm{CP}}\right) J^{\max}_{\mathrm{CP}} \sum_{\gamma} \varepsilon_{\alpha\beta\gamma}\ . \tag{18}$$

CP violation is believed to be a prerequisite of the matter-antimatter asymmetry observed in our universe. And the measurement of δ_{CP} by comparing the difference of the oscillation probability of $\nu_\mu \to \nu_e$ and $\bar{\nu}_\mu \to \bar{\nu}_e$, for example, may provide an answer to this fundamental puzzle.

1.2.2 Neutrino Propagation in Matter

Sub-subsection 1.2.2 is recast exhaustively from **Sec.14.5: Propagation of Massive Neutrinos in Matter** (pp. 289-291) of *The Review of Particle Physics (2022)* [1].

The probability of an incoherent inelastic scattering between neutrinos and medium is very small. For example, a characteristic cross section for ν-proton scattering is of the order

$$\sigma \sim \frac{G_F^2 s}{\pi} \sim 10^{-43}\mathrm{cm}^2 \left(\frac{E}{\mathrm{MeV}}\right)^2\ , \tag{19}$$

where G_F is the Fermi constant and s is the square of the center of mass energy of the collision.

However, when neutrinos propagate in the dense matter, they can also interact coherently with the medium. The interference between scattered and unscattered neutrino waves due to the different phase velocity caused by scattering are also possible, which enhances the matter effect in neutrino propagation. By definition, the medium remains intact in coherent interactions. Hence it allows the decoupling of neutrino evolution equations from the medium ones. Therefore the matter effect can be introduced as an effective neutrino potential V determined by the density and compositions of medium. For example, the mass-eigen-basis evolution equation for three Standard Model active ultra-relativistic neutrinos propagating in matter can be written as [1]

$$\mathrm{i}\frac{d\vec{\nu}}{dx} = H\vec{\nu}\ , \quad H = H_m + U^\dagger V U\ . \tag{20}$$

Here x is the spatial coordinate of the neutrino trajectory in the medium, $\vec{\nu} \equiv (\nu_1, \nu_2, \nu_3)^T$ is a vector of neutrino mass eigenstates in vacuum, H_m is the kinetic Hamiltonian

$$H_m = \frac{1}{2E}\mathrm{diag}\left(m_1^2, m_2^2, m_3^2\right)\ , \tag{21}$$

and V is the effective neutrino potential (e.g. Eq.(22)) provided by the medium in the interaction basis. U is the 3×3 unitary PMNS matrix (see Eq.(2)) relating flavour eigenstates $(\nu_e, \nu_\mu, \nu_\tau)^T$ (i.e. in interaction basis) and mass eigenstates $\vec{\nu} \equiv (\nu_1, \nu_2, \nu_3)^T$ in vacuum. For instance, in a neutral medium consisting electrons, protons and neutrons, the effective potential takes the form

$$V = \mathrm{diag}\left(\pm\sqrt{2}G_F n_e(x), 0, 0\right) \equiv \mathrm{diag}\left(V_e, 0, 0\right)\ . \tag{22}$$

The sign + (−) in Eq.(22) corresponds to neutrinos (antineutrinos) and $n_e(x)$ denotes for the number density of electrons in the medium. In general, $n_e(x)$ is not a constant along the neutrino trajectory.

The instantaneous Hamiltonian $H(x)$ for a fixed x in Eq.(20) can be diagonalized by a unitary matrix $\tilde{U}(x)$ such that

$$\tilde{U}^\dagger(x) H(x) \tilde{U}(x) = \frac{1}{2E}\mathrm{diag}\left(\mu_1^2(x), \mu_2^2(x), \mu_3^2(x)\right)\ , \tag{23}$$

where $\mu_i(x)$ are the instantaneous neutrino masses in the medium. The instantaneous mass eigenstates in the medium, $|\nu_i^m\rangle$, and the original mass eigenstates in vacuum, $|\nu_i\rangle$, are related by a unitary transformation $\tilde{U}(x)$ such that

$$|\nu_i\rangle = \sum_{j=1}^{3} \tilde{U}(x)_{ij} |\nu_j^m\rangle\ . \tag{24}$$

For simplicity, we consider a 2×2 case which contains only two neutrino flavours $|\nu_\alpha\rangle$ and $|\nu_\beta\rangle$. Then the H_m in Eq.(21) reduces to $H_m = \frac{1}{2E}\mathrm{diag}\left(m_1^2, m_2^2\right)$. From Eq.(22), the effective neutrino potential in this simplified case is $V = \mathrm{diag}\left(V_\alpha(x), V_\beta(x)\right)$. Without losing generality, the unitary PMNS matrix in 2×2 case can always be parameterized as a real rotation matrix

$$U = \begin{pmatrix} \cos\theta & \sin\theta \\ -\sin\theta & \cos\theta \end{pmatrix}\ . \tag{25}$$

Then one can get $\mu^2_{1,2}(x)$ by computing two eigenvalues of $H(x)$ in Eq.(20)

$$\mu^2_{1,2}(x) = \frac{m_1^2+m_2^2}{2} + E\left[V_\alpha(x)+V_\beta(x)\right] \mp \frac{1}{2}\sqrt{\left[\Delta m^2\cos 2\theta - A(x)\right]^2 + \left[\Delta m^2 \sin 2\theta\right]^2}\,, \tag{26}$$

where $\Delta m^2 = m_2^2 - m_1^2$ and $A(x) \equiv 2E\left[V_\alpha(x) - V_\beta(x)\right]$. The net rotation matrix $U^{\text{net}}(x)$ which links the instantaneous mass eigenstates in the medium and flavour eigenstates is parameterized as follows

$$U^{\text{net}}(x) \equiv U\tilde{U}(x) = \begin{pmatrix} \cos\theta & \sin\theta \\ -\sin\theta & \cos\theta \end{pmatrix}\begin{pmatrix} \cos\tilde{\theta} & \sin\tilde{\theta} \\ -\sin\tilde{\theta} & \cos\tilde{\theta} \end{pmatrix} \equiv \begin{pmatrix} \cos\theta_m & \sin\theta_m \\ -\sin\theta_m & \cos\theta_m \end{pmatrix} \tag{27}$$

such that

$$\begin{pmatrix} \nu_\alpha \\ \nu_\beta \end{pmatrix} = \begin{pmatrix} \cos\theta_m & \sin\theta_m \\ -\sin\theta_m & \cos\theta_m \end{pmatrix}\begin{pmatrix} \nu_1^m \\ \nu_2^m \end{pmatrix}, \tag{28}$$

where the instantaneous mixing angle $\theta_m \equiv \theta + \tilde{\theta}$. The parameterized $\tilde{U}(x)$ can be constructed by computing two eigenvectors of $H(x)$ with unity normalization where

$$\begin{cases} \cos\tilde{\theta}(x) & = \frac{1}{4NE}\, A(x)\sin 2\theta \\ \\ \sin\tilde{\theta}(x) & = \frac{1}{4NE}\left(-\Delta m^2 + A(x)\cos 2\theta + \sqrt{\left[\Delta m^2\cos 2\theta - A(x)\right]^2 + \left[\Delta m^2\sin 2\theta\right]^2}\right) \end{cases}, \tag{29}$$

and N is a mass-dimension factor ensuring the normalisation $\cos^2\tilde{\theta} + \sin^2\tilde{\theta} = 1$. Then the instantaneous mixing angle θ_m in matter is given by

$$\tan 2\theta_m(x) \equiv \tan\left(2\theta + 2\tilde{\theta}(x)\right) = \frac{\Delta m^2 \sin 2\theta}{\Delta m^2\cos 2\theta - A(x)}\,. \tag{30}$$

As seen in Eq.(30), the tangent of instantaneous mixing angle changes sign if the neutrino passes by some certain matter satisfying the *resonance condition*

$$A_R = \Delta m^2 \cos 2\theta\,. \tag{31}$$

The Eq.(31) implies that when the neutrino system travels across a monotonically varying potential, after passing the border where the *resonance condition* holds, the dominant flavour component of a given mass eigenstate changes. This phenomenon is called *level crossing*.

Inserting Eq.(24) back into the evolution Eq.(20) and utilizing Eq.(23), one finds the evolution equation in the instantaneous mass basis reads

$$\mathrm{i}\frac{d\vec{\nu}^m}{dx} = \left[\frac{1}{2E}\mathrm{diag}\left(\mu_1^2(x), \mu_2^2(x), \mu_3^2(x)\right) - \mathrm{i}\,\tilde{U}^\dagger(x)\frac{d\tilde{U}(x)}{dx}\right]\vec{\nu}^m \tag{32}$$

The last term of Eq.(32) in the square bracket indicates that different instantaneous mass eigenstates are coupled and generically they are not energy eigenstates. For constant medium or the medium varying slowly enough, the last term is negligible and instantaneous mass eigenstates can be treated independently as energy eigenstates. This is the *adiabatic* approximation. When the last term is significant, different instantaneous mass eigenstates mix along the neutrino path. Then the evolution is *non-adiabatic.*

For adiabatic evolution, the probability of neutrino flavour oscillations takes a very similar form comparing with its vacuum counterpart Eq.(9). When we neglect CP violation, it reads

$$P_{\alpha\to\beta}(L) = \left|\sum_j U^{\rm net}_{\alpha j}(0)U^{\rm net}_{\beta j}(L)\exp\left(-\frac{\mathrm{i}}{2E}\int_0^L dx'\,\mu_j^2\left(x'\right)\right)\right|^2 . \tag{33}$$

One can always solve the neutrino evolution equation in matter numerically in order to compute $P_{\alpha\to\beta}(L)$.

1.3 Neutrino oscillation experiments

A major reference of subsection 1.3 is **Sec.14.6.3 Accelerator Neutrinos** (pp. 294-297) of *The Review of Particle Physics (2022)* [1].

Neutrino flavour oscillations have been studied using various different neutrino sources and detection techniques. Due to the tiny cross section of neutrino interactions and the long distance needed to oscillate significantly, intense sources and huge detectors are required by the experiments. Besides, the definitive measurement also asks for a good knowledge of neutrino flux before the oscillations.

Since this thesis is about the research relevant to T2K experiment [6, 7], the status of important long-baseline accelerator neutrino experiments is briefly reviewed in this subsection 1.3. And more specific details about T2K experiment will be introduced in section 2.

1.3.1 Accelerator Neutrino Beams

The conventional accelerator neutrino beams are produced by bombarding targets with energetic protons to generate mesons such as pion π and koan K. Then the light mesons will weakly decay to neutrinos. Undecayed mesons and muons are stopped by beam blocks. Because the predominately generated mesons are pions and kaons, the accelerator neutrino beams are mainly muon-type neutrinos with a little contamination of electron-type neutrinos primarily from kaon and muon decays. By focusing the charged parents of neutrinos with a pulsed electromagnet called magnetic horn, the neutrinos or anti-neutrinos can be selected and guided into a specific solid angle range. However, even after the focusing of magnetic horns, *wrong sign* neutrinos still exist in the beams.

From the equation (10), we know that a suitable choice of (L/E) can maximize the probability of a typical type neutrino oscillation to be studied and therefore increase the experimental sensitivity. Thus a narrow energy band of neutrino beams is wanted and neutrinos with irrelevant energies should be suppressed. From the two-body kinematics of the charged pion decay, the energy of muon neutrino ν_μ is

$$E_\nu = \frac{\left[1-(m_\mu/m_\pi)^2\right]E_\pi}{2\gamma^2\left(1-\beta\cos\theta\right)}\ , \tag{34}$$

where $\gamma = E_\pi/m_\pi = 1/\sqrt{1-\beta^2}$ and $\beta c = |\vec{p}_\pi|/E_\pi$ is the speed of the parent pion. θ in the equation (34) is the angle between the tracks of parent pion and neutrino in the lab frame. If we define the beam direction of focused parent pions as a reference axis, the angle θ characterises the off-axis degree of daughter neutrinos. In the high-energy limit and when $|\theta| \ll 1$, the equation (34) can be approximated as

$$E_\nu \approx \frac{\left[1-(m_\mu/m_\pi)^2\right]E_\pi}{1+\gamma^2\theta^2}\ . \tag{35}$$

In principle, by selecting parent pions within a narrow energy interval and receiving the daughter neutrinos at a small angle range $\theta \sim \theta + d\theta$, the neutrino beam with a narrow energy band is obtained. In fact, as shown in Figure 1, for a wide range of E_π, E_ν is much more sensitive to the non-zero off-axis angle θ than to the energy E_π of parent pions. So the off-axis configuration can be applied in experiments for obtaining a narrower energy band neutrino beam.

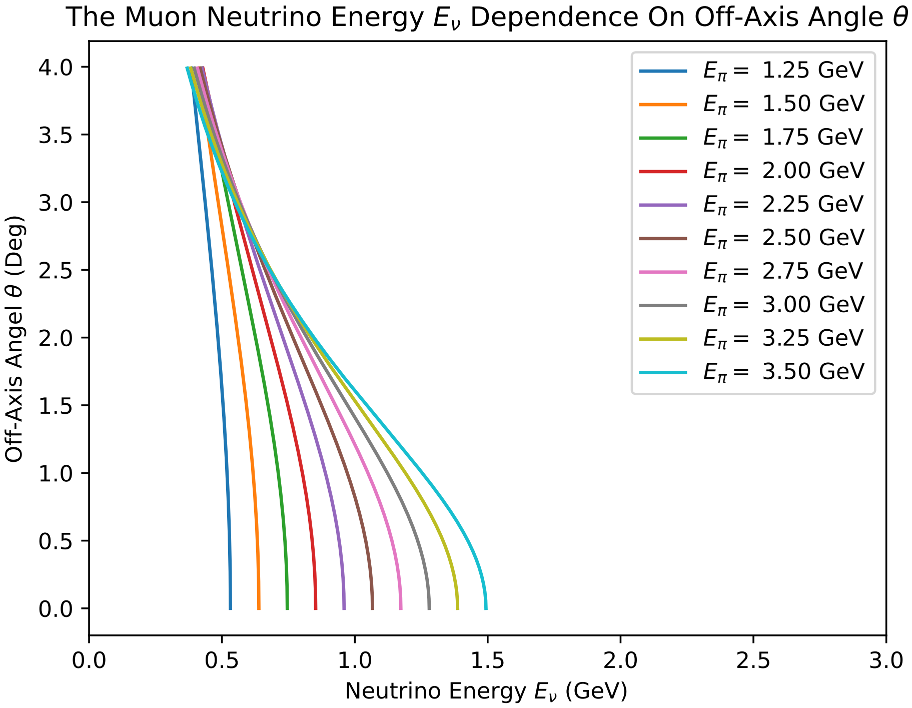

Figure 1: For a wide range of E_π, a non-zero off-axis angle θ can help to get a narrower muon neutrino energy E_ν band.

Regarding the choice of L/E to maximize the intended oscillation probability, the corresponding mass splitting value Δm^2 needs to be inputted to Eq.(11). For example, the ν_μ-disappearance mass splitting $\Delta m^2_{\mu\mu}$ is around $2.5\times10^{-3}\,\mathrm{eV}^2$. By imposing that Eq.(11) equals to $\frac{\pi}{2}$, it indicates that the first maximum of ν_μ disappearance oscillation takes place at about 500 km/GeV. For experiments of which accelerators provide neutrino beams of energy $\sim$ 1GeV, baselines should be around several hundred kilometers to one thousand kilometers to maximize their sensitivities. Thus these experiments are called long-baseline experiments. Meanwhile, some also believe that the possible mass splitting scale might be $\sim 1\,\mathrm{eV}^2$ when a *sterile* neutrino[1] is involved [8], which can be studied over a short baseline of $\sim 1\,\mathrm{km}$ with neutrinos from accelerators, namely short-baseline experiments.

With the help of Monte Carlo simulations corresponding to specific beamline configurations, the flux of neutrino beams produced by accelerators can be estimated. The hadron production cross section is an important input to estimate the flux of neutrino beams. The data of hadron production cross section are taken from dedicated hadron production experiments and the uncertainty in the relevant energy region is around 5% ~ 10%.

1.3.2 Long-baseline Experiments

For a long baseline accelerator neutrino oscillation experiment, due to the non-monoenergetic nature of neutrino beams (see Eq.(34)), one can only measure an averaged oscillation probability $\langle P_{\alpha\to\beta}(L)\rangle$ over an oscillation distance L. Many long-baseline experiments use both a near detector (ND) and a far detector (FD) to reduce the systematic uncertainties arising from neutrino flux and neutrino-nucleus interactions. The near detectors are usually placed hundreds meters away from the production target and measure the neutrino flux as a function of energy spectrum, $\phi(E)$, and the interaction cross section $\sigma(E)$, which are used as input to make predictions of observables at the far detector. The observed oscillation probability $\langle P_{\alpha\to\beta}(L)\rangle$ can be expressed as follows

$$\begin{aligned}\langle P_{\alpha\to\beta}(L)\rangle &= \frac{\int dE\,\frac{d\phi}{dE}\,\sigma^{\beta}_{CC}(E)\,P_{\alpha\to\beta}(L,E)\,\epsilon_{\mathrm{FD}}(E)}{\int dE\,\frac{d\phi}{dE}\,\sigma^{\alpha}_{CC}(E)\,\epsilon_{\mathrm{ND}}(E)} \\ &= \delta_{\alpha\beta} - 4\sum_{j>k}\mathbf{Re}\left\{U^*_{\alpha j}\,U_{\beta j}\,U_{\alpha k}\,U^*_{\beta k}\right\}\left\langle \sin^2\left(\frac{\Delta m^2_{jk}L}{4E}\right)\right\rangle, \\ &+ 2\sum_{j>k}\mathbf{Im}\left\{U^*_{\alpha j}\,U_{\beta j}\,U_{\alpha k}\,U^*_{\beta k}\right\}\left\langle \sin\left(\frac{\Delta m^2_{jk}L}{2E}\right)\right\rangle\end{aligned} \tag{36}$$

where σ^{α}_{CC} is the charged-current cross section of the process in which the neutrino ν_α is detected and $\epsilon_{\mathrm{ND}}(E)$ ($\epsilon_{\mathrm{FD}}(E)$) is the detection efficiency of near detector (far detector). The minimal step of the energy integral is constrained by the energy resolution of the detector.

Tabel 1 [1] summarizes the basic information of important long-baseline neutrino oscillation experiments. K2K was the first long-baseline experiment using a neutrino beam produced from the KEK 12 GeV proton synchrotron. The neutrino beam had an average energy of 1.3 GeV. It passed through a near detector complex and flew towards a far detector called Super-Kamiokande (see more details in sub-subsection 2.2.2) with a 250 km baseline. The near detector complex of K2K consisted of a 1 kilo-ton water Cherenkov detector and a set of fine-grained detectors,

---

[1] *Sterile* neutrinos are defined as having no SM gauge interactions [1]. Therefore, they are singlets of the complete SM gauge group and absent in the SM.

located at about 300 m downstream of the production target [9]. K2K confirmed the muon neutrino disappearance originally reported by Super-Kamiokande atmospheric neutrino observation.

Name	**Beamline**	**Far Detector**	**L (km)**	**E_ν (GeV)**	**Year**
K2K	KEK-PS	Water Cherenkov	250	1.3	1999-2004
MINOS	NuMI	Iron-scintillator	735	3	2005-2013
MINOS+	NuMI	Iron-scintillator	735	7	2013-2016
OPERA	CNGS	Emulsion hybrid	730	17	2008-2012
ICARUS	CNGS	Liquid argon TPC	730	17	2010-2012
T2K	J-PARC	Water Cherenkov	295	0.6	2010-
NOvA	NuMI	Liquid scint. tracking calorimeter	810	2	2014-
DUNE	LBNF	Liquid argon TPC	1300	2-3	
Hyper-Kamiokande	J-PARC	Water-Cherenkov	295	0.6	

Table 1: List of long-baseline neutrino oscillation experiments [1]

MINOS, MINOS+ based at Fermilab combined data from both accelerator and atmospheric neutrinos to measure oscillation parameters. The European OPERA experiment, using the CNGS beamline from CERN to LNGS (Laboratori Nazionali del Gran Sasso), confirmed $\nu_\mu \to \nu_\tau$ oscillation in appearance mode with a statistical significance of 6.1σ. There was no near detector in CNGS because it was not needed for the ν_τ appearance search, since both parent kaons K and parent pions π are lighter than tau $\tau^\pm$ and cannot decay to τ^- (τ^+) and $\bar{\nu}_\tau$ (ν_τ). Another European experiment ICARUS was also operated in Gran Sasso in Italy, using the CNGS beamline as well.

All the aforementioned first generation of long-baseline experiments confirmed the existence of neutrino oscillation. The major goal of second generation experiments was the observation of $\nu_\mu \to \nu_e$ oscillation. Combining the data from both neutrino and anti-neutrino appearance mode, people can search for CP violation in the neutrino mixing. Measurement of the mass ordering and the octant θ_{23} is also applicable.

The T2K experiment was started in 2010 using a newly constructed high-intensity proton synchrotron called Japan Proton Accelerator Research Complex (J-PARC) and the Super-Kamiokande detector. It is the first long-baseline experiment to employ the off-axis neutrino beam. The off-axis angle of 2.5° was chosen to set the peak of the neutrino energy spectrum at 0.6 GeV, matching the first maximum of ν_μ disappearance oscillation probability at the 295 km baseline for $\Delta m^2_{\mu\mu} \sim 2.5 \times 10^{-3}\,\mathrm{eV}^2$. T2K has a set of near detectors complex (ND280) at about 280 m from the production target. In 2011, T2K reported the first indication of $\nu_\mu \to \nu_e$ oscillation with a statistical significance of 2.5σ. In the framework of 3ν mixing, it corresponds to detecting non-zero amplitude generated by the mixing angle θ_{13}(see Eq.(15)). Later $\nu_\mu \to \nu_e$ oscillation was established by T2K with more than 7σ in 2014. By a combined analysis of the neutrino and antineutrino data, T2K reported a hint of CP violation at the 2σ level.

The NOvA experiment uses the upgraded NuMI beamline with an off-axis configuration. The physics run of NOvA was started in 2014. After confirmation of $\nu_\mu \to \nu_e$ from ν_μ beam, NOvA started data taking with anti-neutrino beam in 2016. Using the $\bar{\nu}_\mu$ beam data, NOvA has reported the observation of $\bar{\nu}_\mu \to \bar{\nu}_e$ with 4.4σ significance. Some values of the CP-violating phase δ_{CP} (see

Eq.(15)) have been excluded for the inverted mass ordering ($m_3 \ll m_1 < m_2$), while no significant limit has been set for the case of normal mass ordering ($m_1 \ll m_2 < m_3$).

Two large-scale long-baseline experiments are under preparation. DUNE will be a 1,300 km long-baseline experiment based in the US. The Hyper-Kamiokande detector in Japan will be the successor of the Super-Kamiokande detector. It will be a water Cherenkov detector with 260 kt total water mass. With upgrades to the existing accelerator and beamline, J-PARC will provide a 1.3 MW neutrino beam to Hyper-Kamiokande with a baseline of 295 km. Both DUNE and Hyper-Kamiokande will have a rich physics program besides the long-baseline experiment, such as searches for proton decays and study of supernova neutrinos.

1.4 Motivations

For a long baseline neutrino oscillation experiment, from Eq.(36), it is evident that a very good knowledge of the denominator factor $\frac{d\phi}{dE}\sigma^{\alpha}_{CC}(E)\,\epsilon_{\mathrm{ND}}(E)$ is required for a precise measurement of the oscillation probability $\left\langle P_{\alpha\to\beta}(L,E)\right\rangle$ and further extractions of oscillation parameters (Eq.(15)). To achieve this goal, it is crucial to equip a near detector complex (i.e. before neutrino oscillations) capable of accurate neutrino energy reconstruction, accurate neutrino-nucleus cross section measurement and high event detection efficiency.

However, those three factors are correlated and have to be improved together. If we consider a segmented scintillator detector as an option, requirements are as follows. For an accurate energy reconstruction of an incident neutrino, a fine granularity is needed for identifying all neutrino-nucleus interaction final states without missing extremely short tracks from the vertex or mixing several collinear tracks as a single track. When it comes to the neutrino-nucleus cross section measurement, it is heavily influenced by the so-called nuclear effects such as Fermi motion, binding energy, nucleon-nucleon correlation and final-state interactions. The nuclear effects can produce various final-state hadrons including protons, neutrons, pions and even other nuclei. Most of hadrons primarily generated by nuclear effects have very short track lengths and are densely attached to the interaction vertex. To reduce the systematic uncertainties originated from nuclear effects, ideally, we have to develop a beyond state-of-the-art fine-grained detector which can reconstruct kinematics of all final-state hadrons. By the way, the neutrino energy measurement is also smeared and biased by nuclear effects. Because from detectors' perspective, the energy transferred within the nucleus is invisible. Thus both the neutrino cross section measurement and neutrino energy reconstruction long for a very fine-grained neutrino-active detector which can offer an accurate description of vertex activities. As for improving event detection efficiency, it is necessary to have a huge mass ($\sim$ tons) of neutrino-active materials to compensate the extremely small neutrino interaction cross section. Besides, a set of highly efficient sensors and electronics readout is also vital for improving both neutrino energy resolution and event detection efficiency.

Overall, a ton-scale neutrino-active Hyper-Fine-Grained Detector (HFGD) with decent photosensing readout becomes a fairly convincing solution as an integrated part of a near detector complex. It can provide an accurate description of neutrino-nucleus vertex activity, an outstanding collinear tracks distinguishing ability and high reconstruction efficiency of extremely short tracks, e.g. protons whose momenta are below 200 MeV/c and track lengths are shorter than few-mm.

The aim of this thesis is about the software development and the detector performance estimation for physical analysis on a novel HFGD which mainly consists of polystyrene-based sub-mm scintillating fibers (SciFi). Comparing to other option such as a High-Pressure Time Projection Chambers (HpTPC), the denser plastic scintillator requires a much smaller magnetised volume and hence it is significantly more economical [10].

For future applications, the novel HFGD might be applied as a replacement of one of the current Fine Grained Detectors (FGDs) for the next upgrade (i.e. ND280++) of the upgraded T2K off-axis near detector (i.e. ND280+). The details of the upgraded T2K off-axis near detector can be found in sub-subsection 2.2.1.

2 The T2K Experiment

Major references of section 2 are T2K Experiment official websites [6, 11], the instrumentation review article *The T2K experiment* [7] and *T2K ND280 UPGRADE TECHNICAL DESIGN REPORT* [12].

T2K (Tokai to Kamioka) experiment is a long baseline accelerator neutrino experiment in Japan, focusing on neutrino oscillation study. A search for $\nu_\mu \to \nu_e$ oscillations was performed by T2K and the collaboration announced the first experimental evidence of them in June 2011 [6]. And these ν_e appearances in ν_μ beam had never been observed by any previous experiments. The latest-known lepton sector mixing angle θ_{13} could be measured by observing $\nu_\mu \to \nu_e$ oscillations. T2K is also performing measurements of oscillations $\nu_\mu \to \nu_\tau$ (which had already been observed in previous experiments). And a precise measurement of oscillation parameters, Δm^2_{32} and $\sin^2\theta_{23}$ was conducted by ν_μ disappearance studies [13].

Other goals of the experiment include various neutrino cross section measurement and sterile neutrino (see footnote 1) searches [7].

2.1 T2K Neutrino Beam

A high-luminosity ν_μ or $\bar{\nu}_\mu$ beam is sent from Tokai at the east coast of Japan to Kamioka which is 295 km westward. The muon neutrinos are produced by bombarding a graphite target with 30 GeV proton beam from Japan Proton Accelerator Research Complex (J-PARC)[7]. The interactions between protons and carbon nucleus produce plenty of mesons which are mainly charged pions $\pi^\pm$ and kaons $K^\pm$. The pions and kaons are selected by their electric charges and focused by magnetic horns to form a beam. $\pi^\pm$ and $K^\pm$ will decay rapidly into muons and muon neutrinos via weak charged currents, i.e. $\pi^+/K^+ \to \mu^+ + \nu_\mu$ and $\pi^-/K^- \to \mu^- + \bar{\nu}_\mu$. Meanwhile, 0.01% or so charged pions (greatly suppressed by the left-handedness nature of neutrinos and helicity (spin) conservation) and around 5% charged kaons will primarily decay to produce electron neutrinos ν_e ($\bar{\nu}_e$). Some muons will also decay to produce electron neutrinos. They contribute to about 1% electron neutrino contamination in a muon neutrino beam. The adjustment of electric current direction in magnetic horns can select either ν_μ or $\bar{\nu}_\mu$ beam from π^+ or π^- decays, respectively. 75 tons of graphite (3.174 m long, 1.94 m wide, 4.69 m high) and 15 iron plates with a total iron thickness of 2.40 m are used as a beam dump to filter out muons, undecayed pions and remaining protons. However, most of neutrinos can pass through the beam dump easily because of their extremely tiny cross sections purely contributed by the weak interaction[6].

The knowledge of the neutrino beam flux and its energy spectrum is imperative for the oscillation experiment. The energy spectrum of T2K neutrino beam is peaked at 0.6 GeV and the first maximum ν_μ disappearance probability occurs at about 295 km away from the graphite production target [6].

2.2 The T2K Detectors

There are two sets of detectors installed for the T2K experiment.

One is a near detector complex (ND280) located at about 280 meters away from the production target. ND280 consists a magnetized off-axis tracking detector and a separate array of on-axis iron/scintillator detectors called Interactive Neutrino GRID (INGRID).

Another is a far land-based water Cherenkov detector named Super-Kamiokande (Super-K) located 295 km west of the beam source and used to sample the beam's flavor composition and look for $\nu_\mu \to \nu_e$ appearance and ν_μ disappearance [7].

2.2.1 Near Detector Complex (ND280)

The off-axis detector of ND280 is used to measure the flux, energy spectrum and electron neutrino contamination in the direction of the far detector, along with measuring rates for exclusive neutrino reactions [7]. All of these measurements are utilized to characterize signals and backgrounds in the Super-Kamiokande detector [7]. The current off-axis angle is 2.5° and it can be adjusted between 2.0° and 2.5°. The off-axis near detector ND280 is in use since the commissioning of the T2K experiment in 2009, and has played a major role in constraining systematic uncertainties, ultimately contributing to sufficient precision for the discovery of $\nu_\mu \to \nu_e$ oscillations [11]. However, the original off-axis near detector is still constrained to angular acceptance of mostly forward going events, and in addition the reconstruction of short tracks is limited. Thus, not every type of neutrino interaction can be analysed with sufficient precision [11]. With the upgrade of J-PARC beam towards higher power, the off-axis ND280 is undergoing a major upgrade as well, which will be completed in 2023. The goal of this off-axis ND280 upgrade is to improve the Near Detector performance to measure the neutrino interaction rate and to constrain the neutrino interaction cross sections so that the uncertainty in the number of predicted events at Super-Kamiokande is reduced from around 6% to about 4% [12]. This goal is achieved by modifying the upstream part of the detector, adding a new highly granular scintillator detector named Super-Fine-Grained Detector (Super-FGD) with full angular acceptance and three perpendicular readout planes, two new TPCs (High-Angle TPC) and six TOF planes [12]. The upgraded off-axis ND280 will match the needs of the T2K-II phase experiment whose aim is to provide a 3σ exclusion of CP conservation for 36% of the δ_{CP} phase space, if the neutrino mass ordering is known [12].

The components of the upgraded off-axis detector are shown in Figure 2 [11]. The ND280 off-axis detector is built around the old CERN UA1/NOMAD magnet providing a dipole magnetic field of 0.2 T, to measure momenta in time projection chambers (TPCs) with good resolution and determine the sign of charged particles produced by neutrino interactions [7]. In the upstream part (on the left in Figure 2), the Super-Fine-Grained Detector (Super-FGD) based on $1\,\mathrm{cm}^3$ scintillating cubes is sandwiched between two High Angle Time Projection Chambers (HA-TPCs). Six Time of Flight planes (TOF) surround both SuperFGD and HA-TPCs. In the downstream part, there are three TPCs sandwiching two Fine Grained Detectors (FGD) based on scintillator bars and layers of water. As for calorimeters, there are three Electromagnetic Calorimeters (ECals): the most upstream P0DEcal as a veto and to detect neutral particles [12], the Barrel ECal and the Down Stream ECal.

A tiny portion of muon neutrinos ν_μ interact with the water or scintillator from either two FGDs or the SuperFGD. Many of these muon neutrino interaction events produce final-state muons, protons, neutrons and pions. The produced charged particles will leave their tracks information by scintillation in scintillators or ionizing the gas in the TPCs. Then, under some certain efficiencies, the energy, momentum and identity of these particles can be reconstructed accordingly.

In addition to the off-axis detector, the on-axis INGRID (Interactive Neutrino GRID) shown in Figure 3 [7] is a neutrino detector centered on the neutrino beam axis. It consists of an interactive network of vertical and horizontal iron/scintillator modules which provide daily check of the neutrino beam direction and intensity by means of neutrino interactions in iron [6].

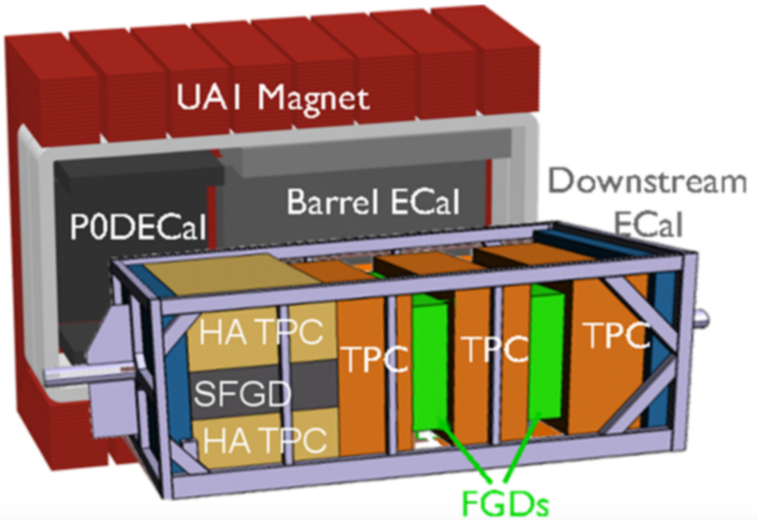

Figure 2: The scheme of the upgraded off-axis detector of ND280 (TOF sub-detectors not visible) [11]

2.2.2 Super-Kamiokande Far Detector

The Super-Kamiokande (Super-K) is located 1,000 meters underground within the center of Mt. Ikenoyama and is about 295 km west of the production target in Tokai [7]. Super-K contains a very large cylinder of 50 kton ultra-pure water. It is the world's largest water Cherenkov detector [14]. The walls of Super-K are covered with more than 10,000 sensitive photo-multipliers (PMT).

Most of the neutrinos passing through the off-axis detector of ND280 without any interactions. They travel to the Super-K at almost the speed of light. At the Super-K detector, most of neutrinos do not interact with water as well. However, due to the high energy and intensity of the beam as well as the huge amount of target water, a tiny portion of them do interact. If they interact with water via weak charged currents, muon neutrinos ν_μ will produce muons μ^- and electron neutrinos ν_e will produce electrons e^-. Most of the produced muons and electrons travel faster than the phase speed of light in water (i.e. three-quarters of vacuum light speed) hence they radiate the Cherenkov light. The walls of PMT then will detect photon rings from Cherenkov radiation. Super-K can distinguish muons' well-defined clear sharp rings from electrons' fuzzy rings [7]. Thus, in an over-simplified

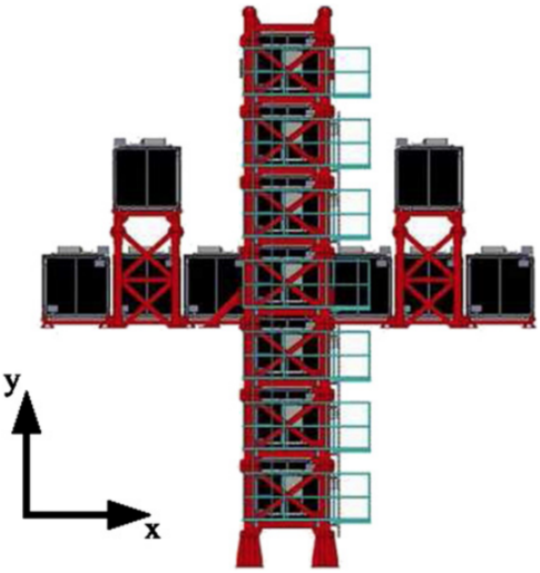

Figure 3: INGRID on-axis detector [7]

version, the oscillations from muon neutrinos ν_μ to electron neutrinos ν_e were seen in Super-K as the diffuse rings from electrons produced by interactions of electron neutrinos ν_e with water [6]. In the real experiment, the confirmation of $\nu_\mu \to \nu_e$ oscillations was made by comparing the flux of neutrinos at Super-K predicted by ND280 with the null hypothesis (i.e. if there are no $\nu_\mu \to \nu_e$ oscillations) and the actual neutrino flux measured by Super-K itself. All backgrounds (e.g. the ν_e contamination in the ν_μ beam) and uncertainties (both statistical and systematic) were taken into consideration for a convincing confirmation.

2.3 Advantages of Off-Axis Experiment

T2K is the world's first off-axis neutrino experiment, with ND280 and Super-K positioned 2.5 degrees away from the centre of the neutrino beam [6]. As mentioned in subsection 1.3.1, the off-axis neutrino beam has a narrower energy band comparing with the on-axis one's. For T2K neutrino beam configuration, the incident neutrino energy spectrum with respect to off-axis angle is shown in Figure 4 [11]. Therefore, from Eq.(10), the range of L where the oscillation probability reaches its first maximum is also narrower and more centered around the spot of Super-K. Thus, with such an off-axis configuration, a larger fraction of muon neutrinos ν_μ in the beam will change their flavours when arriving at the Super-K comparing to that of an on-axis experiment, which increases the sensitivity of oscillation analysis.

Besides, the most important measurement at ND280 is the flux of incident neutrinos as a function of their energies. This measurement is made most accurately with the so-called Charged-Current Quasi-Elastic (CCQE) event which a muon neutrino ν_μ exchanges a virtual charged weak boson (i.e. $W^\pm$) with a quasi-free neutron in nucleus and produces a muon μ^- and a proton in its final state [6]. The off-axis part of the beam whose narrower energy band E_ν peaked at 0.6 GeV has a larger fraction of these events than the on-axis part (see contributing processes to the total

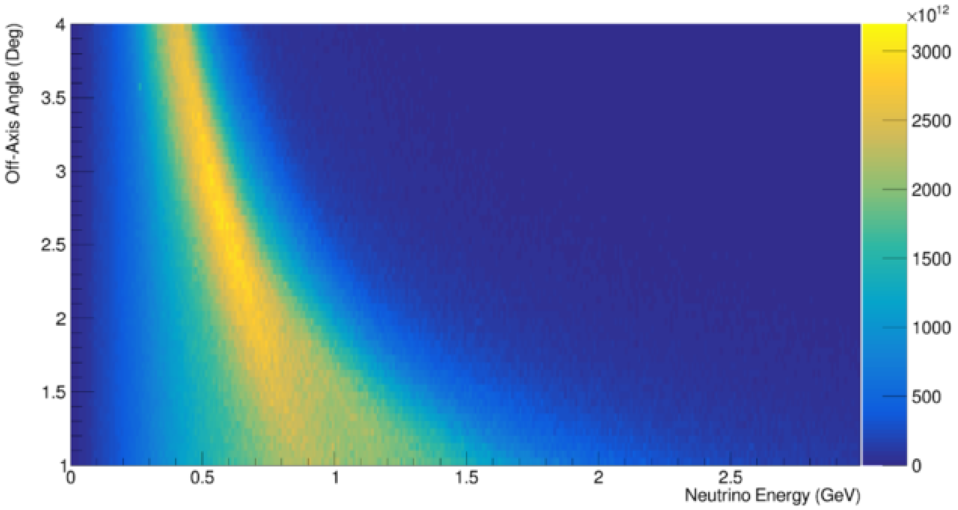

Figure 4: Neutrino energy spectrum with respect to off-axis angle [11]

neutrino ν cross section in Figure 5 [15]), which enables T2K to make more accurate measurements of neutrino energies.

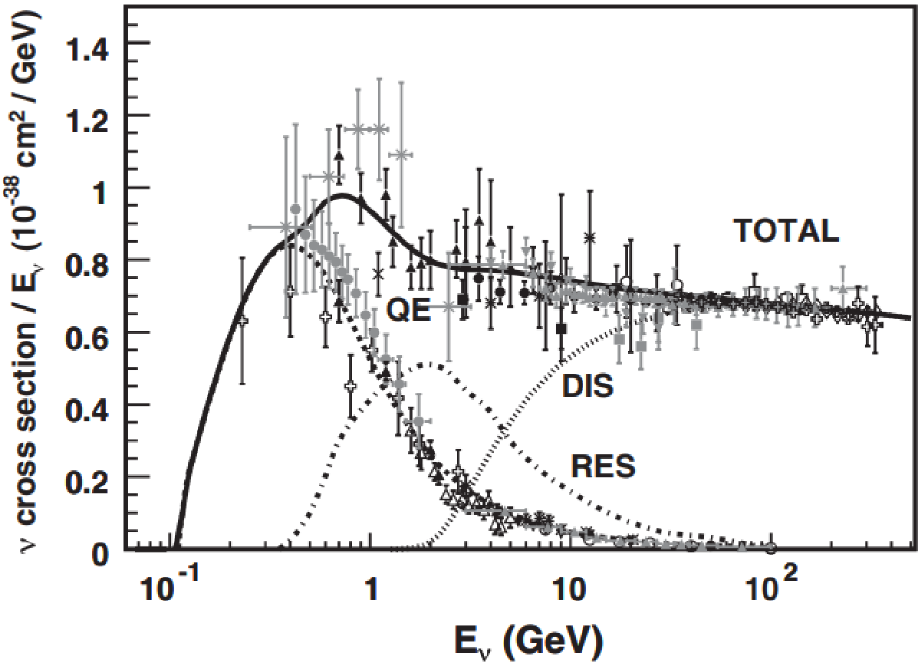

Figure 5: Total neutrino per nucleon charged-current cross sections (for an isoscalar target) divided by neutrino energy and plotted as a function of energy. Also shown are the various contributing processes including quasi-elastic (QE) scattering (dashed), resonance (RES) production (dot dashed), and deep inelastic scattering (DIS) (dotted) [15].

All of these advantages lead to more precise measurements of neutrino oscillation parameters than those previous on-axis experiments.

3 HFGD Designs And Detector Response

Two kinds of polystyrene-based scintillators are simulated as basic compositions of the Hyper-Fine-Grained Detector (HFGD): Scintillating Cubes and Scintillating Fibers (SciFi). The details of Scintillating Cube and Scintillating Fibers are introduced in subsection 3.1 and 3.2, respectively. Two possible designs of HFGD are proposed. The first one is a Hybrid Design (details in subsection 3.3) by combining 1 cm^3 scintillating cubes and 0.5-mm-diameter SciFi. The second one is a Pure SciFi Design (details in 3.4) using hyper-fine SciFi with merely 0.25-mm diameter. NEUT [16] and Geant4 [17, 18, 19] as applied softwares for HFGD simulations are introduced in subsection 3.5. A parameterized analytical simulation algorithm for HFGD detector response is explained in details in subsection 3.6. At last, some event displays are presented in subsection 3.7 to visualise the detector responses to the most important CCQE events.

3.1 Scintillating Cube

The composition of scintillating cubes (Super-FGD like) is polystyrene doped with 1.5% of para-Terphenyl (PTP) and 0.01% of POPOP as primary and secondary luminophores [12]. The size of each cube is 1.027 cm × 1.027 cm × 1.027 cm with the active volume to be 1 cm^3 sharp. The inactive region is spared for reflecting layers which optically isolate one cube from another. For each scintillating cube, it has two holes in x and y directions which are orthogonal to the neutrino beam direction (i.e. z direction) and perpendicular to each other. The Wavelength Shifting Fibers (WLS fibers) are inserted into holes to collect scintillation photons generated by energy depositions from charged particles. Then WLS fibers will down-shift the original ultraviolet (UV) photons to lower-energy visible photons which have a much longer attenuation length in fibers. The end of each WLS fiber is connected to a Silicon PhotoMultipliers (SiPM) as a readout which converts analog signal (scintillation photon) to digital signal (the current initiated by photoelectrons (p.e.)). If we assemble many scintillating cubes together to form a segmented detector, it could provide projections of charged particle trajectories onto two planes (i.e. xz plane and yz plane), as well as the information of energy deposition (i.e. the number of detectable photons or equivalently photoelectrons) of each hit.

However, the 1 cm granularity of the cube is not fine enough to detect the low-energy proton whose momentum is below 200 MeV/c, with a mere few-mm or even sub-mm track length in plastic scintillators. As mentioned in subsection 1.4, a good knowledge of low-energy final-state protons is vital for the neutrino-nuclei cross section characterisation. Thus the sub-mm-diameter SciFi becomes an irreducible element for the HFGD, which will be introduced in subsection 3.2 below.

3.2 Scintillating Fibers

The current high-performance SciFi is made of polystyrene containing a type of new luminophores called Nanostructured Organosilicon Luminophores (NOLs) [20]. Comparing to the traditional luminophores, it is highly efficient in down-shifting UV photons and has much shorter photoluminescense decay time (i.e. much faster scintillation).

N SciFi can be assembled parallelly into a $(N \times 1)$ slice. Every SciFi in a specific $(N \times 1)$ SciFi slice is aligned either along x direction (X or yz SciFi slice) or y direction (Y or xz SciFi slice), where two directions are orthogonal to each other. And the xy plane is perpendicular to the incident neutrino beam which is along z direction. Apart from that, xz SciFi slice and yz SciFi slice are alternatively arranged one after another, so that two consecutive SciFi slices can provide a complete 3D spatial coordinate (x, y, z_{mean}) from two hits (x, z_1) and (y, z_2).

Two kinds of SciFi with different diameters and slightly different lengths are chosen for building two designs of HFGD. For the Hybrid Design, 0.50-mm-diameter scintillating fibers whose lengths are identically 2053.77 mm are applied. As for the Pure SciFi Design, state-of-the-art 0.25-mm-diameter hyper-fine scintillating fibers with 2000.00 mm length each are utilized to form it.

3.2.1 Photosensors for Scintillating Fiber Readout

Since the diameter of SciFi is sub-mm, a block of SciFi slices of meter scale demands a tremendous number of readout channels (around or beyond 10^6), if one SciFi is associated with one SiPM. Without sacrificing spatial resolution (i.e. one SiPM per SciFi end), the cost of electronics can be prohibitively expensive. One plausible method is applying a new type of photosensor consisting Single-Photon Avalanche Diode (SPAD) array sensors [10]. Comparing with SiPMs converting scintillation photons into photoelectrons in its active area with a time resolution of $\mathcal{O}(100\,\text{ps})$, SPAD arrays can offer both time and position information of each single detected photon with a spatial resolution of the size of a pixel pitch ($\sim 2\,\mu\text{m}$). In this way, each SPAD pixel can function as an independent readout channel. Ideally, without compromising spatial resolution, SciFi bundles coupling to well-developed SPAD arrays can effectively reduce the costs of readout electronics. Because the area of each SPAD pixel is much smaller than the area of SciFi cross section, the number of SPAD arrays needed for readouts only scale with the coupled readout surface area of a SciFi detector rather than the number of SciFi used to construct the detector. For example, for a $2\,\text{m} \times 2\,\text{m} \times 1\,\text{m}$ rectangular solid SciFi detector, both its xz-view and yz-view areas are identically $2\,\text{m}^2$. If 0.50-mm-diameter SciFi with 2000-mm length are adopted for constructing this detector, it needs 8×10^6 channels, for readouts installed at only one side of the SciFi end. If we use 0.25-mm-diameter SciFi with 2000-mm length to assemble a same-size detector, it consists of 32×10^6 SciFi, which requires four times of the number of channels of the same-size 0.50-mm-diameter SciFi detector. However, since each SPAD pixel pitch ($\sim 2\,\mu\text{m} \ll 250\,\mu\text{m} < 500\,\mu\text{m}$) is able to readout as an independent channel, the number of SPAD array sensors needed for readouts does not change as long as the xz-view and yz-view areas of the detector are invariant.

The SPAD which we already have in the laboratory is called SwissSPAD2-μlens [10]. It consists of SwissSPAD2 together with microlens on each pixel to focus photons hence increase the effective fill factor. The photon detection efficiency (PDE) of SwissSPAD2-μlens for 450 nm light is approximately

6% from measurements [10]. Several methods such as increasing the fill factor by improving the SPAD architecture, installing SPAD on both ends of SciFi or adopting the suitable SciFi to match the peak photon detection probability of SPAD are proposed to improve its PDE [10].

3.3 The Hybrid Design

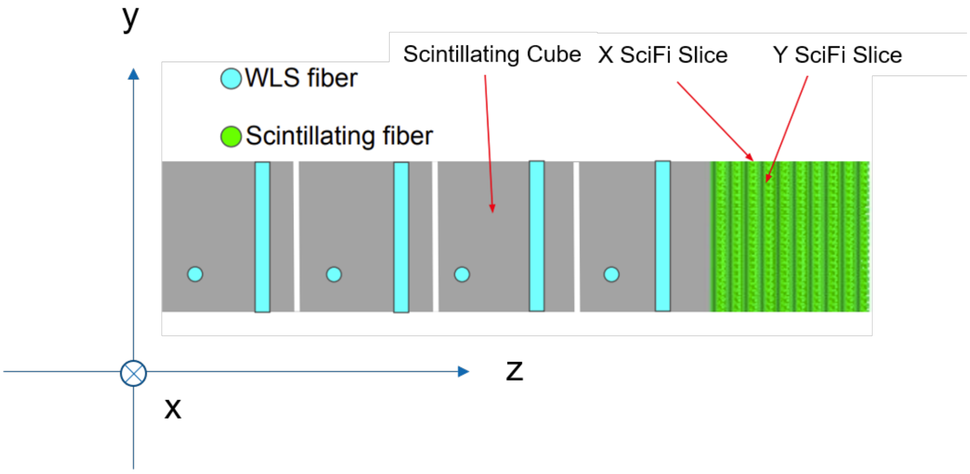

Figure 6: A Basic Unit of A Single Module of The Hybrid Design

SciFi	Diameter/mm	xy Spacing/mm	z Spacing/mm	Length/mm	the Number per Slice
Value	0.50	0.51	0.60	2053.77	4,027

Table 2: The Geometry Parameters of The SciFi Component of The Hybrid Design

A basic unit of the hybrid design of HFGD by combining scintillating cubes and SciFi is illustrated in Figure 6. The whole hybrid design is a (2054.00 mm × 2054.00 mm × 1008.52 mm) rectangular solid. There are 19 duplicate modules in total for the hybrid design. And for each module, it contains 10 layers of $(Y + X)$ SciFi Slices behind 4 layers of (200 × 200) scintillating cubes. The geometry information of the 0.50-mm-diameter SciFi adopted in the hybrid design are listed in Table 2.

3.4 The Pure Scintillating Fiber Design

SciFi	Diameter/mm	xy Spacing/mm	z Spacing/mm	Length/mm	the Number per Slice
Value	0.25	0.25	0.25	2000.00	8,000

Table 3: The Geometry Parameters of The Hyper-fine SciFi of The Pure Design

A pure SciFi design only composed of 0.25-mm-diameter hyper-fine SciFi is also proposed. A part of it is depicted in Figure 7. The geometry parameters of the hyper-fine SciFi for the pure design are shown in Table 3. There are 2,000 $(X + Y)$ SciFi slices in total for the pure SciFi design, which makes it (2000.00 mm × 2000.00 mm × 1000 mm) sharp in size and very similar to the total size of the hybrid design.

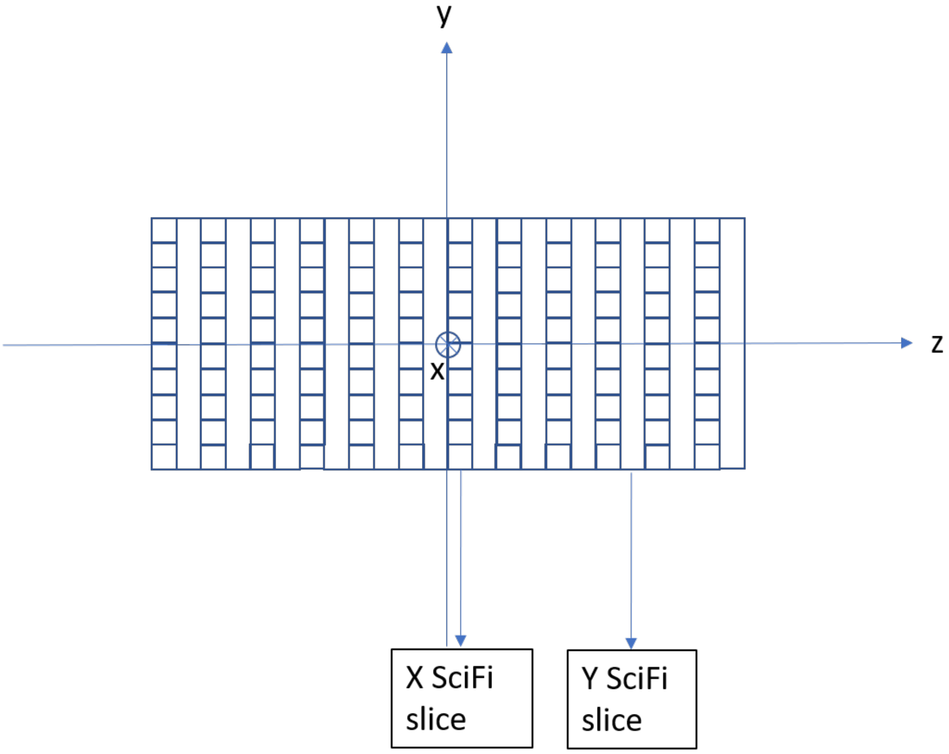

Figure 7: A Part of The Pure SciFi Design

3.5 Simulation Software

3.5.1 NEUT

The neutrino interactions with nucleons and nuclei such as Hydrogen, Oxygen and Carbon can be simulated in a widely applied program library called NEUT [16]. By applying NEUT with the T2K muon neutrino ν_μ energy flux, the final-state particles of ν_μ-nucleus interactions including all known contributing modes, as well as their initial positions and energy-momenta can be obtained. Then, the physical information of final-state particles is stored in the format of a ROOT [21] file. This ROOT file is input to the Geant4 [17, 18, 19] software to simulate the passage of final-state particles through HFGD.

3.5.2 Geant4

Geant4 [17, 18, 19] (for GEometry ANd Tracking) is a very powerful toolkit developed by CERN Geant4 Collaboration for "the simulation of the passage of particles through matter" using Monte Carlo methods. It is widely applied in most of particle physics experiments as simulation frameworks. In this thesis, the software simulation of particles passage through two designs of HFGD is based on Geant4 version geant4-10-05. For the hybrid design, the Geant4 simulation is developed on the basis of ND280 software [22]. Whilst for the pure SciFi design, the Geant4 simulation is programmed independent of any other softwares.

3.6 Detector Response

In this subsection 3.6, the detector response from an energy deposition (as an output of Geant4 simulation) of a Geant4 step from a charged particle to the eventual number of detectable scintillation photons or equivalent photoelectrons (p.e.) is introduced. The detector response is analytically calculated by applying parameterized formulas and it is independent of Geant4 simulations. Therefore, it grants enough freedom of tuning SciFi and SPAD responsive parameters, which is suitable for detector R&Ds. Besides, comparing with computationally expensive optical Monte Carlo simulations, the application of parameterized formula is much more efficient and also precise enough for relevant studies in the thesis. The following three steps including light quenching corrections, scintillation photon trappings and attenuation in SciFi, and the photon detection efficiency of SPAD photosensors are sequentially introduced and applied after Geant4 simulations to get various detector response configurations.

3.6.1 Light Quenching in Polystyrene

Light quenching refers to any process that decreases the intensity of scintillation light yield [23]. It is caused by any possible non-radiative de-excitation process in which most of the excitation energy is degraded to heat rather than yielding light, hence quenching [24]. For the organic scintillator, the energy deposition of a charged particle is due to its electromagnetic interaction with scintillator molecules. Then a part of its kinetic energy is radiated to either excite or ionize the molecules. The π valence bond (e.g. the cyclic π bond of the benzene of the polystyrene) of the excited molecule (exciton) is responsible for scintillation via the standard photophysical transitions. The ions may recombine to excitons as well [1]. However, for densely ionizing particles (i.e. large dE/dx) like protons or α-particles, a local concentration of ions is so significant that they function as quenching agent to couple excitons non-radiatively to ground states, where the excitation energy is transferred to heat. Thus the larger the dE/dx is, the higher percentage of the deposited energy is quenched to heat instead of yielding light.

For organic scintillators, this non-linear effect between dE/dx and effective light yields is well described by a semi-empirical formula named Birks' Law [25]

$$\frac{dE_{\text{eff}}}{dx} = \frac{\frac{dE}{dx}}{1 + kB\frac{dE}{dx}}\,, \tag{37}$$

where dE_{eff}/dx is the effective light-yield energy loss per unit path. kB is named as Birks' coefficient whose value is 0.126 mm/MeV for the polystyrene-based scintillator and it is large enough to compensate polystyrene-based calorimetry. Due to non-negligible light quenching effects in our polystyrene-based HFGD, the energy deposition has to be corrected by Birks' Law for a reliable light yield computation.

When applying the Birk's Law Eq.(37), dE is taken to be the energy deposition per Geant4 step and dx is the length of each Geant4 step. After light-quenching corrections, the steps of a charged particle passage within one SciFi are merged to a single SciFi hit. The first step position inside each SciFi is regarded as the truth position of the hit. The effective deposited energies of all steps within one SciFi are summed up as the effective deposited energy of the hit, denoted by $E_{\mathrm{eff}}^{\mathrm{SciFi\,Hit}}$. After merging, for an arbitrary charged particle, there is at most one hit per SciFi along its passage in HFGD.

3.6.2 Photon Trapping and Attenuation in Scintillating Fiber

For polystyrene-based scintillators, the light yield efficiency is roughly 10 scintillation photons per KeV of effective deposited energy. The SciFi photon trapping efficiency is hard-coded to be 7% to match the measurement (see sub-subsection 3.6.3). The SPAD array sensors are installed at the positive end (i.e. the end with the larger x or y coordinate for X or Y SciFi, respectively) of each SciFi. Since the scintillation is isotropic, only 50% of trapped photons head to the readout direction.

The photon attenuation in SciFi from a hit spot to the corresponding SciFi end coupled with SPAD can be approximated by a single exponential attenuation (Single Exp. Att.) formula [26] with a 4000-mm attenuation length

$$LY_{\mathrm{SciFi\,End}} = LY_{\mathrm{Hit\,Spot}} \times \exp\left(-\frac{x\,[\mathrm{mm}]}{4000\,\mathrm{mm}}\right), \tag{38}$$

where x is the distance between the hit and the corresponding readout SciFi end, $LY_{\mathrm{Hit\,Spot}} \equiv E_{\mathrm{eff}}^{\mathrm{SciFi\,Hit}}\,[\mathrm{KeV}] \times 10\ \mathrm{photons/KeV} \times 50\%$ is the effective light yields at hit spot for readout, and $LY_{\mathrm{SciFi\,End}}$ stands for the number of photons reaching the readout SciFi end after optical attenuation.

3.6.3 Photon Detection Efficiency

Due to the limited photon detection efficiency (PDE) of the SPAD introduced in sub-subsection 3.2.1 above, the number of detectable photons (or equivalent photoelectrons (p.e.)) is calculated by the formula below

$$\text{the number of p.e.} = \sum_{i=1}^{\mathrm{int}(LY_{\mathrm{SciFi\,End}})} 1 \times \mathrm{if}\,(\text{Random Number 0 to 1} < \text{PDE value})\ . \tag{39}$$

Overall, combining all three steps above, for the current SwissSPAD2-μlens with 6% PDE, the net conversion from the effective deposited energy to the number of photoelectrons (p.e.) regardless attenuation is 21 p.e./MeV, which is consistent with data from the $^{90}_{38}$Sr test.

Meanwhile, SPAD array sensors with much higher PDE for better reconstructed energy resolutions are still under R&Ds. In order to estimate the improvement of HFGD performance by promoting SPAD PDE, an improved 25% PDE value is also applied as a comparison to the nominal 6% PDE.

3.7 Event Displays

Performing event displays is an effective method to check geometry consistencies and response correctness of simulation results. For example, a typical Charged-Current Quasi-Elastic (CCQE) event of ν_μ-Carbon interaction with one muon and one proton as final states is displayed in Figure 8. The color scales stand for the number of scintillation photons at SciFi end right after single exponential attenuation Eq.(38) and just before taking SPAD PDE into consideration. The cross sections of scintillating cubes and SciFi are also plotted and consistent to the intended geometry design.

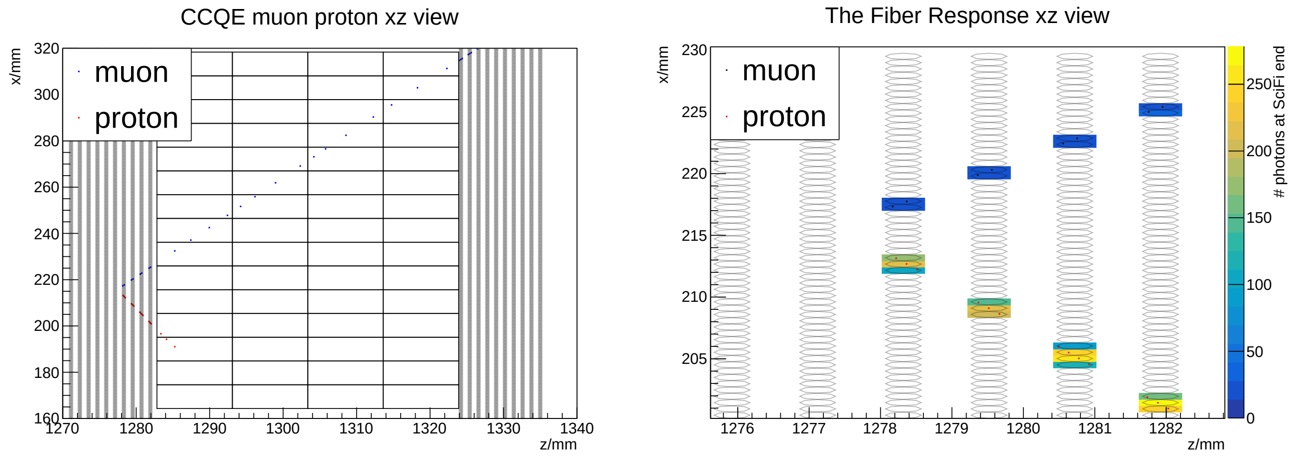
CCQE muon proton xz view

The Fiber Response xz view

(a) xz view truth track

(b) xz view SciFi response

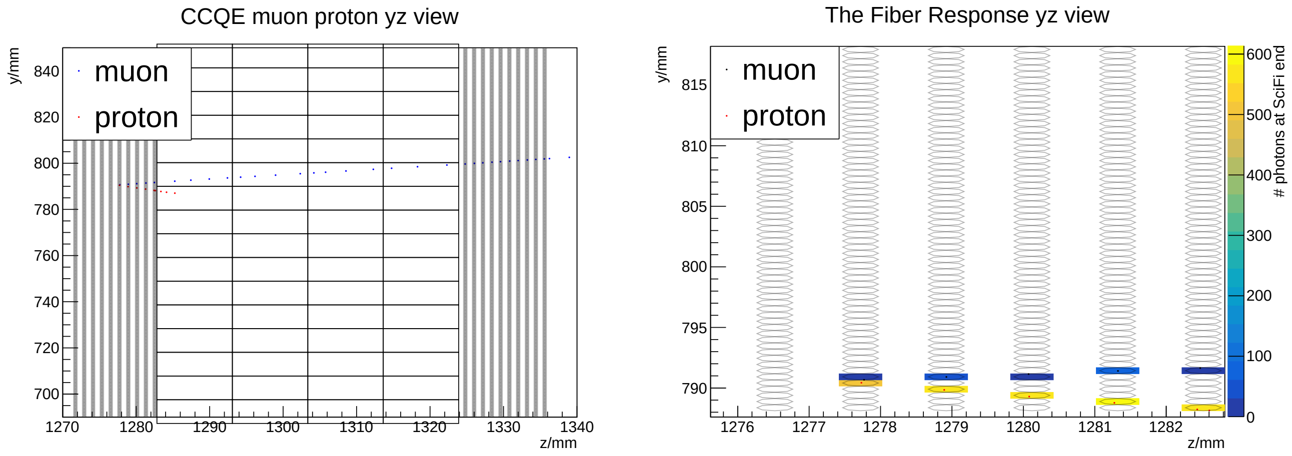
CCQE muon proton yz view

The Fiber Response yz view

(c) yz view truth track

(d) yz view SciFi response

Figure 8: A CCQE event display of the hybrid design

For the pure SciFi design, a ν_μ-Carbon CCQE event display of both nominal 6% PDE and improved 25% PDE configurations is shown in Figure 9. The ν_μ-Carbon interaction vertex is placed at the center of the pure SciFi detector. The color scales account for the number of detectable photons (photoelectrons (p.e.)) of each SciFi hit after simulating SPAD PDE. In Figure 9, it can be clearly seen that a stopping proton track with relatively high light yields and a visible Bragg Peak[2] at its tail. However, the muon escapes out of the visible scope of the plot with much lower

---

[2] The Bragg Peak is a pronounced peak on the Bragg curve which plots the energy loss of ionizing radiation during

light yields. Comparing to the improved 25% PDE configuration in Figure 9c and 9d, a nominal 6% PDE configuration in Figure 9a and 9b presents a significant sparsity of detectable hits from the muon's (minimum ionizing particle (MIP)) track. And the number of photoelectrons from proton's Bragg-Peak hit can be 5 to 10 times of that from muon's. So the current SPAD photosensor is already applicable for tracking stopping protons. Nevertheless, the current SPAD PDE has to be improved for a more precise MIP tracking and a better deposited energy resolution.

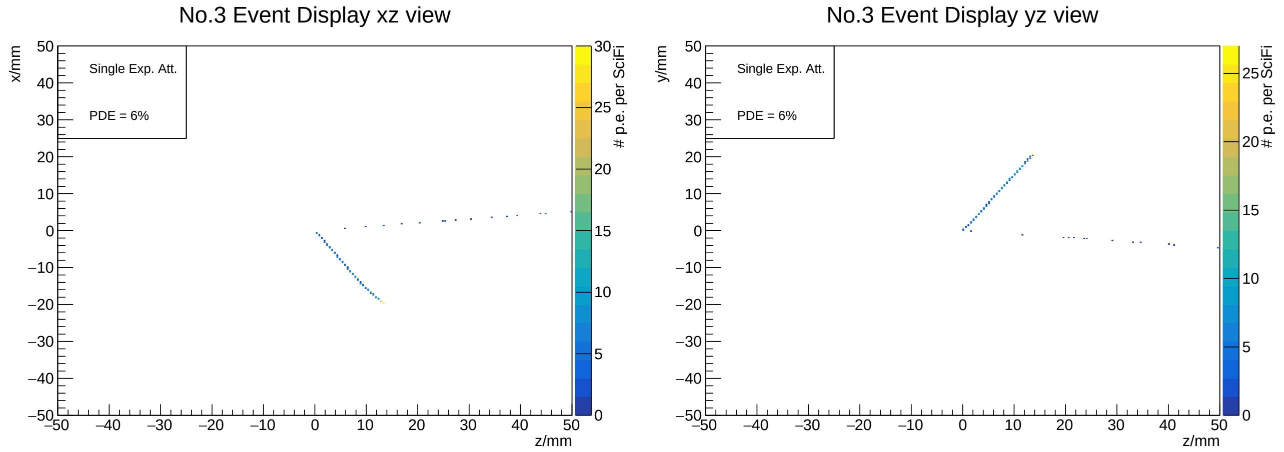

(a) xz view with PDE = 6%

(b) yz view with PDE = 6%

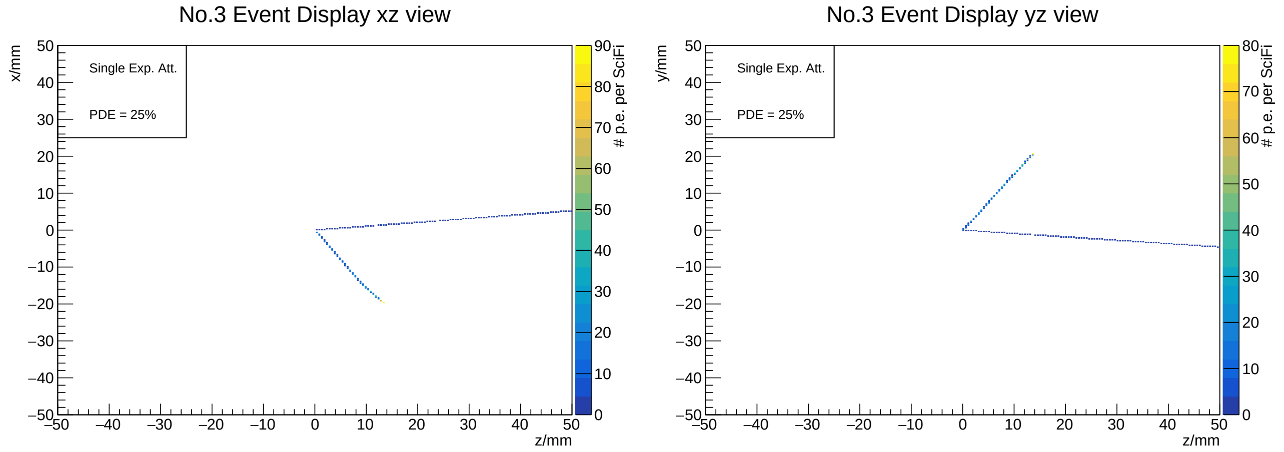

(c) xz view with PDE = 25%

(d) yz view with PDE = 25%

Figure 9: A CCQE Event Display of Pure SciFi Design with PDE = 6% or 25%

3.8 Summary of Applications of Two Designs to Different Physics Studies

After implementations of simulations and detector response algorithms, with Monte Carlo data on hand, the following three sections 4, 5, and 6 are dedicated to CC0πNp event reconstruction study, momentum reconstruction and charge identification by curvature, and $\gamma/e^{\pm}$ separation study, respectively.

In **section 4: CC0πNp Event Reconstruction Efficiency Study**, the pure scintillating fiber design is applied to estimate the highest reconstruction efficiency which can be achieved with the state-

---

its travel through matter. For protons, α-rays, and other ion rays, the peak occurs immediately before the particles come to rest [27].

of-the-art 0.25-mm granularity. The especial attention is paid to the reconstructable threshold of protons whose momenta are below 200 MeV/c.

In **section 5: Momentum Reconstruction and Charge Identification by Curvature**, the SciFi components of the hybrid design are utilized for reconstructions. It is a thorough examination about plausibility of reconstructing momenta and charge signs by curvature in a segmented dense-material detector with sub-mm spatial resolutions.

In **section 6: $\gamma/e^{\pm}$ Separation Study**, the pure scintillating fiber design is practiced to distinguish very collinear e^+e^- pairs from $\gamma \to e^+e^-$ pair productions. A high e^+e^- separation efficiency is expected with the help of 0.25-mm granularity.

4 CC0πNp Event Reconstruction Efficiency Study

CC0πNp is short for Charged-Current 0 pion N proton(s) event. The estimation of reconstruction efficiencies of CC0πNp event from ν_μ-Carbon interactions in the pure SciFi design is conducted in this section 4. The reaction can be compactly expressed as

$$\nu_\mu + n + (N-1)\, p \to \mu^- + Np\,,\, N \geq 1\,. \tag{40}$$

And the final states of a CC0πNp event are N protons and one muon. Estimating CC0πNp event reconstruction efficiencies of the novel HFGD is of great importance due to the fact that:

1. CC0π1p event has the greatest correlation to the CCQE process, of which the most accurate measurement of the incident neutrino energy is made.
2. If some of low-momentum final-state protons of a CC0πNp ($N \geq 2$) event are missed by the detector, then this event will contaminate the CC0$\pi N'$p ($N' < N$) sample. Thus the neutrino energy of this event will be lowlier estimated and contribute to the systematic uncertainty of the measurement. If these types of error are not properly modelled, they can even lead to the wrong measurement of oscillation parameters.

Therefore, if an unprecedented high CC0πNp event reconstruction efficiency of the novel HFGD is obtained, then we will have enough motivations to realize the design.

The final states of CC0πNp only have two categories of particles, namely muon and proton. Comparing to long penetrative muon tracks, most of proton tracks are short and compact to interaction vertices. So the key of CC0πNp reconstructions is the proton track reconstruction. An estimation of proton track reconstruction efficiency is presented in subsection 4.1.

To estimate CC0πNp reconstruction efficiencies, 100,000 CCQE events are simulated, with the T2K energy-spectrum ν_μ beam shooting along the z axis defined in Figure 7. All primary vertices of ν_μ-Carbon interactions are placed at the center of the pure SciFi design for an optimistic estimation. An estimation of exclusive CC0πNp reconstruction efficiencies is shown in subsection4.2.

In order to identify final-state protons and muons, detector responses to charged particles' energy loss in the pure SciFi design is explored in subsection 4.3.

Finally, a simple muon/proton separation algorithm based on the information of energy loss and track length is developed. The separation method and qualities based on reconstructable CC0πNp events are discussed in subsection 4.4.

4.1 Proton Track Reconstruction Efficiency Estimation

A criterion for judging whether a proton track is reconstructable or not in the pure SciFi design is proposed and decomposed into two parts:

1. Enough hits: A proton track contains at least 2 detectable hits in one view and at least 3 detectable hits in another view.

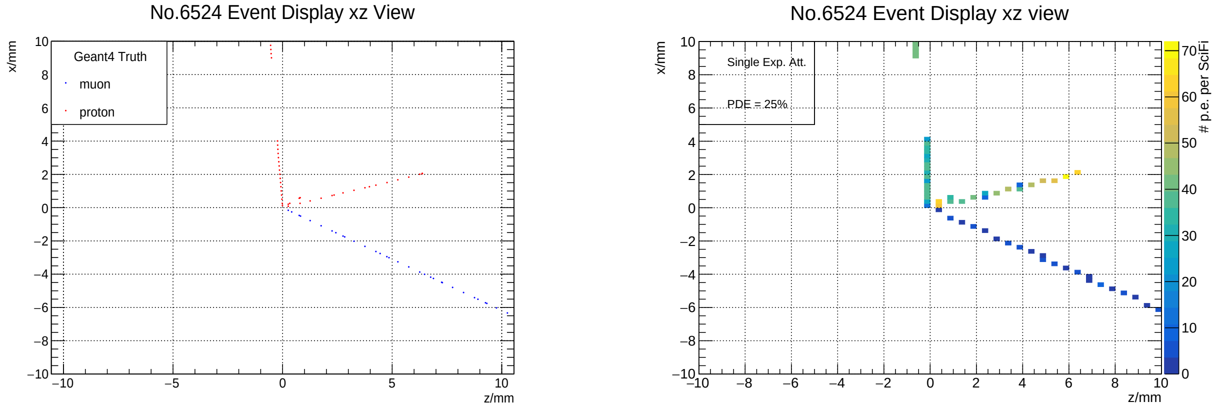

(a) Geant4 Truth xz view

(b) Detector Response xz view with PDE = 25%

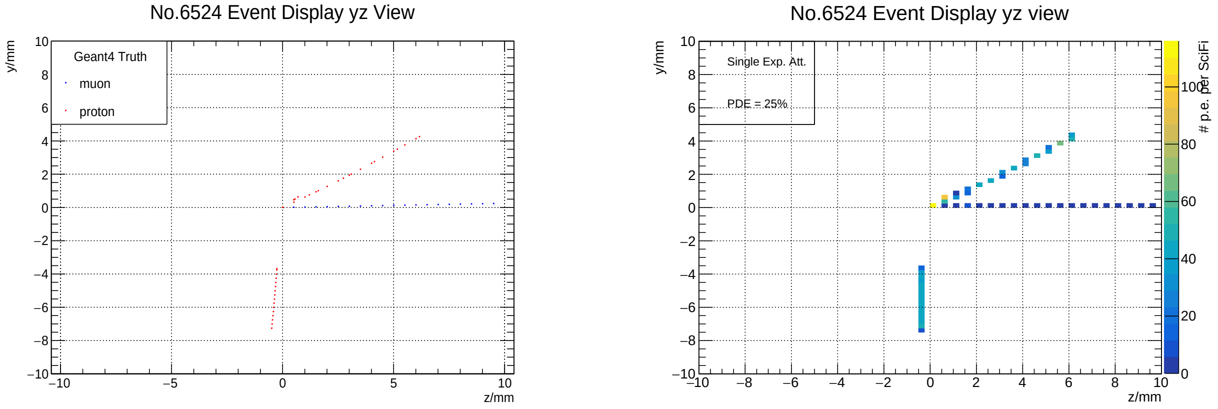

(c) Geant4 Truth yz view

(d) Detector Response yz view with PDE = 25%

Figure 10: A CC0π3p event display. According to the separability criterion, the shortest forward proton track is inseparable from another long forward proton track in both xz and yz views because there are no hit-free scintillating fibers in between at its ending slices. Hence the shortest proton track is tagged as inseparable and cannot be reconstructed although it has enough hits. In experiments, this true CC0π3p event is very likely to be wrongly reconstructed as a CC0π2p event.
P. S. Blanks of the backward proton track show up for both xz view and yz view, due to the fact that the polar angle of this proton track is so close to $\frac{\pi}{2}$ that it travels several millimeters inside the same SciFi slice.

Mathematically, $\max\{\#\text{ xz hits}, \#\text{ yz hits}\} \geq 3$ and $\min\{\#\text{ xz hits}, \#\text{ yz hits}\} \geq 2$.

2. Separability: For a proton track from a CC0πNp event, two ending hits from both xz view and yz view are checked. As long as one of the two ends stays away from any other tracks' hits by at least one hit-free SciFi at the same slice, this proton track is tagged as separable.

   As an example for a better comprehension of the separability, a true CC0π3p event with an inseparable forward short proton track is shown in Figure 10.

If a proton track can satisfy both enough hits and separability conditions, the proton track is regarded as a reconstructable one.

After implementing the reconstructable criterion to all proton tracks of 100,000 CCQE events sample, the proton track reconstruction efficiency of pure SciFi design can be visualised in Figure 11 and Figure 12. From Figure 11, we can see that even going down to a 150 MeV/c low-momentum domain, the pure SciFi design still keeps a decent 60% or so proton track reconstruction efficiency. The origin of inefficiency below 150 MeV/c (the corresponding proton kinetic energy is below 12

MeV) is that the proton track is too short (sub-mm) to generate enough detectable hits. Comparing the red proton momentum profile, which is the proton initial momentum distribution from NEUT CCQE ν_μ-Carbon interaction generator using the special function method, and the blue proton track reconstruction efficiency, it is clear that a nearly 100% efficiency is achieved for the most probable momenta region. Therefore, it is natural to see an over 97% high net proton reconstruction efficiency.

Besides, thanks to the highly ionizing nature of proton, when comparing proton reconstruction efficiencies from two PDE configurations in Figure 11a and Figure 11b, only a very tiny difference between the two shows up at high momentum region over 1,000 MeV/c. The tiny drop of the efficiency presented in Figure 11a at high momentum region is because the low PDE configuration cannot detect enough hits for high-momentum proton tracks with low dE/dx and short track lengths. And the short track length of the high-momentum proton is mainly due to the inelastic scattering (including proton absorptions) between proton and carbon nucleus, of which the total inelastic cross section is above 0.2 barn[3] at 1000 MeV/c [28, 29, 30].

Figure 12 shows the proton track reconstruction efficiency in a 2D phase space of proton initial momentum $|\vec{p}_{\text{proton,init}}|$ and proton polar angle $\cos(\theta)$ between its initial direction of motion and z axis. Except the observed inefficiency below 150 MeV/c from Figure 11, an inefficiency extending to the 250 MeV/c momentum region also takes place when the proton initial direction almost lies inside xy plane, i.e. $\theta \approx \frac{\pi}{2}$ or $\cos(\theta) \approx 0$. In this situation, the proton track is very likely to propagate in only one SciFi slice. Hence it cannot generate enough detectable hits for both xz view and yz view. Fortunately, from Figure 13, it is evident that only few protons are distributed in this inefficient domain. And it is also natural to visualize that most protons are travelling forward, since the incident neutrinos bombard the detector along the positive direction of z axis.

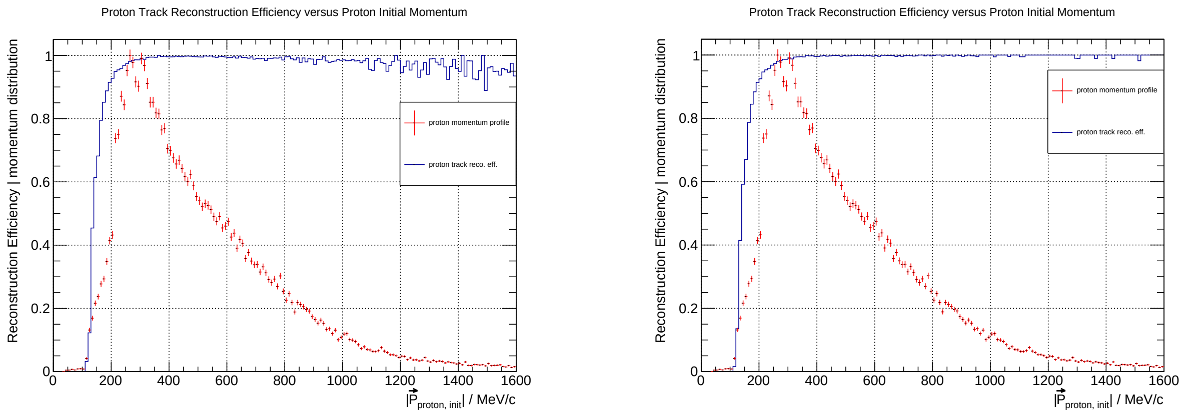

(a) PDE = 6%, Net Efficiency = 97.31%

(b) PDE = 25%, Net Efficiency = 97.72%

Figure 11: Proton Track Reconstruction Efficiency versus Proton Initial Momentum.

---

[3] $1\,\text{barn} = 10^{-28}\,\text{m}^2$

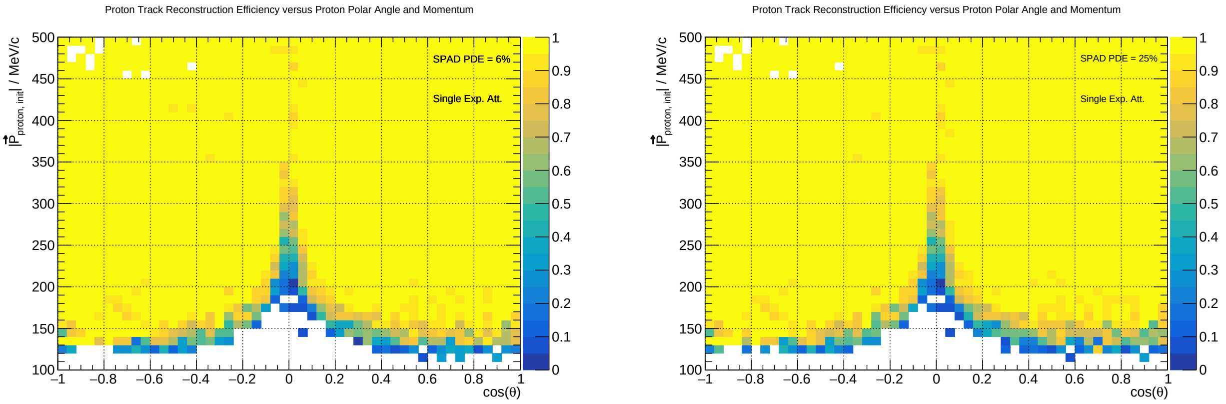

(a) θ is the polar angle between proton initial direction and z axis, PDE = 6%

(b) θ is the polar angle between proton initial direction and z axis, PDE = 25%

Figure 12: Proton Track Reconstruction Efficiency versus Proton Initial Momentum and Polar Angle

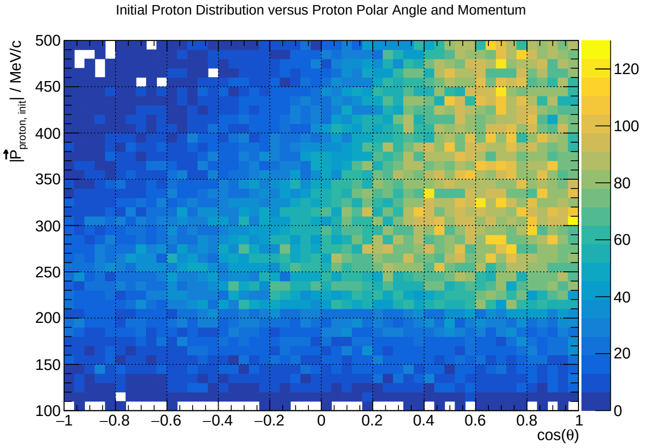

Figure 13: Initial Proton Distribution versus Proton Polar Angle and Momentum

4.2 Whole Event Reconstruction Efficiency Study

After the study of proton track reconstruction efficiency in subsection 4.1, it is straightforward to study the whole CC0πNp event reconstruction efficiency. From the reaction formula (40), if we impose that the final states are one muon and N protons at Geant4 truth levels, then an exclusive event reconstruction efficiency can be obtained via a set of similar criterion to the proton track reconstruction:

1. Enough hits: Every track from a true CC0πNp event consists at least 2 detectable hits in one view and at least 3 detectable hits in another view.

   Mathematically, $\max\{\#\text{ xz hits}, \#\text{ yz hits}\} \geq 3$ and $\min\{\#\text{ xz hits}, \#\text{ yz hits}\} \geq 2$.

2. Separability: For a true CC0πNp event, all proton tracks are separable according to the separability criterion explained in subsection 4.1. Because except all protons there is only one muon left from the event, all proton tracks' separability automatically grants the separability with the muon track.

If a true CC0πNp event fulfills all the criterion above, then it is regarded as a reconstructable event. After applying the criterion to the Geant4 truth CC0πNp event sample selected from the original $100,000$ CCQE events, the event reconstruction efficiencies corresponding to two different SPAD PDE configurations are listed in Table 4 and Table 5, respectively.

N of CC0πNp	the Number of Events	the Number of Reconstructable Events	Efficiency
1	76,940	74,960	97.43%
2	16,000	14,631	91.44%
3	4,154	3,572	85.99%
4	1,146	915	79.84%

Table 4: CC0πNp Event Reconstruction Efficiency with 6% PDE

N of CC0πNp	the Number of Events	the Number of Reconstructable Events	Efficiency
1	76,940	76,156	98.98%
2	16,000	14,848	92.80%
3	4,154	3,601	86.69%
4	1,146	917	80.02%

Table 5: CC0πNp Event Reconstruction Efficiency with 25% PDE

4.3 Charged Particles Energy Loss Study

The energy loss per unit path (dE/dx) is determined by the nature (mass, charge, category, etc.) of different particles. Hence it is widely applied in particle identification (PID). In experiment, the HFGD functions dually as a tracker and a calorimeter. Thus it is of great interests to study its sensitivity to different charged particles' dE/dx.

The detector response to dE/dx of pure SciFi design with 25% PDE configuration for most commonly detected electrons, muons, charged pions and protons are plotted in Figure 14. The stopping particles are selected by checking that they do not produce hits in boundary volumes of the detector. Figure 14a shows that the dE/dx for the electron whose energy is below 500 MeV is relatively flat. And electron does not have Bragg Peak (see footnote 2) at its track tail. Figure 14b and Figure 14c share quite similar patterns. Since muon and charged pion carry the same amount of electric charge and have very close rest mass values, both of them are equipped with medium-size Bragg Peaks. Proton is the heaviest particle among these four and possesses the highest Bragg Peak, which can be clearly seen in Figure 14d.

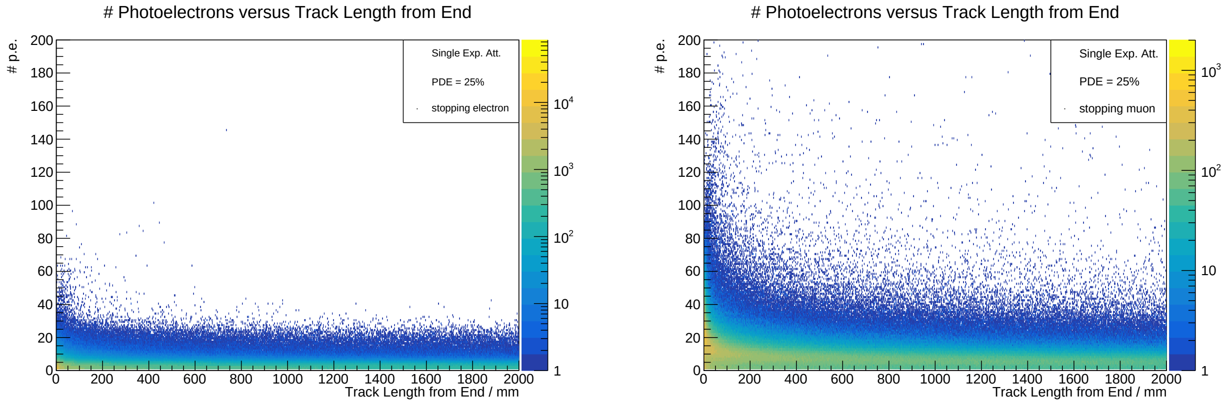

(a) Stopping Electron

(b) Stopping Muon

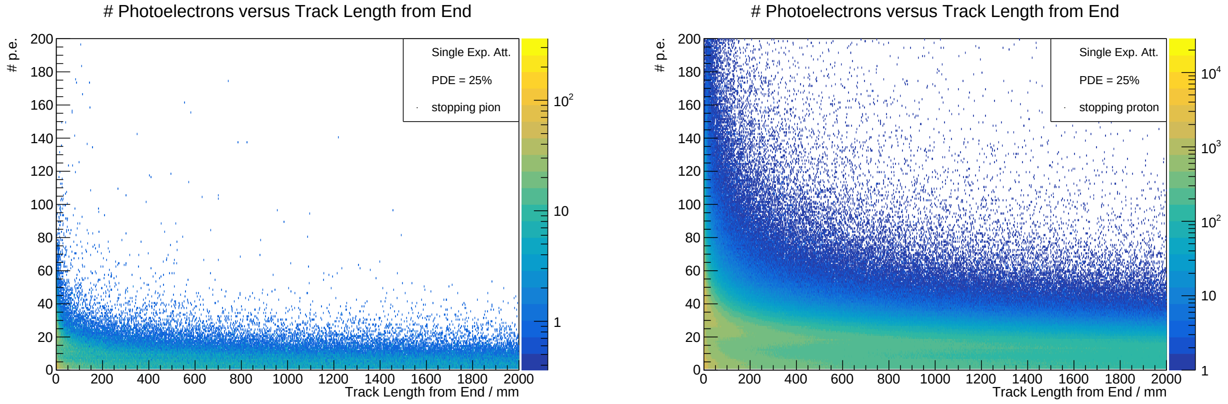

(c) Stopping Charged Pion

(d) Stopping Proton

Figure 14: Stopping Charged Particles Distribution versus the Number of Photoelectrons Per SciFi Hit and Track Residual Range

Comparing Figure 14b and Figure 14d, one can conclude that the difference of Bragg Peaks from proton and muon can be applied to distinguish one from another. Therefore, an observable which is the summation of the number of photoelectrons from the last 5 SciFi hits (Bragg Peak region) of a stopping charged particle is proposed to separate muon and proton. From Figure 15, it is clear that the single peak of stopping muon is from its Bragg Peak. Whilst stopping proton's double peaks originate from its inelastic-scattered stopping and Bragg Peak, from left to right, respectively. It is worthy to point out that after inelastic scattering, Geant4 treats the original track as a stopping one and all secondary products are new tracks with new IDs. Since the proton's Bragg Peak is higher

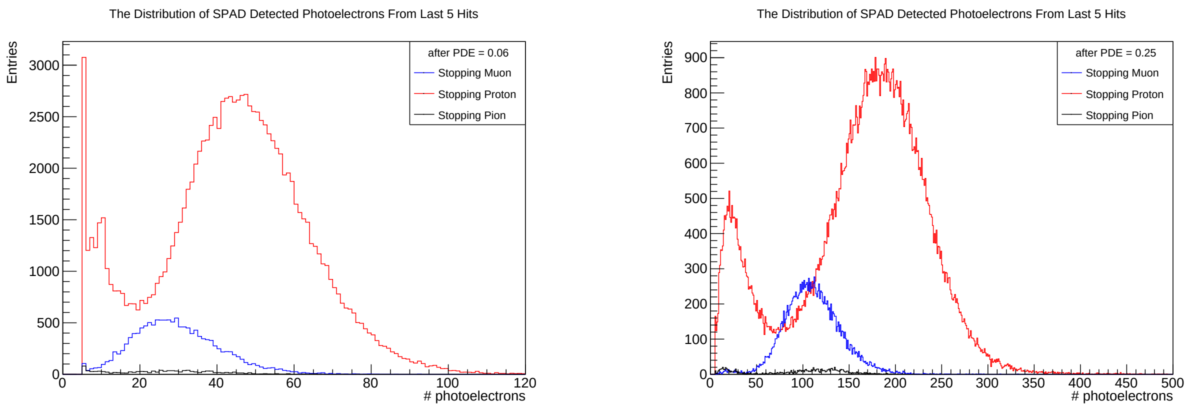

(a) PDE = 6%

(b) PDE = 25%

Figure 15: Distribution of the Summation of photoelectrons from Last 5 Hits

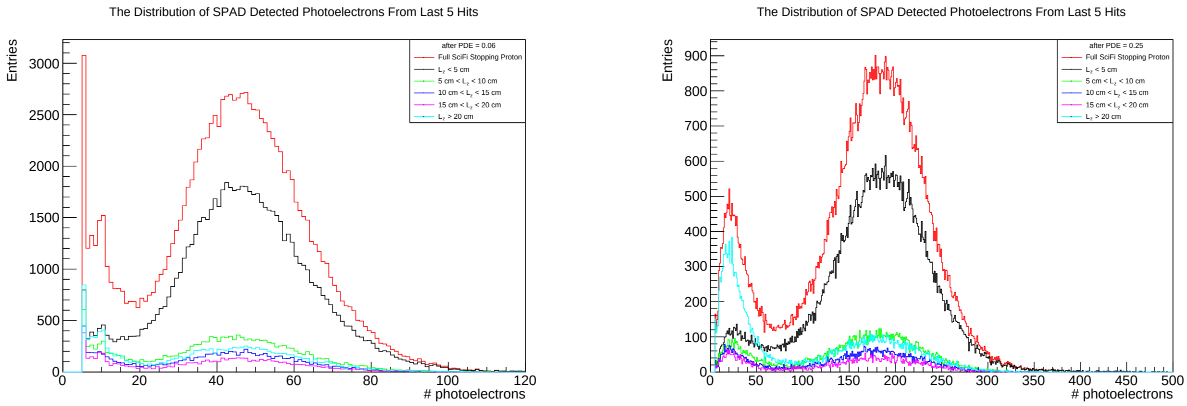

(a) PDE = 6%

(b) PDE = 25%

Figure 16: The Hint of Inelastic Scattering Proton Contribution

than that of muon's, the peak of muon in Figure 15 is centered to the left of the second peak of proton, just as expected.

A demonstration of inelastic scattering contribution to Figure 15 is plotted in Figure 16. Stopping protons are decomposed with respect to their track length along z axis (i.e. L_z). With the increase of L_z, the ratio of the height of the first peak to that of the second peak becomes larger and larger. At the same time, the proton's energy, the number of nuclei that it encounters along the path, and the inelastic scattering cross section are also generically greater. Hence the probability of proton-nucleus inelastic scattering also monotonically increases. Therefore, Figure 16 implies that the appearance of the left proton peak is due to proton-nucleus inelastic scatterings.

4.4 Particle Identification Study

Apart from the summation of photoelectrons from last 5 SciFi hits, the track length of stopping particles can further lift the degeneracy for a better PID quality. The track length of a track is calculated by accumulating the distance between two detectable consecutive hits. The distributions of stopping protons, stopping muons and stopping pions in the 2D phase space of the summation of photoelectrons from last 5 SciFi hits and track length are shown in Figure 17. Since the charged pions' distribution are completely overlapped with either protons' or muons', this PID prescription is unable to separate pion. However, by the virtues that the reconstructable CC$0\pi N$p events are from true CC$0\pi N$p samples, a preliminary PID can be applied for muon/proton separation. The PID purity and efficiency as PID quality measures are defined as follows

$$\text{PID Purity} = \frac{\text{the number of true particles } X \text{ which are also identified as } X}{\text{the total number of particles which are identified as } X}, \tag{41}$$

$$\text{PID Efficiency} = \frac{\text{the number of correctly identified particles } X}{\text{the total number of true particles } X}. \tag{42}$$

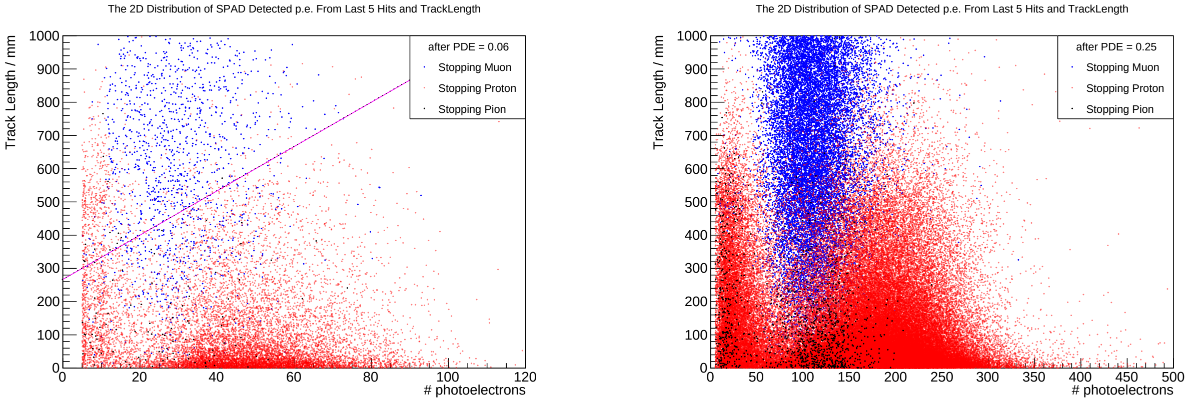

(a) PDE = 6%

(b) PDE = 25%

Figure 17: The Distribution of Stopping Proton, Muon and Pion versus the Summation of photoelectrons from Last 5 Hits and Track Length

As a preliminary application, a straight purple line is drawn in Figure 17a for a simple muon/proton separation. Then the final states of our reconstructable CC$0\pi N$p events can be identified as muons (above the purple line) or protons (beneath the purple line). The PID qualities of this simple method are listed in Table 6, Table 7, Table 8 and Table 9 for CC$0\pi N$p with $N = 1, 2, 3, 4$, respectively. An over 90% PID efficiency and purity can be achieved for muon/proton separation. The main PID failure is from high-energy inelastic-scattered protons and low-energy short muons. And this can be cured by a more complicated non-linear separation along the envelop of muons' distribution in Figure 17, for example.

True PID	True muon	True proton	PID sum	PID Purity
PID as muon	65,896	4,988	70,884	92.96%
PID as proton	7,765	68,673	76,438	89.84%
True Sum	73,661	73,661		
PID Efficiency	89.46%	93.23%		

Table 6: CC0π1p

True PID	True muon	True proton	PID sum	PID Purity
PID as muon	12,802	835	13,637	93.88%
PID as proton	1,583	27,935	29,518	94.64%
True Sum	14,385	28,770		
PID Efficiency	89.00%	97.10%		

Table 7: CC0π2p

True PID	True muon	True proton	PID sum	PID Purity
PID as muon	3,121	184	3,305	94.43%
PID as proton	410	10,409	10,819	96.21%
True Sum	3,531	10,593		
PID Efficiency	88.39%	98.26%		

Table 8: CC0π3p

True PID	True muon	True proton	PID sum	PID Purity
PID as muon	801	55	856	93.57%
PID as proton	100	3,549	3,649	97.26%
True Sum	901	3,604		
PID Efficiency	88.90%	98.47%		

Table 9: CC0π4p

5 Momentum Reconstruction and Charge Identification by Curvature

If a charged particle is only subjected to a uniform magnetic field $\vec{B}$, its trajectory forms a helix. The 3D helix motion can be decomposed into a constant velocity 1D motion along the direction of $\vec{B}$ and a uniform 2D circular motion in the plane orthogonal to $\vec{B}$. From the Lorentz force formula, its equation of motion is as follows,

$$\frac{d\vec{p}}{dt} = ze\vec{v} \times \vec{B} \,, \tag{43}$$

where $\vec{p} = \frac{m_0 \vec{v}}{\sqrt{1-v^2/c^2}}$ is its spatial momentum, z is its electric charge in unit of the elementary charge, $\vec{v}$ is its velocity and e is the magnitude of the elementary charge. Due to a virtue of the Lorentz force which is always perpendicular to $\vec{p}$ and hence it does not change $|\vec{p}|$, Eq.(43) is often applied to measure the momentum of charged particles. The gyroradius R or the equivalent curvature $k \equiv \frac{1}{R}$ of the 2D circular motion derived from Eq.(43) is

$$R \equiv \frac{1}{k} = \frac{|\vec{p}_\perp|}{zeB} \,, \tag{44}$$

where $\vec{p}_\perp$ is the momentum component perpendicular to $\vec{B}$. A more practical form with proper units conversion of Eq.(44) is, to a very good approximation,

$$|\vec{p}_\perp|(\mathrm{GeV}) = 0.3 \cdot z \cdot B(\mathrm{T}) \cdot R(\mathrm{m}) \equiv \frac{0.3 \cdot z \cdot B(\mathrm{T})}{k\left(\mathrm{m}^{-1}\right)} \,. \tag{45}$$

In principle, the momentum component parallel to $\vec{B}$ can be measured as well

$$|\vec{p}_\parallel| = zeB\frac{|\Delta\vec{x}_\parallel|}{\Delta\theta} \approx 0.3 \cdot z \cdot B(\mathrm{T}) \cdot \frac{|\Delta\vec{x}_\parallel|(\mathrm{m})}{\Delta\theta(\mathrm{rad})} \,, \tag{46}$$

where $|\Delta\vec{x}_\parallel|$ is the magnitude of the charged particle's displacement projected to $\vec{B}$ direction, and $\Delta\theta$ is the corresponding circular rotational angle in the plane perpendicular to $\vec{B}$.

The charge identification (CID) by curvature is based on Eq.(43). The particle carrying the opposite sign of the electric charge is bent to the opposite direction in the plane perpendicular to $\vec{B}$. Then by testing the bending direction of the track, the sign of the charge can be identified.

In experiments, comparing to protons, α-particles or other heavier nuclei, muons and charged pions have much smaller average dE/dx. Hence they are more likely to escape out of detectors rather than depositing all of their kinetic energies in detectors. To measure their momenta, an effective way is reconstructing curvatures of their partial trajectories in a uniformly magnetized tracker. Meanwhile, in plastic scintillators, incident electrons are subjected to bremsstrahlung and intense Møller scatterings with atomic electrons, which make their passages fairly zig-zag and improper for curvature reconstruction.

Overall, in following subsections, muons μ^- and charged pions π^- are investigated in 0.50-mm-diameter SciFi components of the hybrid design to examine the error and efficiency of momentum reconstruction and CID by curvature, respectively. A nominal field strength $B = 0.2$ T and a enhanced one $B = 0.5$ T are adopted to study improvements of reconstruction qualities by increasing magnetic fields. At first, the momentum error and CID efficiency is estimated by parameterized formulas presented in subsection 5.1. After that, Geant4 simulations of passages of μ^- and π^- in the hybrid design and consistency check between simulations and parameterized formulas are explained in subsection 5.2. At last, results of momentum reconstructions (CID) by curvature based on simulation data, and comparison between momentum resolutions $\frac{\sigma_{p_\perp}}{p_\perp}$ (CID efficiencies) derived from reconstruction algorithms and parameterized formulas are shown in subsection 5.3 (subsection 5.4), respectively.

5.1 Momentum Error/Charge Identification Efficiency from Parameterized Formula

Main references of subsection 5.1 are **Sec.34.3 Multiple scattering through small angles** (pp. 554-555) and **Sec.35.13 Measurement of particle momenta in a uniform magnetic field** (pp. 610-611) of *The Review of Particle Physics (2022)* [1].

The measurement error (resolution) of particle momenta by curvature in a uniform magnetic field can be estimated by parameterized formulas. The distribution of measurements of the curvature $k \equiv 1/R$ is approximately Gaussian, with the standard deviation σ_k contributed from both multiple scatterings $(\sigma_k)_{\mathrm{MS}}$ and finite spatial resolutions $(\sigma_k)_{\mathrm{SpaRes}}$ of the tracker [1]

$$\sigma_k = \sqrt{{(\sigma_k)_{\mathrm{MS}}}^2 + {(\sigma_k)_{\mathrm{SpaRes}}}^2}\,. \tag{47}$$

Then the resolution of the projected particle momentum $p_\perp$ measurement constrained by both multiple scatterings and finite spatial resolution can be estimated by the following parameterized formula

$$\frac{\sigma_{p_\perp}}{p_\perp} \approx \frac{\sigma_R}{R} = \frac{\sigma_k}{k} \equiv R \cdot \sigma_k \approx \frac{|\vec{p}_\perp|(\mathrm{GeV})}{0.3 \cdot z \cdot B(\mathrm{T})} \cdot \sigma_k(\mathrm{m}^{-1})\,, \tag{48}$$

where the last approximation in Eq.(48) above is made by inserting Eq.(45) to substitute R.

For the CID by bending directions of tracks in a uniform magnetic field, a CID efficiency can be defined as follows

$$\text{CID Eff.} \equiv \frac{\text{the number of correct CID particles}}{\text{the number of total particles performed CID}}\,. \tag{49}$$

If the distortion of bending directions is predominately from multiple scatterings, a parameterized formula for CID efficiency can be constructed as well (see Eq.(61)).

The multiple scattering contribution to the angular resolution θ_0, momentum reconstruction error $\frac{(\sigma_{p_\perp})_{\mathrm{MS}}}{p_\perp}$ and CID efficiency is introduced in sub-subsection 5.1.1. The finite spatial resolution contribution to the momentum reconstruction error $\frac{(\sigma_{p_\perp})_{\mathrm{SpaRes}}}{p_\perp}$ and angular resolution $(\sigma_\theta)_{\mathrm{SpaRes}}$ is presented in sub-subsection 5.1.2. Finally, the net momentum reconstruction error $\frac{\sigma_{p_\perp}}{p_\perp}$ and net angular resolution $\Delta\theta_{\mathrm{rms}}$ are assembled in sub-subsection 5.1.3.

5.1.1 Small-Angle Multiple Scattering Contribution

A charged particle (e.g. $\mu^{\pm}$ or $\pi^{\pm}$) passes through matter will experience a series of scatterings with the matter. Most of them are Coulomb scatterings described by Rutherford's formula. For hadrons like pions, the strong interactions also contribute to multiple scatterings. If all multiple scatterings are small-angle ones, the accumulated distribution of net deflection angles and displacement should be Gaussian like via the central limit theorem. The non-Gaussian long tails are contributed by less frequent "hard" large-angle deflections [1].

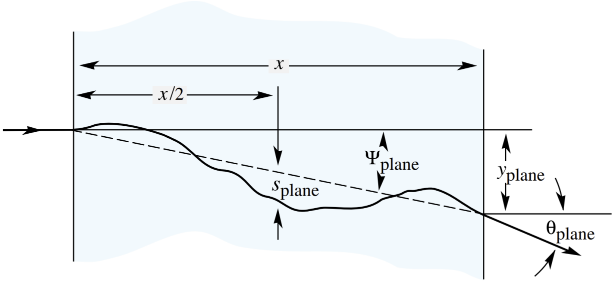

Figure 18: Quantities used to describe multiple Coulomb scattering. The particle is incident in the plane of the figure [1]

.

The quantities used to describe multiple Coulomb scattering are shown in Figure 18 [1]. If we define

$$\theta_0 \equiv \theta^{\text{rms}}_{\text{plane}} = \frac{\theta^{\text{rms}}_{\text{space}}}{\sqrt{2}} \tag{50}$$

to be the standard deviation of the Gaussian approximation of the net deflection angle distribution, then its empirical parameterized formula is given by G. R. Lynch and O. I. Dahl [31] as follows

$$\theta_0 = \frac{13.6\text{MeV/c}}{\beta p} z \sqrt{\frac{x}{X_0}} \left[1 + 0.038 \ln\left(\frac{x z^2}{X_0 \beta^2} \right) \right] , \tag{51}$$

where β, p and z are the speed, momentum magnitude and electric charge number of the incident particle. (x/X_0) is the longitudinal track length in unit of material's radiation length. The random variables sagitta s (the depth or height of an arc), ψ, y and θ in the plane are correlated, e.g. $y \approx x \cdot \psi$. Two useful relations of the standard deviation of the sagitta and y_{plane} displacement induced by multiple scatterings inside the plane are listed in Eq.(52) and Eq.(53).

$$s^{\text{rms}}_{\text{plane}} = \frac{1}{4\sqrt{3}} x \theta^{\text{rms}}_{\text{plane}} = \frac{1}{4\sqrt{3}} x \theta_0 \tag{52}$$

$$y^{\text{rms}}_{\text{plane}} = \frac{1}{\sqrt{3}} x \theta^{\text{rms}}_{\text{plane}} = \frac{1}{\sqrt{3}} x \theta_0 \tag{53}$$

Then the probability density function (PDF) of the projected y_{plane} after small-angle multiple

Coulomb scatterings is approximately given by a Gaussian distribution [1]

$$\mathrm{PDF}\left(y_{\mathrm{plane}}\right) = \frac{1}{y_{\mathrm{plane}}^{\mathrm{rms}}\sqrt{2\pi}}\,\exp\left(-\frac{y_{\mathrm{plane}}^{2}}{2\left(y_{\mathrm{plane}}^{\mathrm{rms}}\right)^{2}}\right). \tag{54}$$

And Eq.(54) above will be applied for deriving the parameterized CID efficiency formula (see Eq.(61)). Besides, a validation of Eq.(54) by Geant4 simulations is presented in sub-subsection 5.2.1.

From the definition of sagitta shown in Figure 19 [32], the sagitta s can be expressed as a function of the radius r and chord l of an arc

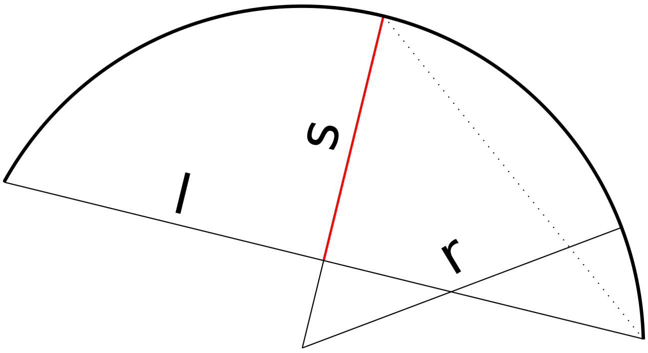

Figure 19: The definition of sagitta [32].

$$s = r - \sqrt{r^2 - \left(\frac{l}{2}\right)^2}\,. \tag{55}$$

If $\frac{l}{r} \ll 1$, then

$$s \approx \frac{l^2}{8}\,\frac{1}{r} \equiv \frac{l^2}{8}\,k\,, \tag{56}$$

where $k \equiv r^{-1}$ is the curvature of the arc. The variation of k from the variation of sagitta s is

$$\delta k \approx \frac{8}{l^2}\,\delta s\,. \tag{57}$$

Therefore, for a slightly curved track whose length L is approximately equal to the chord l of the arc fitting the track, the standard deviation $(\sigma_k)_{\mathrm{MS}}$ of the track curvature from small-angle multiple scatterings is pronounced as

$$(\sigma_k)_{\mathrm{MS}} \approx \frac{8}{L^2}\,s_{\mathrm{plane}}^{\mathrm{rms}}\,. \tag{58}$$

For a charged particle flying in a constant magnetic field $\vec{B}$, if following underlying assumptions are held,

1. the track bending from the Lorentz force is much larger than the deflection from multiple scatterings;
2. multiple scatterings are predominately Coulomb scatterings in the small-angle limit;

3. the energy loss of a charged particle in the medium is negligible;

4. the track length in unit of radiation length of the medium fulfills the condition $10^{-3} < \frac{L}{X_0} < 100$ [31],

then the resolution of projected particle momentum $p_\perp$ measurements constrained by multiple scatterings can be estimated by the following parameterized formula

$$\frac{(\sigma_{p_\perp})_{\mathrm{MS}}}{p_\perp} \approx \frac{(\sigma_R)_{\mathrm{MS}}}{R} = \frac{(\sigma_k)_{\mathrm{MS}}}{k} = \frac{8\,R\,s_{\mathrm{plane}}^{\mathrm{rms}}}{L^2}\,, \tag{59}$$

where Eq.(44) and Eq.(58) are applied and $k \equiv R^{-1}$ is the curvature of the track predominately shaped by the Lorentz force. Explicitly, for a unit charged $z = 1$ particle, inserting Eq.(44), Eq.(51) and Eq.(52) into Eq.(59) yields

$$\frac{(\sigma_{p_\perp})_{\mathrm{MS}}}{p_\perp} \approx 52.35 \times \frac{1 + 0.038 \ln\left(\frac{L}{X_0}\frac{1}{\beta^2}\right)}{B(\mathrm{T})\,\beta\,\sqrt{L(\mathrm{mm})\,X_0(\mathrm{mm})}}\,, \tag{60}$$

where $\frac{L}{X_0}$ is the longitudinal track length in unit of radiation length of the medium. The only medium relevant parameter in Eq.(60) is the radiation length X_0, which is used to characterise the intensity of multiple scatterings in the medium. If we neglect tiny contributions from the logarithm term on the numerator of Eq.(60), a simple calculation $\sqrt{\frac{X_0(\text{Polystyrene})}{X_0(\text{T2K TPC Mixture Gas})}} \approx 0.06$[4] shows that under same circumstances, the momentum resolution of gas-based TPC is roughly 0.06 times better than that of the polystyrene-based HFGD, if we only consider the multiple scattering contribution to the momentum resolution.

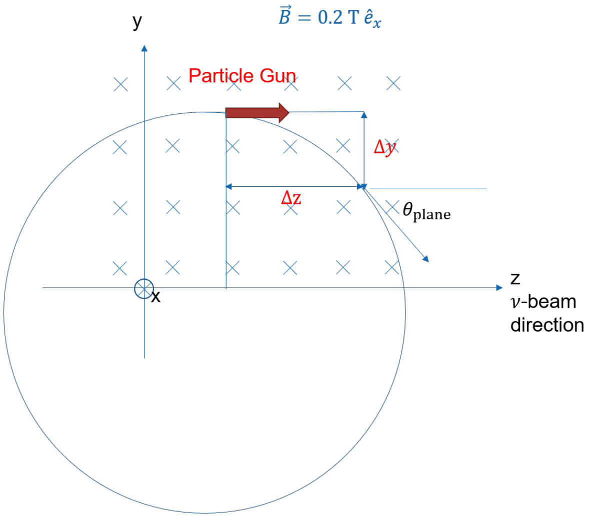

Figure 20: A sketch of a negatively charged particle doing circular motion in the yz plane. The magnetic field $\vec{B}$ is along the positive direction of x axis.

For CID by bending directions, a parameterized formula based on Eq.(54) for the CID efficiency defined in Eq.(49) can be formulated. As shown in Figure 20, if CID is studied by using a single

---

[4] X_0(Polystyrene) = 41.706 cm, X_0(T2K TPC Mixture Gas) = 117.575 m, data taken from the Geant4 implementation of ND280 Software[22]

direction particle gun shooting along z axis, then ideally, the sign of the displacement $\Delta y^{\text{Lorentz}} \equiv y^{\text{Lorentz}}_{\text{final}} - y_{\text{initial}}$ due to the Lorentz force should represent the sign of the electric charge. However, multiple scatterings can reverse the sign of Δy and lead to wrong CID. If the multiple scattering is the sole reason for displacing Δy other than Lorentz force and the y_{plane} distribution is indeed depicted by Eq.(54), then the CID efficiency can be approximated as an integral

$$\text{CID Eff.} \approx \int_0^{+\infty} \frac{d y_{\text{plane}}}{y^{\text{rms}}_{\text{plane}} \sqrt{2\pi}} \exp\left(- \frac{\left(y_{\text{plane}} - |\Delta y^{\text{Lorentz}}|\right)^2}{2\left(y^{\text{rms}}_{\text{plane}}\right)^2} \right) = 1 - \frac{1}{2} \operatorname{erfc}\left(\frac{|\Delta y^{\text{Lorentz}}|}{\sqrt{2} y^{\text{rms}}_{\text{plane}}} \right) , \tag{61}$$

where the complementary error function is defined as

$$\operatorname{erfc}(z) := 1 - \operatorname{erf}(z) \equiv 1 - \frac{2}{\sqrt{\pi}} \int_0^z dt\, e^{-t^2} , \tag{62}$$

and $\Delta y^{\text{Lorentz}} \equiv y^{\text{Lorentz}}_{\text{final}} - y_{\text{initial}}$ is the calculated y-direction displacement by assuming charged particles are only affected by the Lorentz force (i.e. no interactions at all with detector materials). The meaning of the CID efficiency parameterized formula Eq.(61) is that after small-angle multiple Coulomb scatterings with mediums, comparing to the situation that charged particles are only subjected to the Lorentz force, the probability that the sign of $\Delta y \equiv y_{\text{final}} - y_{\text{initial}}$ remains unchanged, i.e. the probability of $\left(\text{sign}\left(\Delta y\right) = \text{sign}\left(\Delta y^{\text{Lorentz}}\right)\right)$.

5.1.2 Spatial Resolution Contribution

If many (≥ 10) uniformly spaced position measurements are made along a trajectory in a uniform medium, then the spatial resolution contribution to the curvature error $(\sigma_k)_{\text{SpaRes}}$ can be expressed as [1]

$$(\sigma_k)_{\text{SpaRes}} = \frac{\epsilon}{L'^2} \sqrt{\frac{720}{N+4}} , \tag{63}$$

where

- N = the number of hits measured along track;
- L' = the projected length of the track onto the bending plane;
- ϵ = spatial resolution for each hit, perpendicular to the trajectory.

The advantage of the Eq.(63) is that the $(\sigma_k)_{\text{SpaRes}}$ can be estimated without feeding the data of specific hits position.

For arbitrary spacing of coordinates s_i measured along the projected trajectory with measurement errors ϵ_i, the curvature error $(\sigma_k)_{\text{SpaRes}}$ is calculated from [1]

$$(\sigma_k)_{\text{SpaRes}} = \frac{4}{w} \frac{V_{ss}}{V_{ss} V_{s^2 s^2} - \left(V_{ss^2}\right)^2} , \tag{64}$$

where V are covariances defined as $V_{s^m s^n} := \langle s^m s^n \rangle - \langle s^m \rangle \langle s^n \rangle$ with $\langle s^m \rangle = w^{-1} \sum_i \left(s_i^m / \epsilon_i^2 \right)$ and $w = \sum_i \epsilon_i^{-2}$. The application of Eq.(64) requires the input of hits position from track data, e.g. Geant4 simulation.

Overall, the spatial resolution contribution to momentum measurement error $\frac{(\sigma_{p_\perp})_{\text{SpaRes}}}{p_\perp}$ is approximated as follows

$$\frac{(\sigma_{p_\perp})_{\text{SpaRes}}}{p_\perp} \approx \frac{(\sigma_k)_{\text{SpaRes}}}{k} = R \cdot (\sigma_k)_{\text{SpaRes}} \,, \tag{65}$$

where $k \equiv R^{-1}$ is the curvature of the track predominately shaped by the Lorentz force.

Apart from the estimation of momentum resolution, the spatial resolution contribution $(\sigma_\theta)_{\text{SpaRes}}$ to the angular resolution $\Delta\theta_{\text{rms}}$ can also be studied

$$(\sigma_\theta)_{\text{SpaRes}} = \frac{\epsilon}{L\sqrt{6\pi}} \,, \tag{66}$$

where ϵ is the spatial resolution of each hit and L is the track length taken for measurement.

5.1.3 Net Momentum and Angular Resolution

After the discussion of both multiple scattering and spatial resolution contribution to the momentum and angular resolution of the detector, it is ready to explore the net momentum and angular resolution. Mathematically, the net momentum resolution $\frac{\sigma_{p_\perp}}{p_\perp}$ and angular resolution$(\sigma_\theta)_{\text{SpaRes}}$ are calculated as Eq.(67) and Eq.(68)

$$\frac{\sigma_{p_\perp}}{p_\perp} = \sqrt{\left[\frac{(\sigma_{p_\perp})_{\text{MS}}}{p_\perp}\right]^2 + \left[\frac{(\sigma_{p_\perp})_{\text{SpaRes}}}{p_\perp}\right]^2} \tag{67}$$

$$\Delta\theta_{\text{rms}} = \sqrt{\theta_0^2 + (\sigma_\theta)_{\text{SpaRes}}{}^2} \,, \tag{68}$$

where $\theta_0 = \theta_{\text{plane}}^{\text{rms}} \equiv (\sigma_\theta)_{\text{MS}}$ comes from Eq.(51).

We take the hybrid design of HFGD as an example to visualize its momentum resolution. Muon with 400 MeV/c initial momentum is the most suitable particle to explore. Because it is the minimum ionizing particle (MIP) in polystyrene and satisfies the underlying assumptions listed in sub-subsection 5.1.1 of the parameterized formula Eq.(59) best. Reasons are as follows,

1. Comparing to pions and protons, muons as leptons are not subjected to “hard" multiple scatterings contributed from strong interactions with nuclei, which more often cause large-angle deflections when comparing to “soft "Coulomb scatterings;
2. Muons are in MIP states and have the smallest energy loss per unit path in polystyrene;
3. Muons are roughly 200 times heavier than electrons. Comparing to the Møller scatterings of electrons, they are less likely to be deflected when scattered with atomic electrons. Meanwhile,

for the energy scale ~ 1 GeV, unlike electrons' energy losses dominated by bremsstrahlung with matters, muons' deflections due to radiative energy losses ($P_{\text{Radiation}} \propto \gamma^4 = \left(\frac{E}{m_0 c^2}\right)^4$) are negligible.

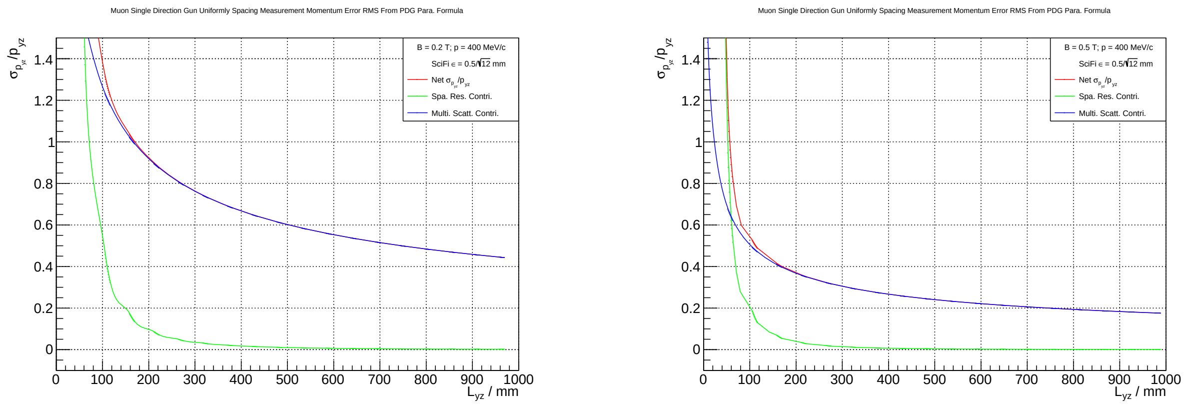

(a) B = 0.2 T

(b) B = 0.5 T

Figure 21: The resolution of momentum by curvature for 400 MeV/c muon in the hybrid design

The results are shown in Figure 21a and 21b with two uniform magnetic field configurations $\vec{B} = 0.2\,\mathrm{T}\,\hat{e}_x$ and $0.5\,\mathrm{T}\,\hat{e}_x$, respectively. Figure 21 clearly shows that after 200 mm travel, multiple scatterings' contribution dominates the momentum resolution. In reality, charged particles lose energy-momentum quite significantly in dense materials like polystyrene. Even the MIP muon will in average lose about half of its energy after 100 cm travel. Thus one also has to develop an effective energy loss correction method to compensate the measured down-shift momentum to its initial value. From the asymptotic scaling $\frac{\sigma_{pyz}}{p_{yz}} \propto \frac{1}{B\sqrt{L}}$ when $L > 200$ mm, increasing magnetic fields is an effective way to improve the momentum resolution. However, in a real experiment, the cost of magnets and maintaining strong magnetic field by large electric currents should also be considered.

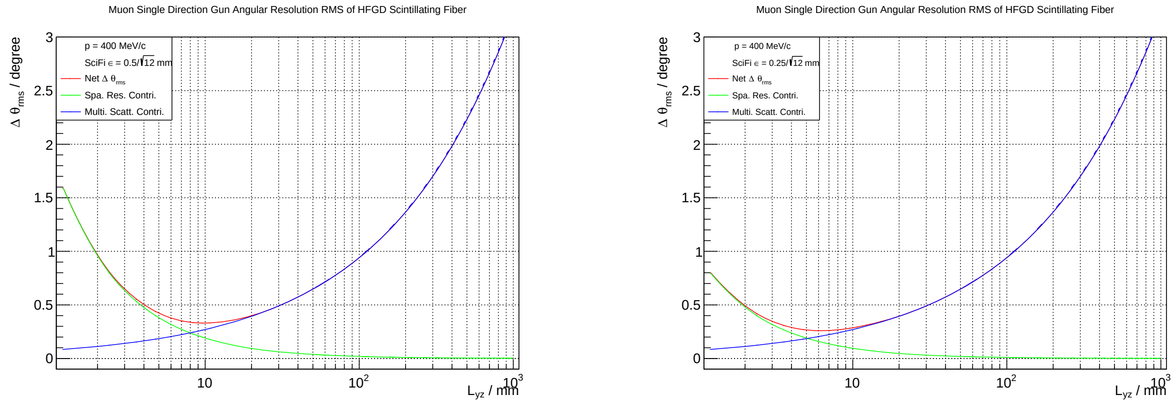

(a) SciFi hit spatial resolution $\epsilon = \frac{0.50}{\sqrt{12}}$ mm

(b) SciFi hit spatial resolution $\epsilon = \frac{0.25}{\sqrt{12}}$ mm

Figure 22: The angular resolution of 400 MeV/c muon

In Figure 22, the 400 MeV/c MIP muon is also used to characterise the angular resolution of 0.50 mm and 0.25 mm SciFi adopted by the hybrid and pure SciFi design, respectively. For such a muon, Figure 22a illustrates that the best angular resolution ~ 0.3° is achieved after travelling 10 mm for 0.50-mm-diameter SciFi, while Figure 22b for 0.25-mm-diameter SciFi tells that the best value appears at merely 6 mm away from the muon's vertex. Besides, Figure 22 also states that the angular resolution is determined by spatial resolution at the vicinity of vertex but dominated by multiple scattering after 20 mm travel.

5.2 Geant4 Simulation for Curvature Study

Samples for momentum reconstructions and charge identifications (CID) by curvature are simulated by the Geant4 software for the hybrid design of HFGD. Single-direction particle guns for muon μ^- and negatively charged pion π^- are used as particle sources. The particle guns are programmed to shoot along the z axis defined in Figure 6 and placed at the center of the first SciFi slice of the first duplicate module of the hybrid design to maximize the number of SciFi hits. Only 19 SciFi sections of each track are selected for momentum reconstruction and CID by curvature (visible from the 19 discrete concentrations of the distribution in Figure 26a).

The detector is magnetized by a uniform magnetic field along x axis. Hence the yz view is applied for $p_\perp \equiv p_{yz}$ reconstruction and CID. Two magnetic field strengths $B = 0.2$ T and $B = 0.5$ T are adopted to validate improvements of momentum resolution and CID efficiencies by enhancing magnetic fields.

5.2.1 A Validation of Multiple Scattering Parameterized Formula By Simulation

In order to check consistencies between the multiple scattering distribution simulated by Geant4 and estimated by the parameterized formula Eq.(69), muons' distribution versus $\Delta y \equiv y_{\text{final}} - y_{\text{initial}}$ and its standard deviation $\sigma_{\Delta y}$ are studied with respect to different $\Delta z \equiv z_{\text{final}} - z_{\text{initial}}$.

$$\sigma_{\Delta y} = y_{\text{rms}}^{\text{plane}} \cdot \cos\left(\theta_{\text{plane}}\right) \tag{69}$$

The definitions of Δy, Δz and θ_{plane} are shown in Figure 20.

The results for 350 MeV/c (400 MeV/c) muon in the $B = 0.2$ T ($B = 0.5$ T) magnetic field are shown in Figure 23 (Figure 24). From Figure 23a, we can see that the smearing of Δy caused by multiple scatterings (the 2D histogram drawn in colorful scales) is quite significant when comparing to the $\Delta y^{\text{Lorentz}}$ calculated from the pure Lorentz force (red dots). Hence a not-so-good momentum resolution is expected. What's more, with the increase of Δz, a greater deviation between $\left(\Delta y\right)_{\text{mean}}$ (black dots) and Δy from the pure Lorentz force (red dots) clearly illustrates the effect of energy loss. Due to the energy loss in polystyrene, the decrease of muon's momentum leads to the smaller gyroradius and thus larger $\left(\Delta y\right)_{\text{mean}}$. It also explains the deviation between the simulated $\sigma_{\Delta y}$ and its prediction from the parameterized formula shown in Figure 23b. With the drop of muon's speed β and momentum p, the actual width of Δy distribution $\sigma_{\Delta y}$ is larger than the prediction from the parameterized formula Eq.(51), where the input β and p are muon's initial speed and momentum. At last, from entries of muons distributed above the horizontal line $\Delta y = 0$ in Figure 23a, it is evident

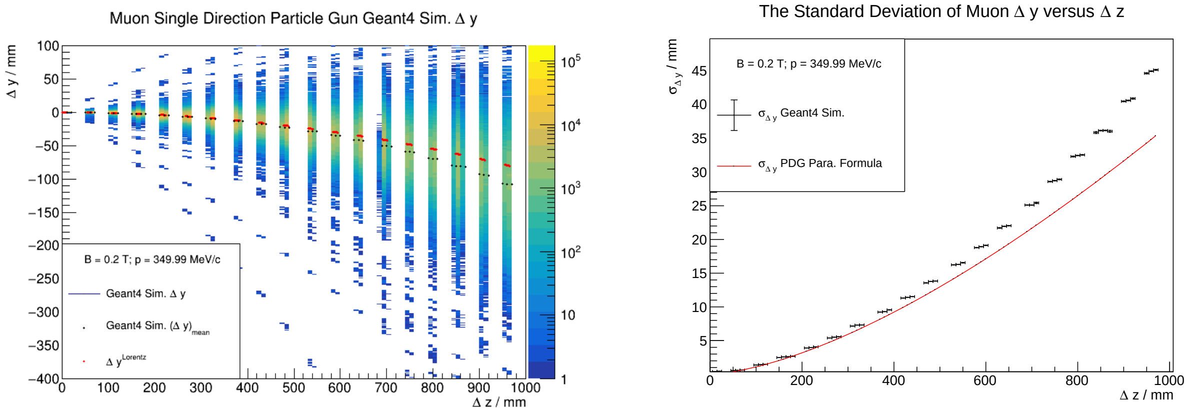

(a) The muon distribution versus Δy and Δz in mm. $(\Delta y)_{\text{mean}}$ (black dots) is the mean value of Geant4 simulated Δy for each Δz bin. The pure Lorentz force $\Delta y^{\text{Lorentz}}$ (red dots) is the Δy for each Δz bin when the muon is only subjected to the Lorentz force.

(b) The Geant4 simulated $\sigma_{\Delta y}$ (black dot with error bars) is calculated from the left Figure 23a for each Δz bin. The PDG parameterized formula predicted $\sigma_{\Delta y}$ (red curve) is obtained by multiplying $y^{\text{plane}}_{\text{rms}}$ (Eq.(53)) and $\cos(\theta_{\text{plane}})$ (see Figure 20).

Figure 23: muon $\vec{p}_{\text{initial}} = p_z\,\hat{e}_z = 350$ MeV/c, $B = 0.2$ T

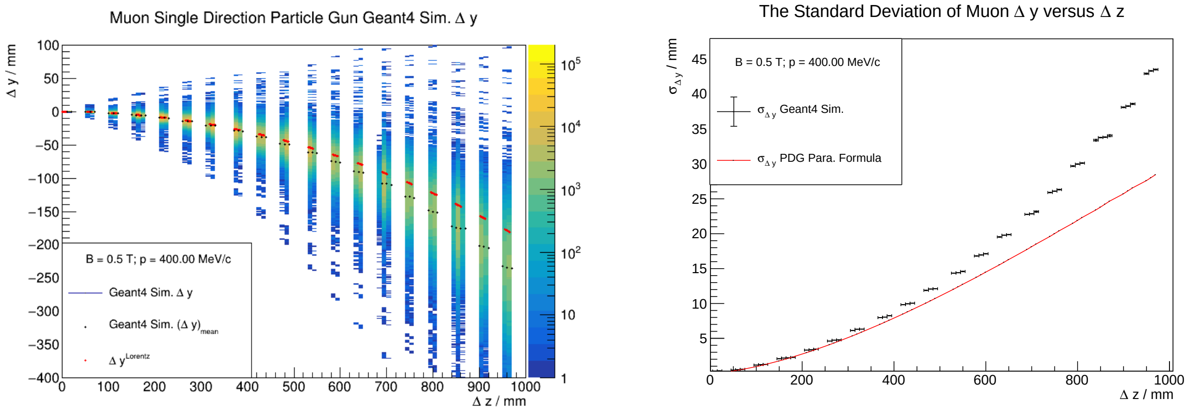

(a) The muon distribution versus Δy and Δz in mm. $(\Delta y)_{\text{mean}}$ (black dots) is the mean value of Geant4 simulated Δy for each Δz bin. The pure Lorentz force $\Delta y^{\text{Lorentz}}$ (red dots) is the Δy for each Δz bin when the muon is only subjected to the Lorentz force.

(b) The Geant4 simulated $\sigma_{\Delta y}$ (black dot with error bars) is calculated from the left Figure 24a for each Δz bin. The PDG parameterized formula predicted $\sigma_{\Delta y}$ (red curve) is obtained by multiplying $y^{\text{plane}}_{\text{rms}}$ (Eq.(53)) and $\cos(\theta_{\text{plane}})$ (see Figure 20).

Figure 24: muon $\vec{p}_{\text{initial}} = p_z\,\hat{e}_z = 400$ MeV/c, $B = 0.5$ T

that multiple scatterings can lead to wrong CID because it reverses the sign of Δy.

5.3 Momentum Reconstruction By Curvature

The curvature $k = R^{-1}$ of a track projected in yz plane can be reconstructed by a circular fit of the track in the yz view. The classical method is minimizing the χ^2 function Eq.(70) of a circle with three free parameters: the circle center (y_0, z_0) and radius R_{yz}.

$$\chi^2 \equiv \left(R_{yz} - \sum_{i \in \{yz \text{ SciFi hits}\}} \sqrt{\left(y_i - y_0\right)^2 + (z_i - z_0)^2} \right)^2 \tag{70}$$

The starting values of (y_0, z_0) for finding the local minimum of χ^2 can be approximated by the center of the circle defined by the first, the middle and the last yz SciFi hits. The starting R_{yz} is calculated by Eq.(45) from the most probable momenta of muon and pion from inclusive ν_μ-Carbon interactions modelled by NEUT with T2K ν_μ beam configuration. From Figure 25, we know the most probable momenta for muon and pion are 350 MeV/c and 200 MeV/c. For the nominal magnetic field strength $B = 0.2$ T, the starting and also the most probable values of R_{yz} are 5.83 m and 3.33 m for muon and pion, respectively. The result of circular fit is fairly unstable when noticing the randomness of track curvatures contributed from multiple scatterings. For example, for a 350 MeV/c muon only subjected to the Lorentz force in a uniform $\vec{B} = 0.2\text{T}\,\hat{e}_x$ magnetic field, the bending $\Delta y^{\text{Lorentz}}$ shown in Figure 20 after eight SciFi modules (i.e. $\Delta z \approx 400$ mm or 80 yz SciFi hits) is ~ 14 mm, which is around a 28-SciFi-diameter shift for 0.50-mm-diameter SciFi. Meanwhile, the $\sigma_{\Delta y} \approx 10$ mm caused by multiple scatterings shown in Figure 23b is comparable to $\Delta y^{\text{Lorentz}}$ at $\Delta z \approx 400$ mm.

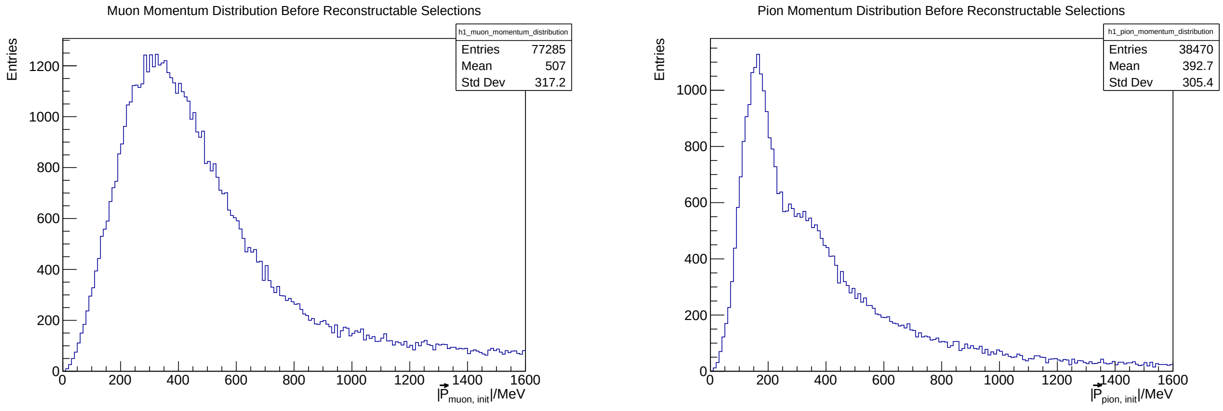

(a) muon **(b)** pion

Figure 25: The momenta distribution of muon and pion from inclusive ν_μ-Carbon interactions modelled by NEUT with T2K ν_μ beam configuration.

The task of the circular fit by minimizing the χ^2 function Eq.(70) is undertaken by the TMinuit Class of the ROOT [21] software. Once the R_{yz}^{reco} from the circular fit is got, it is straight forward to get $p_{yz}^{\text{reco}}(\text{GeV/c}) = 0.3\,B(\text{T})\,R(\text{m})$. Then the relative uncertainty (error) of momentum reconstruction by curvature is defined as

$$\frac{\delta p_{yz}}{p_{yz}} := \frac{p_{yz}^{\text{reco}} - p_{yz}^{\text{true}}}{p_{yz}^{\text{true}}}\,, \tag{71}$$

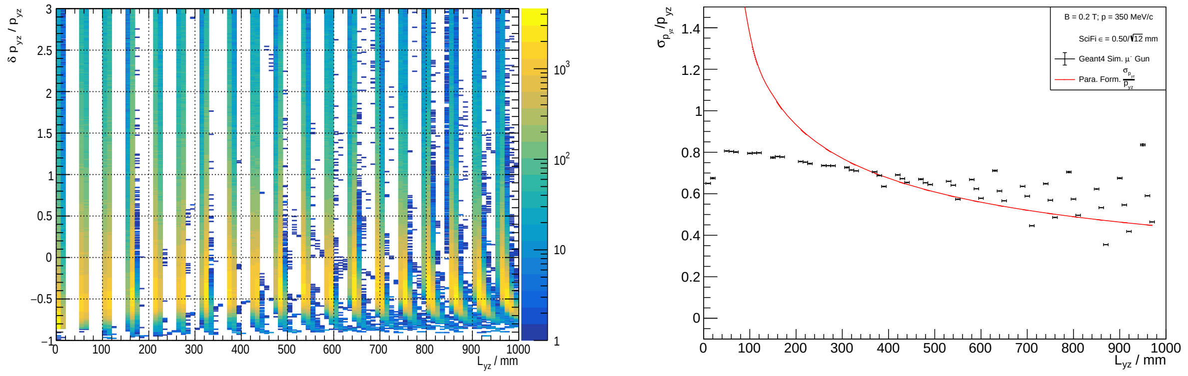

(a) The Geant4 simulated muon track distribution versus the reconstructed momentum error $\frac{\delta p_{yz}}{p_{yz}}$ (Eq.(71)) from the circular fit of the track and the projected track length L_{yz}.

(b) The standard deviation $\frac{\sigma_{p_{yz}}}{p_{yz}}$ derived either from the left Figure 26a (black dots) or the parameterized formula Eq.(67) (red curve) versus the projected track length L_{yz}.

Figure 26: muon $p_{yz}^{\text{true}} = 350$ MeV/c, $B = 0.2$ T

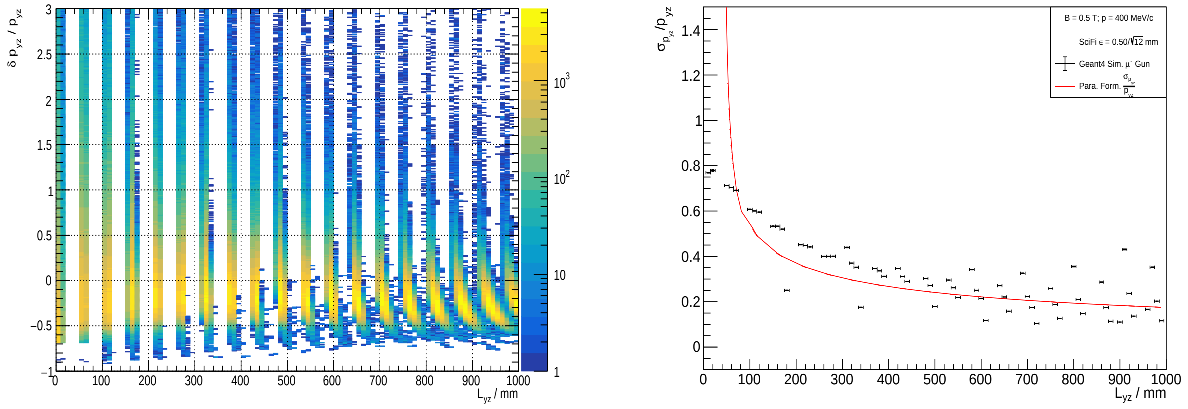

(a) The Geant4 simulated muon track distribution versus the reconstructed momentum error $\frac{\delta p_{yz}}{p_{yz}}$ (Eq.(71)) from the circular fit of the track and the projected track length L_{yz}.

(b) The standard deviation $\frac{\sigma_{p_{yz}}}{p_{yz}}$ calculated either from the left Figure 27a (black dots) or the parameterized formula Eq.(67) (red curve) versus the projected track length L_{yz}.

Figure 27: muon $p_{yz}^{\text{true}} = 400$ MeV/c, $B = 0.5$ T

where p_{yz}^{true} is the Geant4 true value of p_{yz} of the particle.

For the distribution of $\frac{\delta p_{yz}}{p_{yz}}$ (e.g. Figure 26a and 27a), its standard deviation $\frac{\sigma_{p_{yz}}}{p_{yz}}$ (e.g. Figure 26b and 27b) can be calculated and compared with the estimation from the parameterized formula Eq.(67). The first feature which we realized from Figure 26a and 27a is that the distributions of $\frac{\delta p_{yz}}{p_{yz}}$ are not centered around 0 but have a negative shift. This negative shift of the measured momenta is due to the energy loss when muon passes through the polystyrene, which can be verified by the fact that with the increase of the projected track length L_{yz}, the negative shift becomes larger due to the greater energy loss. Besides, for the matching between the $\frac{\sigma_{p_{yz}}}{p_{yz}}$ from the circular fit of the Geant4 simulation tracks and parameterized formula Eq.(67), the best match takes place at the intermediate region of L_{yz} (see Figure 26b and 27b). That is because when the L_{yz} is small, the deflection from multiple scatterings is comparable or even overwhelms the bending from the

Lorentz force. Hence this region does not satisfy the applicable assumptions of Eq.(59) and it explains the deviation between the two. The reasoning can also be verified by comparing Figure 26b and 27b. When the strength of magnetic field is increased from 0.2 T to 0.5 T, the bending from the Lorentz force is enhanced and the better match between the two shows up in the small L_{yz} region. For the large L_{yz} region, although the bending from the Lorentz force is more significant than the small-angle multiple scattering, the energy loss of muon at this region is also non-negligible and the β of muon is smaller than its initial value at the vertex. This is why at the large L_{yz} region the parameterized formula Eq.(60) applied to the whole track lowly estimates the standard deviation $\frac{\sigma_{p_{yz}}}{p_{yz}}$.

Overall, if a nominal magnetic field strength $B = 0.2$ T is adopted and a proper correction algorithm is well-developed for compensating measured down-shift momenta due to energy losses, then for 350 MeV/c muons whose track lengths taken for measurement are ~ 1000 mm, center-value correct momenta can be reconstructed with a 50% or so resolution . If the magnetic field strength is increased to 0.5 T, the momentum resoltuion for 1000-mm-long 400 MeV/c MIP muons can be improved to around 20%.

In conclusion, after the study above, we find that the momentum reconstruction by curvature in dense materials such as polystyrene is not a preferable method for precise measurements. The significance of multiple scatterings in polystyrene washes out a non-negligible amount of momentum information built in tracks' curvatures by the Lorentz force, no matter how fine the granularity of segmented detectors is.

5.4 Charge Identification By Curvature

A charge identification (CID) algorithm based on judgements of the bending direction of a charged particle in the plane perpendicular to the external magnetic field is developed. It can be simply and effectively implemented as follows.

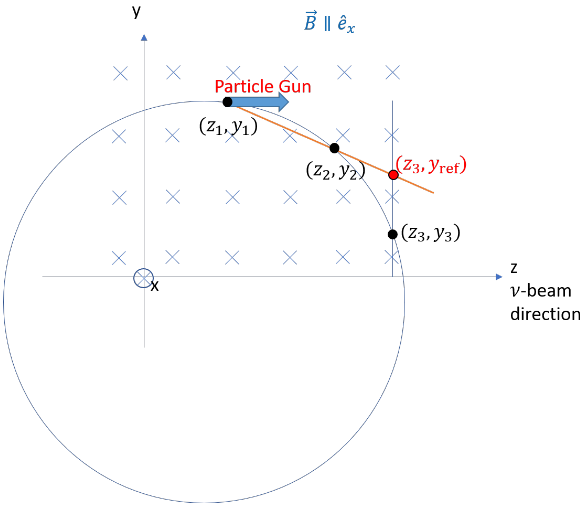

Figure 28: A Charge Identification By Curvature Configuration

1. For each CID available track, it has to have at least 9 SciFi hits in the yz view.

2. Three parts of SciFi hits in the yz view are grouped, averaged and input for CID. Namely the beginning three are averaged to (z_1, y_1), the middle three to (z_2, y_2) and the ending three to (z_3, y_3).

3. From (z_1, y_1) and (z_2, y_2), a straight reference line is defined. Substituting z_3 into the straight line equation yields a y_{ref}. For a CID configuration shown in Figure 28, CID results are

$$\begin{cases} y_{\text{ref}} \geq y_3 \Rightarrow \text{ negatively charged} \\ y_{\text{ref}} < y_3 \Rightarrow \text{ positively charged} \end{cases} . \tag{72}$$

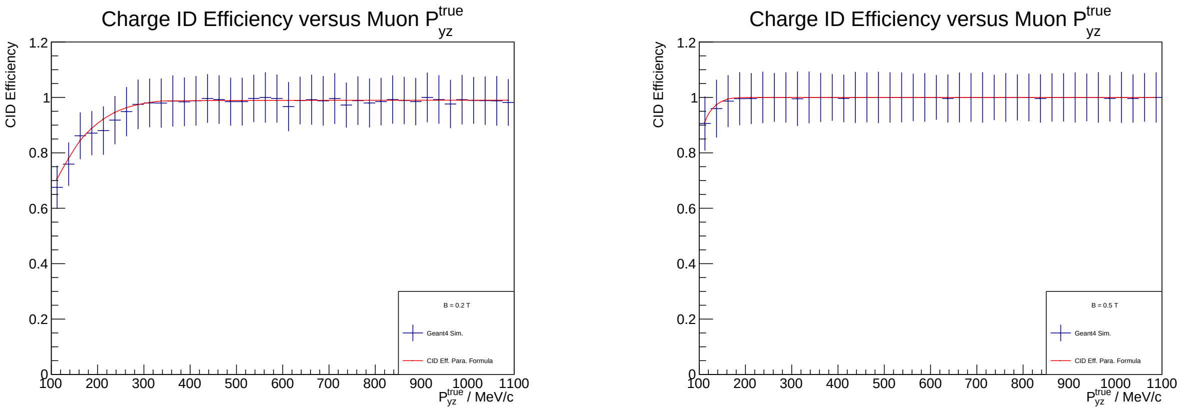

(a) $B = 0.2$ T **(b)** $B = 0.5$ T

Figure 29: The CID Efficiency of Muons μ^-

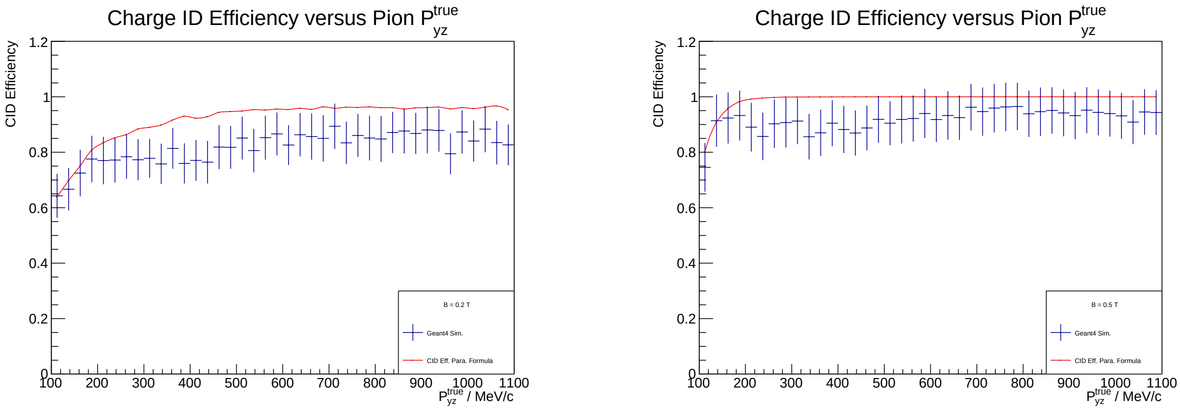

(a) $B = 0.2$ T **(b)** $B = 0.5$ T

Figure 30: The CID Efficiency of Pions π^-

CID efficiencies (Eq. 49) of muons μ^- and pions π^- with $B = 0.2$ T and $B = 0.5$ T magnetic field configurations are shown in Figure 29 and 30. Comparing to momentum reconstructions by curvature, the requirement of track details is much lower for CID. Therefore, from Figure 29, we can see a very nice match between the μ^-'s CID efficiency (blue dot with error bars) from

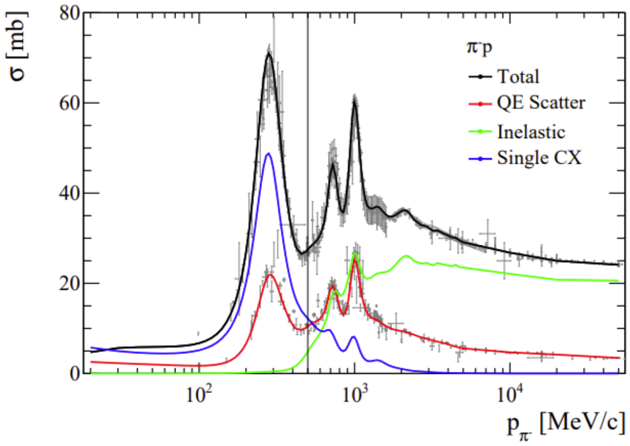

Figure 31: π^- on free proton scattering cross sections [33].

implementations of the CID algorithm introduced above to the Geant4 simlulated μ^- tracks and the CID efficiency (red curve) from the parameterized formula Eq.(61). The good match between simulations and the parameterized formula Eq.(61) in Figure 29 also explains that for muons, the CID inefficiency is mainly from small-angle multiple Coulomb scatterings. In the nominal magnetic field $B = 0.2$ T, the CID efficiency of muons whose momenta are above 300 MeV/c is nearly 100%. And this nearly 100% CID efficiency threshold extends down to 150 MeV/c if the magnetic field strength is increased to 0.5 T.

However, for pions π^-, the corresponding CID efficiency is lower than muon's. Besides, the discrepancy between the simulation and parameterized formula estimation appears when the π^-'s momentum is larger than 200 MeV/c. This is due to the fact that meson pions' multiple scatterings, which also include contributions of strong interactions with nuclei, are more intense than lepton muons'. And starting from $p_{\pi^-} = 200$ MeV/c or so, the inelastic scattering cross section which is not included in the small-angle multiple scattering arises (see Figure 31 [33]).

6 γ / $e^{\pm}$ Separation Study

In T2K experiment, an efficient rejection of electrons (positrons) from $\gamma \to e^+e^-$ is vital for excluding backgrounds that contaminates ν_e ($\bar{\nu}_e$) CC event samples, e.g. $\nu_e + n \to e^- + p$ and $\bar{\nu}_e + p \to e^+ + n$. Energetic photons γ which can pair-produce contamination electrons might come from $\pi^0 \to \gamma\gamma$ decays, where π^0 may come from nuclear effects of neutrino-nucleus interactions, for example. Therefore, it is important and promising to study $\gamma \to e^+e^-$ reconstruction efficiencies of our novel HFGD.

In subsection 6.1, Geant4 simulation samples of the pure SciFi design generated by γ guns and classifications of γ-hydrocarbon interactions are introduced. e^+e^- pair reconstruction efficiencies are estimated in subsection 6.2. With the help of 0.25 mm hyper-fine granularity of the pure SciFi design, a high efficiency of e^+e^- pair separation is expected. At last, a preliminary estimation of exclusive γ rejection efficiencies is presented in subsection 6.3.

6.1 Simulation Samples and Gamma-Hydrocarbon Interaction Counting

A main reference of subsection 6.1 is **Sec.34.4.5 Energy loss by photons** (pp. 557-558) of *The Review of Particle Physics (2022)* [1].

40, 100 γ uniformly distributed in an energy range between 100 MeV and 500 MeV are simulated by the Geant4 software of the pure SciFi design. A single direction γ gun shooting along the z axis defined in Figure 7 is used as particle sources. The γ gun is placed at the coordinate $(0, 0, -500)$ mm which is also the center of the first SciFi slice of the pure SciFi design.

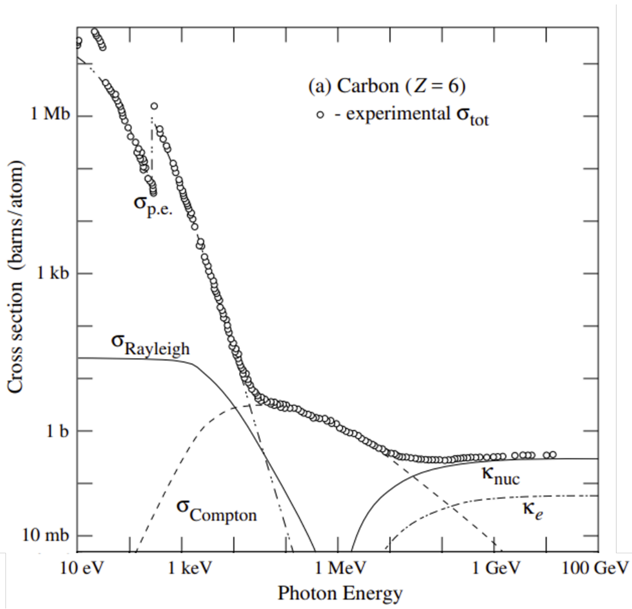

Figure 32: The Cross Section of γ-Carbon Interactions. $\sigma_{\text{p.e.}}$ stands for the cross section of photoelectric effect. κ_{nuc} and κ_e represent $\gamma \to e^+e^-$ pair production cross sections by interacting with nucleus field and electron field, respectively [1].

Cross sections of γ-Carbon interactions with different contributing processes have been thoroughly studied by many people in the past and summarized in Figure 32 [1]. As a validation of the

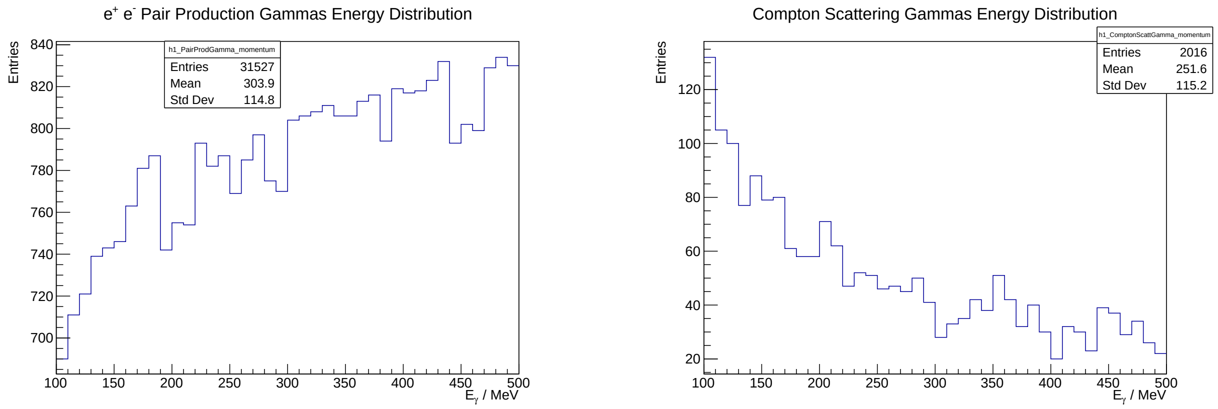

(a) e^+e^- Pair Production

(b) Compton Scattering

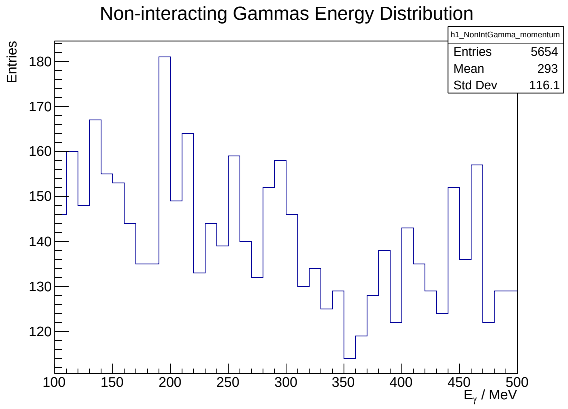

(c) No Interactions

Figure 33: The Energy Distribution of Incident Gammas Classified by Final States

Geant4 γ simulation sample, energy distributions of incident γ undergoing e^+e^- pair productions, Compton scatterings and non-interactions are plotted in Figure 33a, 33b and 33c, respectively. Comparing Figure 33 from the Geant4 simulation and Figure 32 for the photon energy range from 100 MeV to 500 MeV, they are consistent to each other:

1. with the increase of photon energy, pair production cross sections rise up;
2. with the increase of photon energy, the Compton scattering cross section drops down;
3. with the increase of photon energy, the totol γ-Carbon cross section roughly remains unchanged.

A counting of different proportions of $40,100$ incident γ classified by their final states after passing through the pure SciFi design is studied and listed below.

1. $31,527\,(\sim 78.62\%)$ γ undergo pure $\gamma \rightarrow e^+e^-$ pair productions as their initial interactions with the detector. They form a signal channel for γ reconstructions. The pair production probability 78.62% is also consistent with a published study quoted in Figure 34 [1]. An event display of this category is shown in Figure 35.

2. $2,016\,(\sim 5.03\%)$ γ have pure Compton scatterings $\gamma + e^- \rightarrow \gamma' + e^-$ with the detector, left with only one visible electron in their final states, e.g. Figure 36. They are the main background for gamma reconstruction, which in principle cannot be reconstructed.
3. $547\,(\sim 1.74\%)$ γ undergo a Compton scattering $\gamma + e^- \rightarrow \gamma' + e^-$ first and a subsequent $\gamma' \rightarrow e^+e^-$ pair production. From detector responses, they cannot be distinguished from electrons' bremsstrahlung, e.g. Figure 37, which also form part of the background.
4. $356\,(\sim 0.89\%)$ γ have photonuclear interactions with nuclei and nuclei are usually broken up to daughter hadrons and other nuclei.
5. $5,654\,(\sim 14.10\%)$ γ do not interact with the detector. The detector is blind to them so they have no influence to experiments.

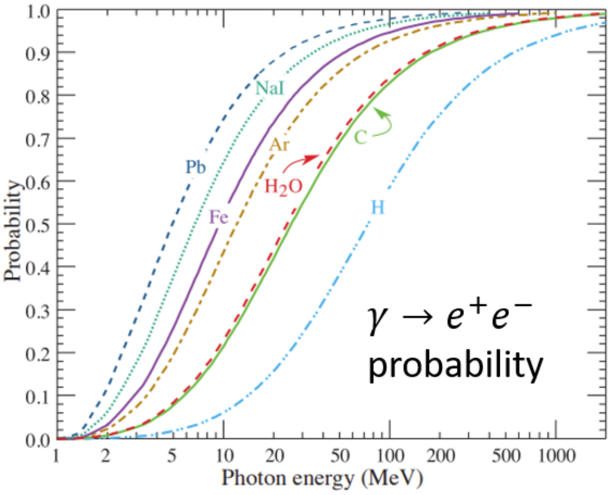

Figure 34: Probability that a photon interaction will result in conversion to an e^+e^- pair [1]

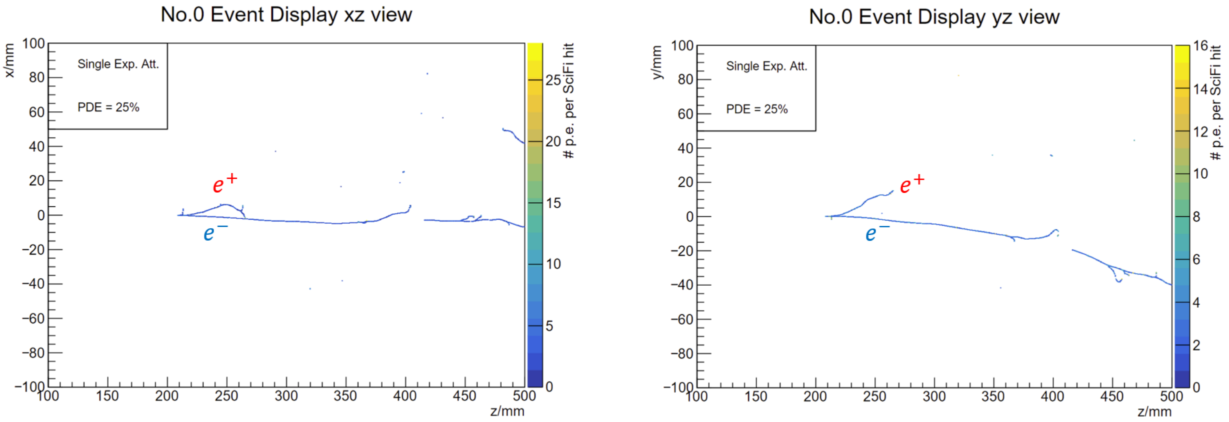

(a) xz View

(b) yz View

Figure 35: A Reconstructable $\gamma \rightarrow e^+e^-$ Event Display

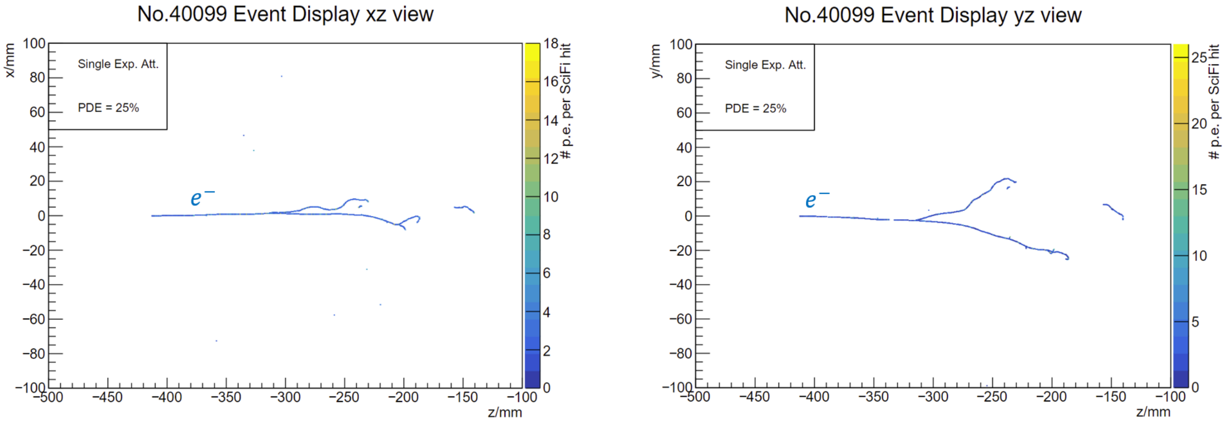

(a) xz View **(b)** yz View

Figure 36: A Background Compton Scattering $\gamma + e^- \rightarrow \gamma' + e^-$ Event Display With Only One Primary Electron Track Detectable

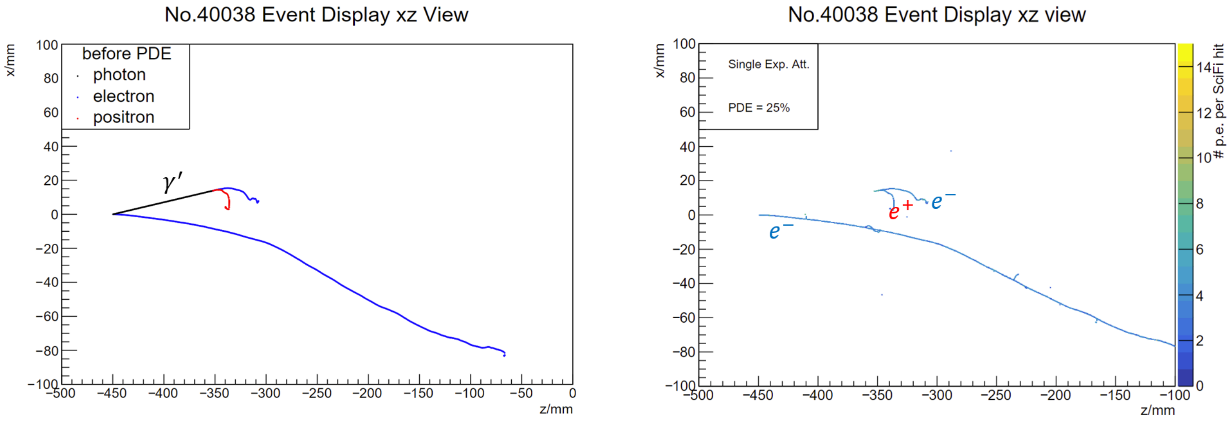

(a) xz View Geant4 Truth **(b)** xz View Detector Response

Figure 37: An Event Display of A Compton Scattering $\gamma + e^- \rightarrow \gamma' + e^-$ and A Subsequent Pair Production $\gamma' \rightarrow e^+ e^-$

6.2 e^+e^- Pair Reconstruction Efficiency Study

From Geant4 truth levels, $31,527$ $\gamma \rightarrow e^-e^+$ pair production signals are selected to study efficiencies of γ reconstructions. Since most of primary electron tracks are longer than protons' and pretty zig-zag due to multiple scatterings and bremsstrahlung, a set of new track reconstructable criterion for electrons is developed as follows

1. Enough hits: both electron and positron tracks of a e^-e^+ pair have enough detectable hits for track reconstructions, i.e. $\max\{\text{\# xz hits, \# yz hits}\} \geq 3$ and $\min\{\text{\# xz hits, \# yz hits}\} \geq 2$;
2. Separability: the detector (i.e. the pure SciFi design) is placed in a uniform magnetic field $\vec{B} = 0.2\,\mathrm{T}\,\hat{e}_x$. Thus electon and positron tracks are supposed to bend to opposite directions in yz view because of Lorentz force. For each e^-e^+ pair, a loop of iterating yz SciFi slices from e^-e^+ vertex to their track ends is conducted to examine whether there is at least one hit-free yz SciFi between two tracks for a certain yz SciFi slice. If so, the e^-e^+ pair is tagged as separable from each other.

An e^-e^+ pair which satisfies both enough hits and separability conditions are labeled as reconstructable.

For the 6% PDE configuration, after the first enough-hit condition selection, $27,014 (\sim 85.69\%)$ out of $31,527$ $\gamma \rightarrow e^-e^+$ pairs have enough detectable hits. Due to the 0.25 mm hyper-fine granularity of the pure SciFi design, the subsequent separability filter only drops the number of surviving pairs from $27,014$ to $26,731 (\sim 84.79\%)$. After improving the PDE to 25%, the number of enough-hit pairs increases to $31,361 (\sim 99.47\%)$ and the number of pairs fulfilling two conditions rises to $30,289 (\sim 96.07\%)$.

Two different phase spaces characterising the topology and momentum information of e^-e^+ pairs are introduced. The e^-e^+ pair initial distributions (i.e. before reconstruction selections) with respect to these two phase spaces are shown in Figure 38a and 38b, respectively. From Figure 38a, it is clear that the pair-produced electron and positron are very collinear. Most e^+e^- pairs distribute in the bin where $\cos(\theta_{e^-e^+}) > 0.99$. And statistically, momenta shared by electrons and positrons from parent γ shown in Figure 38b are very symmetric to each other, which is also a consequence of CP conservation in electromagnetic interactions.

The efficiency of e^+e^- pair reconstructions can be visualised versus two phase spaces defined in Figure 38 as well. Results are shown in Figure 39 and Figure 40. Comparing e^+e^- pair reconstruction efficiencies versus the same phase space but with different SPAD PDE, one can easily sense the enhancement of efficiencies by improving PDE, which effectively increases the number of detectable hits. Besides, in Figure 39, there are no distinct inefficiencies showing up in the bin where $\cos(\theta_{e^-e^+}) > 0.99$, which means that the hyper-fine granularity indeed alleviates separable constraints to a good extent. What's more, from Figure 40, one can notice that substantial inefficiencies only appear when electron's or positron's momentum is below 10 MeV, where they cannot produce enough detectable hits.

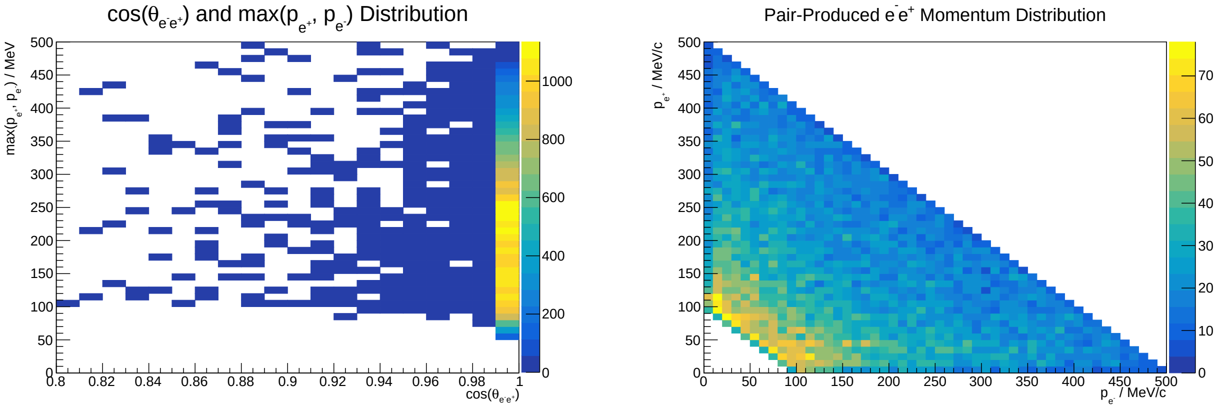

(a) The e^+e^- pair distribution versus the highest momentum in the pair and the angle $\theta_{e^+e^-}$ between their initial directions of motion.

(b) The e^+e^- pair distribution versus the initial momentum of the positron p_{e^+} and the initial momentum of the electron p_{e^-}.

Figure 38: The initial e^+e^- pair distribution before reconstructable selections.

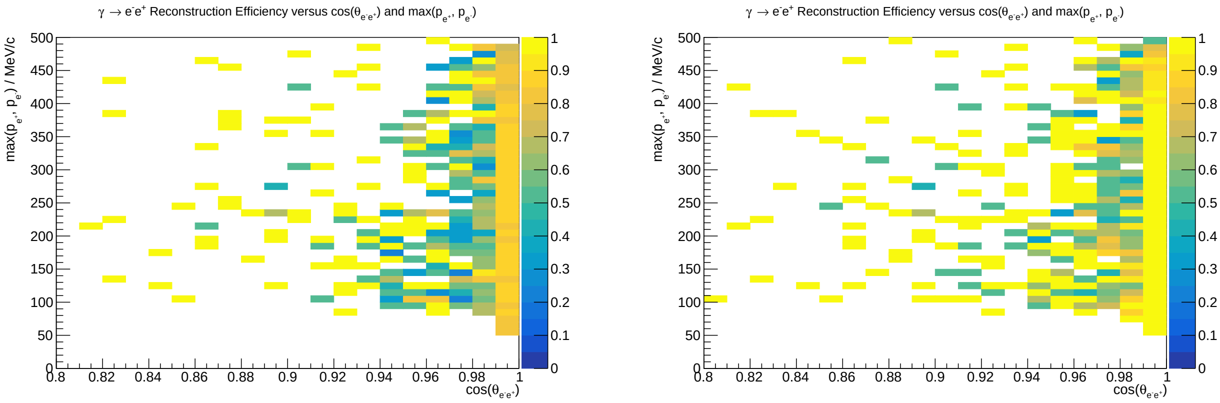

(a) PDE = 6%

(b) PDE = 25%

Figure 39: The e^+e^- pair reconstruction efficiency versus the highest momentum in the pair and the angle $\theta_{e^+e^-}$ between their initial directions of motion.

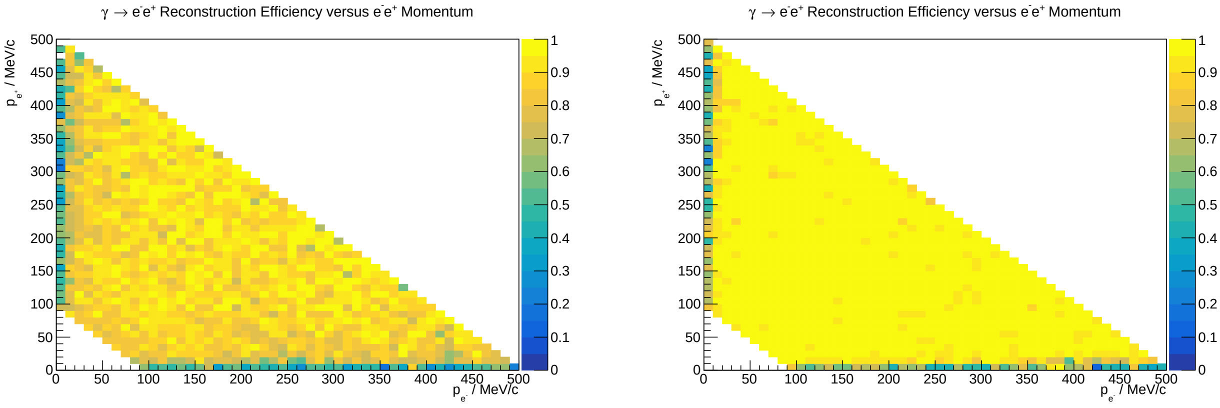

(a) PDE = 6%

(b) PDE = 25%

Figure 40: The e^+e^- pair reconstruction efficiency versus the initial momentum of the positron p_{e^+} and the initial momentum of the electron p_{e^-}.

6.3 Estimation of γ Rejection Efficiency

After reconstructing a pair of tracks from a same vertex, it is not sufficient to say a γ is reconstructed without identifying the pair is indeed e^+e^- pair. One may argue that an identification of two electron-like (by the electromagnetic shower feature) tracks carrying opposite electric charges can do the job. However, an implementation of the CID by curvature algorithm (see subsection 5.4) for e^+e^- pairs demonstrates that its efficiency is disappointingly low, which is mainly due to zigzag features of electron tracks from intensive multiple scatterings or bremsstrahlung. Taking the best 25% PDE configuration as an example, a reliable bending direction judgement requires at least 9 SciFi hits in yz view, which will bring down the 96.07% pair reconstruction efficiency to 95.60% and it is still tolerable. However, correlations between actual bending directions and signs of electric charges are so weak that eventually only 32.44% of $\gamma \rightarrow e^+e^-$ signals can be successfully reconstructed by this method. A robust multiple scattering pattern recognition algorithm for e^+e^- pairs might be a good solution. If we assume an efficiency of the e^+e^- pair recognition algorithm based on our reconstructable pairs to be $x \in (0, 1)$, then the $\gamma \rightarrow e^+e^-$ reconstruction efficiency will be around $84\% \cdot x$ and $96\% \cdot x$ for 6% and 25% PDE configurations, respectively. Developing a pattern recognition algorithm is of great complexity and beyond the scope of this master thesis.

Practically, an efficiency of rejecting electrons and positrons originated from photons (i.e. γ rejection efficiency) is a more useful form of the same topic. From the counting shown in subsection 6.1, the Compton scattering events are dominate backgrounds which cannot be eradicated, due to the appearance of a single detached electron track in final states. Combining the Compton scattering backgrounds and the $\gamma \rightarrow e^+e^-$ signals, two indefinite γ rejection efficiencies $\frac{26731 \cdot x}{31527+2016+547} < 78.41\%$ and $\frac{30289 \cdot x}{31527+2016+547} < 88.85\%$ with upper bounds can be obtained for 6% and 25% PDE configurations, respectively. x is the indefinite e^+e^- pair pattern recognition efficiency based on our reconstructable pairs.

7 Conclusions

A novel polystyrene-based neutrino target detector based on sub-mm scintillating fibers (SciFi) with either the scintillating cube-SciFi hybrid design or the pure SciFi design is simulated and studied by joint applications of NEUT and Geant4 software.

The Birks' light quenching correction, the SciFi trapping efficiency, the optical attenuation in SciFi, and the photon detection efficiency (PDE) of the readout SPAD array sensors are treated as detector response processes and coded independent of Geant4 with two SPAD PDE configurations: the currently available 6% PDE and the improved 25% PDE which is still under R&Ds.

The 0.25 mm hyper-fine granularity of the pure SciFi design extends the momentum threshold of reconstructable protons down to 150 MeV/c, with an over 97% unprecedented high net proton reconstruction efficiency for CCQE events generated by NEUT with T2K ν_μ energy spectrum. The relevant CC0πNp ($N = 1, 2, 3, 4$) event reconstruction efficiencies are also explored. A preliminary particle identification (PID) method based on a linear cut on a 2D Bragg Peak - Track Length phase space is proposed and capable of separating protons and muons with both PID efficiency and purity above 90%.

The momentum reconstruction by curvature is studied with the hybrid design of HFGD consisting of 0.50-mm-diameter SciFi. Both parameterized formulas and Geant4 simulations predict a 50% (20%) or so momentum resolution for a minimum ionizing 1000 mm long muon track bent in a uniform magnetic field $B = 0.2$ T ($B = 0.5$ T). Main constraints of momentum resolutions by curvature in plastic scintillators come from intense multiple scatterings. The expectation value of reconstructed momenta by curvature needs to be corrected to compensate energy losses in polystyrene. The charge identification (CID) efficiency by curvature for muons and pions is studied by both Geant4 simulations and parameterized formulas. For muons, the CID efficiency by curvature is nearly 100% when their momenta are above 300 MeV/c (150 MeV/c) for $B = 0.2$ T ($B = 0.5$ T). However for pions, the CID efficiency by curvature has a 90% (95%) upper limit for $B = 0.2$ T ($B = 0.5$ T) restricted by large-angle “hard" scatters from strong interactions with nuclei and inelastic scatters.

The γ rejection efficiency of the pure 0.25-mm-diameter SciFi design is studied for estimating γ-initiated $e^{\pm}$'s contamination to events sample generated by incident ν_e or $\bar{\nu}_e$. Two indefinite γ rejection efficiencies with 78.41% and 88.85% upper limits are obtained for 6% and 25% PDE, respectively. The indefinity comes from an undeveloped e^+e^- pair pattern recognition algorithm.

For further improvements and future studies, the PID efficiency for separating muons and protons can be enhanced by implementing a more complicated curved 2D separation on the Bragg Peak - Track Length phase space. An energy loss compensation algorithm for momentum reconstructions by curvature can be developed. If enough time and energy are invested, an efficient e^+e^- pair pattern recognition algorithm based on the features of electromagnetic shower and $e^{\pm}$ multiple scatterings with dense materials can be realized.

References

[1] Particle Data Group et al. “Review of Particle Physics”. In: *Progress of Theoretical and Experimental Physics* 2022.8 (Aug. 2022), p. 083C01. ISSN: 2050-3911. DOI: `10.1093/ptep/ptac097`. eprint: `https://academic.oup.com/ptep/article-pdf/2022/8/083C01/49175539/ptac097.pdf`. URL: `https://doi.org/10.1093/ptep/ptac097`.

[2] A. Rubbia. *Phenomenology of Particle Physics.* Cambridge University Press, 2022. DOI: `10.1017/9781009023429`.

[3] Wikipedia contributors. *Neutrino oscillation — Wikipedia, The Free Encyclopedia.* [Online; accessed 9-October-2023]. 2023. URL: `https://en.wikipedia.org/w/index.php?title=Neutrino_oscillation&oldid=1169153431`.

[4] Z. Maki, M. Nakagawa and S. Sakata. “Remarks on the Unified Model of Elementary Particles”. In: *Progress of Theoretical Physics* 28.5 (Nov. 1962), pp. 870–880. ISSN: 0033-068X. DOI: `10.1143/PTP.28.870`. eprint: `https://academic.oup.com/ptp/article-pdf/28/5/870/5258750/28-5-870.pdf`. URL: `https://doi.org/10.1143/PTP.28.870`.

[5] Wikipedia contributors. *Solar neutrino — Wikipedia, The Free Encyclopedia.* [Online; accessed 25-October-2023]. 2023. URL: `https://en.wikipedia.org/w/index.php?title=Solar_neutrino&oldid=1176449975`.

[6] The T2K Collaboration 2021. *About T2K.* [Online; accessed 9-October-2023]. 2021. URL: `https://t2k-experiment.org/t2k/`.

[7] K. Abe et al. “The T2K experiment”. In: *Nuclear Instruments and Methods in Physics Research Section A: Accelerators, Spectrometers, Detectors and Associated Equipment* 659.1 (2011), pp. 106–135. ISSN: 0168-9002. DOI: `https://doi.org/10.1016/j.nima.2011.06.067`. URL: `https://www.sciencedirect.com/science/article/pii/S0168900211011910`.

[8] S. Ajimura et al. “The JSNS2 detector”. In: *Nuclear Instruments and Methods in Physics Research Section A: Accelerators, Spectrometers, Detectors and Associated Equipment* 1014 (2021), p. 165742. ISSN: 0168-9002. DOI: `https://doi.org/10.1016/j.nima.2021.165742`. URL: `https://www.sciencedirect.com/science/article/pii/S0168900221007270`.

[9] K2K Collaboration. *Long Baseline neutrino oscillation experiment, from KEK to Kamioka (K2K).* [Online; accessed 21-October-2023]. 2023. URL: `https://neutrino.kek.jp/intro/k2k.html`.

[10] M. Franks et al. *Demonstration of particle tracking with scintillating fibres read out by a SPAD array sensor and application as a neutrino active target.* 2023. arXiv: 2309.03131 `[physics.ins-det]`.

[11] The T2K Collaboration 2021. *T2K and beyond.* [Online; accessed 9-October-2023]. 2021. URL: `https://t2k-experiment.org/beyond-t2k/`.

[12] K. Abe et al. *T2K ND280 Upgrade – Technical Design Report*. 2020. arXiv: `1901.03750 [physics.ins-det]`.

[13] K. Abe et al. "Updated T2K measurements of muon neutrino and antineutrino disappearance using 3.6×10^{21} protons on target". In: *Phys. Rev. D* 108 (7 Oct. 2023), p. 072011. DOI: `10.1103/PhysRevD.108.072011`. URL: `https://link.aps.org/doi/10.1103/PhysRevD.108.072011`.

[14] Kamioka Observatory, ICRR, The University of Tokyo. *About Super-Kamiokande: Overview*. [Online; accessed 20-October-2023]. 2023. URL: `https://www-sk.icrr.u-tokyo.ac.jp/en/sk/about/outline/`.

[15] J. A. Formaggio and G. P. Zeller. "From eV to EeV: Neutrino cross sections across energy scales". In: *Rev. Mod. Phys.* 84 (3 Sept. 2012), pp. 1307–1341. DOI: `10.1103/RevModPhys.84.1307`. URL: `https://link.aps.org/doi/10.1103/RevModPhys.84.1307`.

[16] Y. Hayato and L. Pickering. "The NEUT neutrino interaction simulation program library". In: *The European Physical Journal Special Topics* 230 (Dec. 2021), pp. 4469–4481. ISSN: 1951-6401. DOI: `10.1140/epjs/s11734-021-00287-7`. URL: `https://doi.org/10.1140/epjs/s11734-021-00287-7`.

[17] J. Allison et al. "Recent developments in Geant4". In: *Nuclear Instruments and Methods in Physics Research Section A: Accelerators, Spectrometers, Detectors and Associated Equipment* 835 (2016), pp. 186–225. ISSN: 0168-9002. DOI: `https://doi.org/10.1016/j.nima.2016.06.125`. URL: `https://www.sciencedirect.com/science/article/pii/S0168900216306957`.

[18] J. Allison et al. "Geant4 developments and applications". In: *IEEE Transactions on Nuclear Science* 53.1 (2006), pp. 270–278. DOI: `10.1109/TNS.2006.869826`.

[19] S. Agostinelli et al. "Geant4—a simulation toolkit". In: *Nuclear Instruments and Methods in Physics Research Section A: Accelerators, Spectrometers, Detectors and Associated Equipment* 506.3 (2003), pp. 250–303. ISSN: 0168-9002. DOI: `https://doi.org/10.1016/S0168-9002(03)01368-8`. URL: `https://www.sciencedirect.com/science/article/pii/S0168900203013688`.

[20] O. Borshchev et al. "Development of a New Class of Scintillating Fibres with Very Short Decay Time and High Light Yield". In: *Journal of Instrumentation* 12.05 (May 2017), P05013. DOI: `10.1088/1748-0221/12/05/P05013`. URL: `https://dx.doi.org/10.1088/1748-0221/12/05/P05013`.

[21] R. Brun and F. Rademakers. "ROOT — An object oriented data analysis framework". In: *Nuclear Instruments and Methods in Physics Research Section A: Accelerators, Spectrometers, Detectors and Associated Equipment* 389.1 (1997). New Computing Techniques in Physics Research V, pp. 81–86. ISSN: 0168-9002. DOI: `https://doi.org/10.1016/S0168-9002(97)00048-X`. URL: `https://www.sciencedirect.com/science/article/pii/S016890029700048X`.

[22] T. Lindner and for ND280 Computing Group. “Evolution of the T2K-ND280 Computing Model”. In: *Journal of Physics: Conference Series* 664.3 (Dec. 2015), p. 032021. DOI: `10.1088/1742-6596/664/3/032021`. URL: `https://dx.doi.org/10.1088/1742-6596/664/3/032021`.

[23] Wikipedia contributors. *Quenching (fluorescence) — Wikipedia, The Free Encyclopedia.* [Online; accessed 10-October-2023]. 2023. URL: `https://en.wikipedia.org/w/index.php?title=Quenching_(fluorescence)&oldid=1168622353`.

[24] Wikipedia contributors. *Scintillator — Wikipedia, The Free Encyclopedia.* [Online; accessed 10-October-2023]. 2023. URL: `https://en.wikipedia.org/w/index.php?title=Scintillator&oldid=1179365268`.

[25] J. B. Birks. “Scintillations from Organic Crystals: Specific Fluorescence and Relative Response to Different Radiations”. In: *Proceedings of the Physical Society. Section A* 64.10 (Oct. 1951), p. 874. DOI: `10.1088/0370-1298/64/10/303`. URL: `https://dx.doi.org/10.1088/0370-1298/64/10/303`.

[26] Ltd. Kuraray Co. *Scintillating Fibers.* [Online; accessed 10-October-2023]. URL: `http://kuraraypsf.jp/psf/sf.html`.

[27] Wikipedia contributors. *Bragg peak — Wikipedia, The Free Encyclopedia.* [Online; accessed 24-October-2023]. 2023. URL: `https://en.wikipedia.org/w/index.php?title=Bragg_peak&oldid=1163743097`.

[28] A. Ershova et al. “Study of final-state interactions of protons in neutrino-nucleus scattering with INCL and NuWro cascade models”. In: *Phys. Rev. D* 106 (3 Aug. 2022), p. 032009. DOI: `10.1103/PhysRevD.106.032009`. URL: `https://link.aps.org/doi/10.1103/PhysRevD.106.032009`.

[29] J. R. Letaw, R. Silberberg and C. H. Tsao. “Proton-nucleus total inelastic cross sections: An empirical formula for E>10 MeV”. In: *Astrophys. J., Suppl. Ser.; (United States)* 51:3 (Mar. 1983). DOI: `10.1086/190849`. URL: `https://www.osti.gov/biblio/6258823`.

[30] L.W. Townsend and J.W. Wilson. *Tables of Nuclear Cross Sections for Galactic Cosmic Rays: Absorption Cross Sections.* NASA reference publication. National Aeronautics, Space Administration, Scientific and Technica[l] Information Branch, May 1985. URL: `https://ntrs.nasa.gov/citations/19850019354`.

[31] G. R. Lynch and O. I. Dahl. “Approximations to multiple Coulomb scattering”. In: *Nuclear Instruments and Methods in Physics Research Section B: Beam Interactions with Materials and Atoms* 58.1 (1991), pp. 6–10. ISSN: 0168-583X. DOI: `https://doi.org/10.1016/0168-583X(91)95671-Y`. URL: `https://www.sciencedirect.com/science/article/pii/0168583X9195671Y`.

[32] Wikimedia Commons. *File:Sagitta.svg — Wikimedia Commons, the free media repository*. [Online; accessed 25-October-2023]. 2020. URL: `https://commons.wikimedia.org/w/index.php?title=File:Sagitta.svg&oldid=444862479`.

[33] P. de Perio. "Neut Pion Fsi". In: *NUINT11: the 7th International Workshop on Neutrino-Nucleus Interactions in the Few GeV Regions*. Ed. by S. K. Singh et al. Vol. 1405. American Institute of Physics Conference Series. Nov. 2011, pp. 223–228. DOI: `10.1063/1.3661590`. arXiv: `1405.3973 [nucl-ex]`.